APRIL–JUNE 2024 VOL. 16 № 2 (61)

ISSN 2075-8251

ActaNaturae

Experimental Use of Common Marmosets (*Callithrix jacchus*) in Preclinical Trials of Antiviral Vaccines

MOLECULAR MECHANISMS OF *DROSOPHILA* HEMATOPOIESIS
P. 4

A VECTOR NANOPLATFORM FOR THE BIOIMAGING OF DEEP-SEATED TUMORS
P. 72

Evaluation of HER2/neu Expression in Metastatic Axillary Lymph Node Tissue of Breast Cancer Patients Using [^{99m}Tc]Tc-(HE)$_3$-G3

O. D. Bragina, L. A. Tashireva, D. M. Loos, S. V. Vtorushin, A. A. Shulga, E. N. Konovalova, M. E. Borodina, V. I. Chernov, V. M. Tolmachev, S. M. Deyev

Anatomic visualization and molecular typing of metastatic regional lymph nodes in breast cancer patients are a serious clinical challenge in modern oncology. According to the results of previous studies, [^{99m}Tc]Tc-(HE)$_3$-G3 has proven to be a promising diagnostic agent in differentiating the HER2/neu receptor status in primary breast tumors. In that case, sensitivity and specificity for the mALN-to-background ratio were identical at 80%.

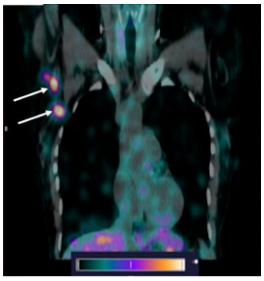

[^{99m}Tc]Tc-(HE)$_3$-G3 uptake in metastatic axillary lymph node of breast cancer patients 4 h after administration

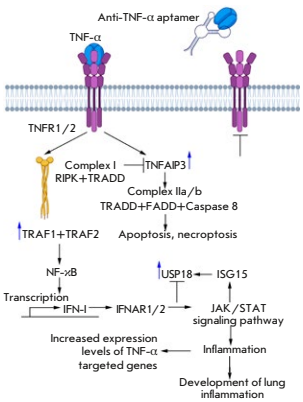

The general scheme of TNF-α signaling

LPS-Induced Acute Lung Injury: Analysis of the Development and Suppression by the TNF-α-Targeting Aptamer

A. V. Sen'kova, I. A. Savin, E. L. Chernolovskaya, A. S. Davydova, M. I. Meschaninova, A. Bishani, M. A. Vorobyeva, M. A. Zenkova

Acute lung injury (ALI) is a specific form of lung inflammation characterized by diffuse alveolar damage, noncardiogenic pulmonary edema, as well as pulmonary and systemic inflammation. The development of lipopolysaccharide (LPS)-induced ALI, as well as the feasibility of suppressing it by an aptamer targeting the proinflammatory cytokine TNF-α, was studied in a mouse model.

An Attenuated and Highly Immunogenic Variant of the Vaccinia Virus

S. N. Shchelkunov, S. N. Yakubitskiy, K. A. Titova, S. A. Pyankov, I. S. Shulgina, E. V. Starostina, M. B. Borgoyakova, D. N. Kisakov, L. I. Karpenko, G. A. Shchelkunova, A. A. Sergeev

Today, there exists a pressing problem related to developing safe and highly immunogenic next-generation vaccines against orthopoxvirus infections. In this study, we have created the LADA strain with an additional deletion in the LAD strain ati gene, which directs the production of a major non-virion immunogen. The LADA variant is attenuated and more immunogenic compared to the L strain, which is used for producing the first-generation smallpox vaccine clinically approved in Russia. The *A35R* and *ati* genes can be considered to be a targeting insertion of desired genes into DNA of the LIVP-A34R* strain when developing safe and efficacious polyvalent live vaccinia virus-based vaccines.

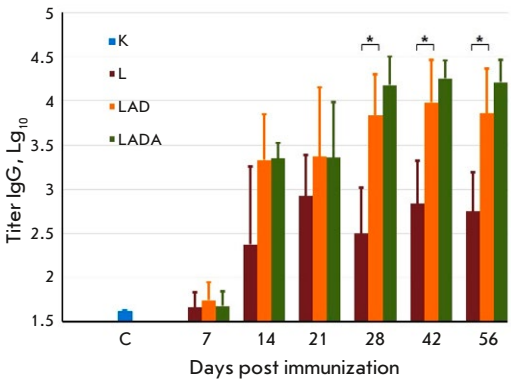

The titers of the VACV-specific IgG in the sera of mice immunized with the L, LAD, or LADA viruses

ActaNaturae
APRIL–JUNE 2024 VOL. 16 № 2 (61)
since april 2009, 4 times a year

Founders
Acta Naturae, Ltd,
National Research University
Higher School of Economics

Adress: 101000, Moscow, Myasnitskaya Ulitsa, 13, str. 4
Phone/Fax: +7 (495) 727 38 60
E-mail: actanaturae@gmail.com

Номер подписан в печать 30 июня 2024 г.
Тираж 15 экз. Цена свободная.
Отпечатано в типографии: НИУ ВШЭ,
г. Москва, Измайловское шоссе, 44, стр. 2

Founder and Chairman
of the Editorial Board (from 2009 to 2023)
of the journal Acta Naturae
Academician Grigoriev Anatoly Ivanovich

Indexed in PubMed, Web of Science, Scopus, and RISC

Impact Factor: 2.0 (WOS); 3.5 (Scopus)

CONTENTS

REVIEWS

S. A. Sinenko
Molecular Mechanisms of *Drosophila* Hematopoiesis 4

RESEARCH ARTICLES

O. D. Bragina, L. A. Tashireva, D. M. Loos, S. V. Vtorushin, A. A. Shulga, E. N. Konovalova, M. E. Borodina, V. I. Chernov, V. M. Tolmachev, S. M. Deyev
Evaluation of HER2/neu Expression in Metastatic Axillary Lymph Node Tissue of Breast Cancer Patients Using [^{99m}Tc]Tc-(HE)$_3$-G3 22

I. V. Gordeychuk, O. S. Gancharova, S. A. Gulyaev, T. V. Gulyaeva, A. S. Zhitkevich, D. V. Avdoshina, A. V. Moroz, A. S. Lunin, S. E. Sotskova, E. A. Korduban, A. I. Tukhvatulin, E. O. Bayurova, A. A. Ishmukhametov

Experimental Use of Common Marmosets (*Callithrix jacchus*) in Preclinical Trials of Antiviral Vaccines 30

E. V. Ivanov, M. R. Akhmetshina, A. R. Gizatulina, M. V. Gulyaev, O. S. Pavlova, Y. A. Pirogov, S. A. Gavrilova

Dihydroquercetin-Loaded Liposomes Change Fibrous Tissue Distribution in the Bleomycin-Induced Fibrosis Model 40

K. I. Kirsanov, T. I. Fetisov, E. E. Antoshina, T. G. Gor'kova, L. S. Trukhanova, S. I. Shram, I. Yu. Nagaev, Yu. A. Zolotarev, L. Abo Qoura, V. S. Pokrovsky, M. G. Yakubovskaya, V. K. Švedas, D. K. Nilov

7-Methylguanine Inhibits Colon Cancer Growth *in Vivo* 50

N. G. Lozhkina, O. I. Gushchina, N. V. Basov, E. V. Gaisler, A. D. Rogachev, Yu. S. Sotnikova, Yu. V. Patrushev, A. G. Pokrovsky

Ceramides As Potential New Predictors of the Severity of Acute Coronary Syndrome in Conjunction with SARS-CoV-2 Infection 53

A. V. Sen'kova, I. A. Savin, E. L. Chernolovskaya, A. S. Davydova, M. I. Meschaninova, A. Bishani, M. A. Vorobyeva, M. A. Zenkova

LPS-Induced Acute Lung Injury: Analysis of the Development and Suppression by the TNF-α-Targeting Aptamer 61

E. I. Shramova, S. M. Deyev, G. M. Proshkina

A Vector Nanoplatform for the Bioimaging of Deep-Seated Tumors 72

S. N. Shchelkunov, S. N. Yakubitskiy, K. A. Titova, S. A. Pyankov, I. S. Shulgina, E. V. Starostina, M. B. Borgoyakova, D. N. Kisakov, L. I. Karpenko, G. A. Shchelkunova, A. A. Sergeev

An Attenuated and Highly Immunogenic Variant of the Vaccinia Virus 82

Guidelines for Authors 90

IMAGE ON THE COVER PAGE
(see the article by Gordeychuk et al.)

Molecular Mechanisms of *Drosophila* Hematopoiesis

S. A. Sinenko
Institute of Cytology Russian Academy of Sciences, St. Petersburg, 194064 Russian Federation
E-mail: s.sinenko@incras.ru
Received: April 05, 2024; in final form, May 31, 2024
DOI: 10.32607/actanaturae.27410

ABSTRACT **As a model organism, the fruit fly (*Drosophila melanogaster*) has assumed a leading position in modern biological research. The *Drosophila* genetic system has a number of advantages making it a key model in investigating the molecular mechanisms of metazoan developmental processes. Over the past two decades, significant progress has been made in understanding the molecular mechanisms regulating *Drosophila* hematopoiesis. This review discusses the major advances in investigating the molecular mechanisms involved in maintaining the population of multipotent progenitor cells and their differentiation into mature hemocytes in the hematopoietic organ of the *Drosophila* larva. The use of the *Drosophila* hematopoietic organ as a model system for hematopoiesis has allowed to characterize the complex interactions between signaling pathways and transcription factors in regulating the maintenance and differentiation of progenitor cells through the signals from the hematopoietic niche, autocrine and paracrine signals, and the signals emanated by differentiated cells.**

KEYWORDS **hematopoiesis, hematopoietic organ, multipotency, hematopoietic stem cells, hematopoietic niche, *Drosophila melanogaster*, hemocytes, differentiation, signaling pathways, transcription factors.**

ABBREVIATIONS **HO – hematopoietic organ (lymph glands); DC – dorsal vessel; PPHs – preprohemocytes; PHs – prohemocytes; IPHs – intermediate prohemocytes; PSC– posterior signaling center; MZ – medullary zone; CZ – cortical zone; IZ – intermediate zone; PL – plasmatocytes; CC – crystalline cells; LM – lamellocytes; ROS – reactive oxygen species; AMP – antimicrobial peptides; ECM – extracellular matrix; UAS – upstream activation sequence; scRNAseq – single-cell RNA sequencing; HSCs – hematopoietic stem cells; SCs – stem cells; AGM – aorta-gonad-mesonephros; Odd – Odd-skiped; Crq – Croquemort; TF – transcription factor; Antp – Antennapedia; NimC1 – Nimrod C1; Col - Collier; Hth – Homothorax; Tin – Tinman; Pnr – Pannier; FGFR – fibroblast growth factor receptor; Htl – Heartless; Dpp – Decapentaplegic; Wg – Wingless; Hh – Hedgehog; Ser – Serrate; Dome – Domeless; E-cad – E-cadherin; Vkg – Viking; Hml – Hemollectin; PPO – prophenoloxidase; Lz – Lozenge; Hnt – Hindsight; Fz – Frizzled; Dot – Dorothy; Mad – mothers against dpp; Sd – Scalloped; Ptc – Patched; Ci – Cubitus interruptus; EGFR – epidermal growth factor receptor; TGF-beta – transforming growth factor beta; PCP – planar cell polarity; FGF – fibroblast growth factor; Upd1–3 – Unpaired 1–3; FoxO – forkhead box protein O; Adgf-A – adenosine deaminase growth factor-A; AdoR – adenosine receptor; PKA – protein kinase A.**

INTRODUCTION

The fruit fly (*Drosophila melanogaster*) is a model organism that has been widely used in genetic studies in cell biology, developmental biology, and immunology. It has been more than 100 years since Thomas Hunt Morgan began using this model system in genetic research [1, 2]. For genetic and biomedical research, *Drosophila* provided several advantages: (1) a minimal set of chromosomes of only four pairs, three of which (X/Y, II, III) virtually contain all the genes of the organism; (2) *Drosophila*'s fully sequenced and annotated genome consists of approximately 13,767 genes and is characterized by a minimum number of duplicated genes and mini-

mal gene redundancy; (3) the methods for producing mutant *Drosophila* lines have been well developed and include chemical, isotope, transposon (P-element) and CRISPR/Cas9-mediated mutagenesis, UAS/Gal4-mediated conditional inactivation of gene expression through interfering RNA (RNAi) and ectopic gene expression, as well as lines with the visualized tissues of interest [3–11]. The targeted gene inactivation methods allow one to implement the reverse genetics approach involving inactivation of a gene of interest while investigating its phenotype/function in a living organism. The fruit fly is perfect for extensive genetic screens using the forward genetics approach as a means to identify mutations and gene function after detection of the phenotype of interest [12–14], and modified genetic screens aimed at identifying the genes involved in the process of interest [15–17]; (4) International repository centers preserve extensive collections of mutant *Drosophila* lines, including those with genetic deletions, point mutations and P-transposon, CRISPR/Cas9, promoter-Gal4, UAS-RNAi, and UAS-transgenes lines; (5) the fruit fly has a stable system for mutation maintenance, using balancing chromosomes and combining mutations through meiotic recombination; (6) it make feasible phenotype studies at the organismal level *in vivo*; and (7) The fly has a short life cycle (30 days), and the fly stocks are convenient and relatively inexpensive to store and maintain. The disadvantages of this popular model are (1) a huge evolutionary distance between insects and mammals and, as a consequence, insufficient homology at the genetic and physiological levels; (2) the fruit fly's small size makes it labor-intensive to process *Drosophila* tissues; and (3) the model limits the application of biochemical and immunochemical methods.

As a model system, *Drosophila* has been intensively used over the last 50 years in almost all areas of modern biology, from deciphering the molecular mechanism of apoptosis to investigations of aging mechanisms [3, 18–23]. It has also been widely used to investigate the molecular mechanisms of hematopoiesis and the humoral and cellular responses of innate immunity. The term hematopoiesis, meaning a process of blood cell formation, development, and maturation, has historically referred to the blood cells of vertebrates whose hematopoiesis is maintained by hematopoietic stem cells (HSCs), giving rise to a number of multipotent and restricted hematopoietic progenitors that differentiate into all types of blood cells such as red blood cells, platelets, leukocytes, and lymphocytes. In invertebrate coelomic organisms, to whom *Drosophila* belong, the internal body cavity contains coelomic fluid or hemolymph carrying hemocytes that are analogs of the blood cells of vertebrates [24–27]. Hematopoiesis in *Drosophila* is a process of multipotent progenitor cells maintenance and differentiation into three types of mature hemocytes occurring in several parts during life-cycle stages. It is important to note that insect hemocytes are functionally homologous to the myeloid cells of vertebrate innate immunity, with which they have evolved in parallel [28].

Dipteran insects have four life cycle stages; namely embryonic, larval, pupal, and imago. The main biological functions of *Drosophila* hemocytes are defensive, including the nonspecific humoral and cellular immune responses, participation in regenerative processes, and scavenging dead cells during ontogenesis. *Drosophila* is known to have three lines of mature hemolymph cells or hemocytes. They are plasmatocytes (PL), crystal cells (CCs), and lamellocytes (LM). The larval instars are characterized by significant growth and morphogenetic changes in the organism, accompanied by active defense against pathogenic microorganisms. During this stage, which is widely used to study hematopoiesis, the process of hematopoiesis occurs in the hematopoietic organ (HO) in which the temporal and spatial dynamics of progenitor cells maintenance and differentiation into all types of mature hemocytes can be observed. Investigations of *Drosophila* hematopoiesis have shown that the mechanisms that help maintain the multipotent hemocyte precursors of the fruit fly and of mammalian HSCs present significant differences. The *Drosophila* hematopoietic system does not have (or has not yet been identified to possess) *bona fide* multipotent stem cells that are analogous to the hematopoietic stem cells of vertebrates, which are maintained throughout life. Employing the *Drosophila* genetic model system has allowed for significant advances in deciphering and understanding the molecular mechanisms of hematopoiesis. The studies performed over the last two decades have demonstrated that the molecular mechanisms to maintain progenitor cells and ensure their differentiation into various hemocyte lineages are somewhat analogous to the processes of myeloid-cell differentiation regulation in mammals [27, 29]. To date, a number of comprehensive review papers have been published that cover many of the issues in this research field [27, 29–34]. This review discusses the major advances in the study of the molecular mechanisms of hematopoiesis in the *Drosophila* HO; these include regulation of multipotent progenitor cell maintenance and their differentiation by transcription factors, signaling pathways, and metabolic and environmental factors.

HEMATOPOIETIC SITES IN *DROSOPHILA*

In *Drosophila*, origin and formation of early progenitor cells, or preprohemocytes (PPHs), occur in two independent (cephalic and dorsal) regions of the embryonic mesoderm. That means hematopoiesis in *Drosophila* occurs in two independent pathways or "waves". In the first case, the cells of the cephalic mesoderm of the early embryo give rise to embryonic prohemocytes (PHs), which are further maintained and differentiate into the mature hemocytes that freely circulate in the hemolymph; hence they are named circulating hemocytes [35–38]. PHs (and their derivatives) of this origin are maintained in the circulating hemolymph during all subsequent stages of the insect's life cycle. The second wave occurs in the dorsal mesoderm, where the dorsal "blood" vessel, or "aorta" (DV, dorsal vessel), and the HO (originally named lymph gland) are formed (*Fig. 1*). However, the term HO is the most accurate for this organ [39–41]. This is a paired tissue formation consisting of hemocytes and their precursors bounded by an extracellular-matrix sheath. At the larval instars, the HO is the main site for maintaining PHs and differentiating them into mature hemocytes. During this stage, hemocytes do not leave the HO until the pupal stage begins. As for the circulating hemocytes, all their types are present in the hemolymph throughout the larval instars. When the pupal stage begins, the HO disintegrates and releases hemocytes, which then mix with the circulating ones. In this way, the PHs and the hemocytes originating from both sites of the mesoderm coexist during the postlarval stages of the fly's life cycle [36, 38, 42, 43].

DROSOPHILA HEMOCYTES

The mature hemocytes of the fruit fly are represented by three morphologically distinct types. These are plasmatocytes, phagocytic cells that perform defense, antimicrobial, and regulatory functions that comprise approximately 90–95% of hemocytes; crystal cells, non-phagocytic cells that make up 2–5% of hemocytes and are involved in wound healing, innate immunity reactions, and hypoxia; and lamellocytes, which are specialized giant cells that differentiate only in response to a parasitic organism invasion or upon tissue damage (*Fig. 1B*`). These cell types have been identified by ultrastructural studies and then confirmed by functional activity and molecular markers. Extensive studies have defined the signaling pathways and transcription factors that enable the specification, differentiation, and maintenance of these cell lines (see reviews [27, 29, 32]). Moreover, with single-cell RNA, sequencing (scRNAseq) has been detected in wide diversity in circulating hemocyte subgroups and eight of their subgroups with different functions have been identified using several experimental approaches [44–47]. In the HO, previously undescribed cell types have also been identified, such as early precursors, or PPHs, and adipohemocytes, a PL subtype [43]. To date, however, many recently identified hemocyte subsets remain poorly characterized and their molecular and functional features require further study.

Plasmatocytes

PLs are the main type of *Drosophila* blood cells that perform defense, immune, and homeostatic functions. These cells are phagocytes that participate in the inactivation of pathogens and the scavenging of apoptotic cells during organism development [26, 48–50]. PLs perform phagocytosis via the Croquemort (Crq), Eater, and Nimrod C1 (NimC1) receptors [51–54] and perform defense functions by secreting antimicrobial peptides (AMPs) (*Fig. 1B*`, *Table 1*) [55–57]. These cells secrete extracellular matrix (ECM) proteins, collagen IV, perlecan and laminin A, contributing to tissue formation [58, 59], and they synthesize peroxidasin (Pxn) [60], an enzyme meant to scavenge free radicals. PL ablation during embryogenesis engenders defects in organogenesis that lead to reduced embryo viability [61–64]. ScRNAseq-based identification of molecular markers has allowed researchers to distinguish four PL subtypes (*Fig. 1B*`) [43].

Crystal cells

Crystal cells are characterized by the fact that they contain the crystals of propenoloxidases 1 and 2 (PPO1 and 2) that are involved in melanization. These cells participate in defense reactions upon tissue damage, as well as in the innate immune response, primarily through the activation of a biochemical melanization cascade [65–68] that is functionally similar to the thrombosis cascade in mammals. Upon melanization, damaged tissues darken and harden, which is also associated with the production of reactive oxygen species (ROS) that participate in pathogen neutralization and healing of the damaged tissues (*Fig. 1B*`) [55, 65, 66, 69]. Suppressed melanization delays wound healing [70–72] and reduces susceptibility to microbial infections [65, 66]. CCs are unable to phagocyte; they express specific molecular markers and proliferate upon certain signals (see further, *Fig. 1B*`, *Table 1*). Using scRNAseq, two CC subtypes have been identified (CC1 and 2) [43].

Lamellocytes

Lamellocytes are large flat cells whose differentiation is induced by the signals from an invaded para-

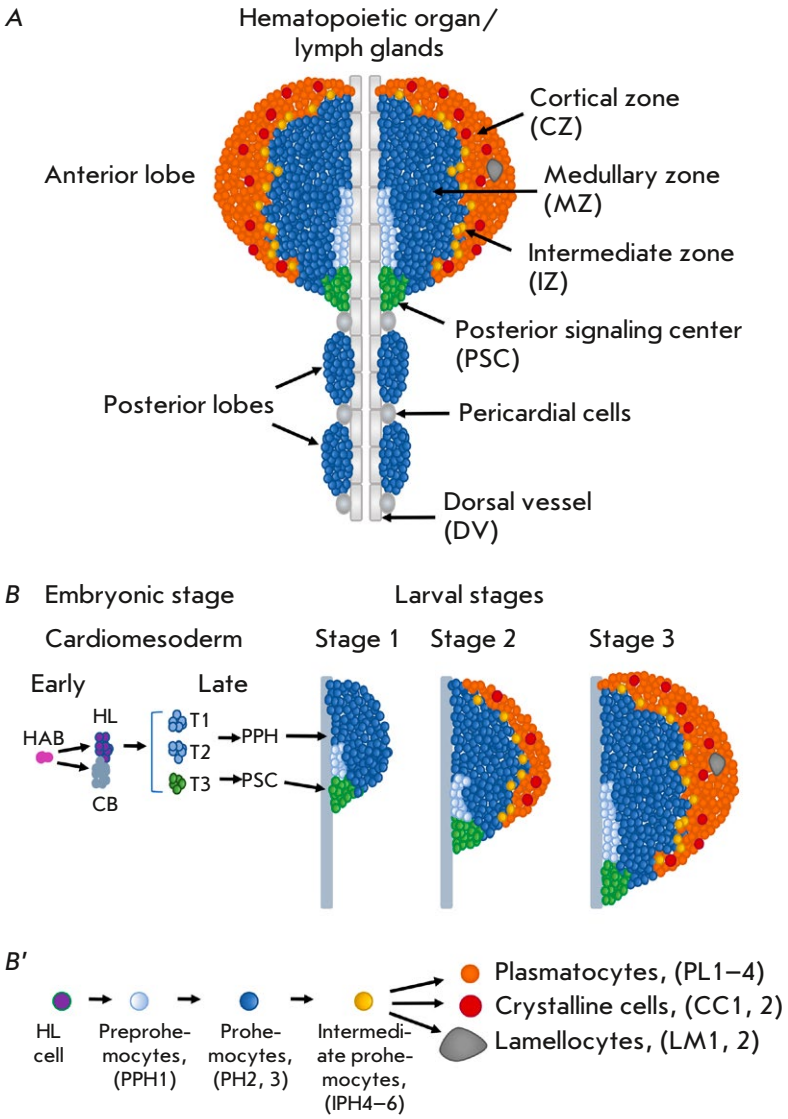

Fig. 1. (*A*) *Drosophila* hematopoietic organ (lymph gland of the third larval instar) structure. The HO consists of paired anterior and posterior lobes, attached and interacting with DV and pericardial cells. The anterior lobes of HO are a model system for studying *Drosophila* hematopoiesis. They consist of cell populations or cellular zones of the PSC (hematopoietic niche); the medullary zone (MZ) involving preprohemocyte (PPH) and prohemocyte (PH) populations; the cortical zone (CZ), consisting of differentiated hemocytes such as plasmatocytes (PLs), crystal cells (CCs), and lamellocytes (LMs); and intermediate prohemocytes (IPHs) of the intermediate zone (IZ). (*B*) Genesis of hematopoietic organ. At the early embryonic stage, cardiogenic mesoderm cells or hemangioblasts (HAB) give rise to hematopoietic lineage (HL) and cardiovascular precursor cells, cardioblasts (CB). At subsequent embryonic stages, three pairs of thoracic segments (T1–3) of cardiogenic mesoderm produce the HO's anterior pairs. Two anterior segments (T1–2) fuse and give rise to PPHs and all the hemocytes of the HO anterior lobe, while the third posterior segment produces PSC cells (highlighted in green). At the first instar larva, the anterior lobes contain PPH, PH, and PSC cells. At the second instar larva, PHs begin to differentiate into IPHs, which differentiate into plasmatocytes and CCs, forming the HO's CZ (these hemocyte lineages are highlighted in colors, as shown on panel *B′*). At the third larval stage, IPH differentiation into terminally differentiated hemocytes continues, accompanied by CZ growth. At this stage, MZ PHs are maintained in a mitotically quiescent state. (*B`*) Hematopoiesis occurring in the HO. Hematopoietic progenitor cells and differentiated hemocyte lineages are indicated, and the abbreviations of the subtypes of the hemocyte lineages detected by scRNAseq are shown in parentheses

sitic organism or an injury to tissue. The cellular immune response in *Drosophila* is mediated specifically by LMs and is mainly directed toward inactivating the eggs of parasitic wasps (*Leptopilina boulardi*) through their encapsulation [73, 74]. Plasmatocytes attach to the surface of an invading foreign object and then differentiate into LMs [75]. Mature LMs express specific molecular markers, and they are unable to divide or to phagocytize (*Fig. 1B`*, *Table 1*) [13, 26, 30, 51, 55, 66, 75–81]. Using scRNAseq, two LM subtypes have been identified in the HO (LM1 and 2) [43].

The features of the stem cells of the *Drosophila* hematopoietic system: prohemocytes

In mammals, HSCs are multipotent adult stem cells capable of self-renewing and differentiation into all blood cell types. They are maintained in a mitotically quiescent state, residing in the hematopoietic niches in bone marrow and other sites of hematopoiesis, where under certain external signals they undergo asymmetric division and further self-renewal and differentiation take place [82–85]. HSCs are capable of repopulating the niches and replenishing the entire blood-cell repertoire. In *Drosophila*, the stem cells capable of self-renewal throughout life include the male and female germlines, intestinal, and neuronal stem cells [86–89]. To date, no *bona fide* HSCs have been identified in the fruit fly, but early multipotent progenitor cells or preprohemocytes have been identified that are maintained by signals from the HO hematopoietic niche and DV cells. PPHs actively proliferate and give rise to more differentiated cells, namely prohemocytes. PHs are maintained in a mitotically quiescent state, and they are able to differentiate into all types of hemocytes [32, 38, 43, 90, 91]. It has not been established whether PPHs or PHs are capable of asymmetric division [92, 93] resulting in stem and differentiating daughter cells. The fact that *Drosophila*'s short life span frees it from the need to maintain and renew a large number of blood cells speaks in favor of its hematopoiesis mechanism being fundamentally different than that of HSC-based vertebrates.

DROSOPHILA HEMATOPOIETIC ORGAN: ZONES, CELLS AND MARKERS

Genesis of hematopoietic organ

Clonal analysis has demonstrated that HO and DV progenitor cells are derived from a common progenitor cell, the so-called hemangioblast. These cells divide into two daughter cells, one of which is a precursor of cardiovascular cells (cardioblasts) that differentiate into DV cells, and the other is a precursor of the cells of the hematopoietic lineage that gives rise to hemocytes [94]. It is plausible that a similar mechanism exists in the hemangioblasts of the vertebral aorta–gonad–mesonephros (AGM) region that produces hematopoietic and vascular cells in vertebrates [95]. The HO is formed from the three thoracic segments (T1–T3) expressing the Odd-skipped (Odd) and GATA Serpent (Srp) TFs (*Fig. 1*, *Table 1*) [94]. At the same time, Antennapedia (Antp) TF induce and specify T3 cells to form the so-called posterior signaling center (PSC) consisting of about 30–40 cells (Fig. 1B) [96]. The PSC is a hematopoietic niche controlling hematopoiesis in the larval HO [97]. The Collier TF (Col), controlled by Antp [96, 97], also participates in PSC maintenance. T1–T2 segments form primary HO lobes through the activity of the Homothorax (Hth) transcriptional cofactor (*Fig. 1B*) [96]. The Tinman (Tin) and GATA Pannier (Pnr) TF genes, Decapentaplegic (Dpp) morphogen ligand, and Heartless (Htl) fibroblast growth factor receptor are required for HO cell formation. In addition, the Wnt/Wingless (Wnt/Wg) signaling pathway positively regulates cardiogenic mesoderm specification [94].

Hematopoietic organ structure

The fruit fly's HO is a paired organ consisting of four lobes located along the aorta (*Fig. 1A*). The main lobe is the largest anterior or primary lobe of HO. In this lobe the coordinated processes PPH and PH maintenance and their proliferation and differentiation occur. The secondary, tertiary, and quaternary lobes are the least studied; they are several times smaller and serve as an additional source of hemocytes when a cellular immune response is activated [98]. The anterior lobe that is often called HO is the most structured part of the organ, so it has been used as a model or the main object to study the molecular mechanisms of hematopoiesis in *Drosophila* [41].

Several zones are distinguished in the anterior lobe, each of them containing functionally different types of cells that are at different stages of differentiation: (1) the PSC that functions as a niche for regulating the self-renewal and differentiation of prohemocytes; (2) the medially located medullary zone (MZ), consisting of PPHs and PHs; (3) the distally located cortical zone (CZ) where differentiation and accumulation of mature hemocytes takes place (*Fig. 1*) [41]; and (4) the intermediate zone (IZ) located between the medullary and cortical zones containing intermediate PHs (IPHs) and expressing both PH and mature-hemocyte markers (*Figs. 1* and *2*, *Table 1*) [43, 93, 99, 100].

Table 1. Molecular markers and genes involved in the specification and maintenance of hemocyte lineages during *Drosophila* hematopoiesis

Drosophila HO cells	Hemocyte-type molecular markers	Human genes homologous to hemocyte marker genes	Genes and factors involved in hemocyte-type specification and maintenance	Human genes homologous to Drosophila one
Embryonic hemangioblasts	Odd-skipped (Odd) Serpent (Srp)	OSR2 GATA1	*Odd* *Srp*	*OSR2* *GATA1*
PSC cells (embryonic T3 segment derivatives)	Antennapedia (Antp) Collier (Col) Hedgehog (Hh) Serrate (Ser) Wingless (Wg) Spitz (Spi) Pvf1	*HOXA7* *EBF1* *SHH* *JAG1* *WNT1* *EPGN* *FLT1,4*	*Antp* *Col* *Wg* *Fz2* *Myc* *Robo1,2* *Dpp* *Dad* *Mad*	*HOXA7* *EBF1* *WNT1* *FZD5* *MYC* *ROBO1,2,3* *BMP2* *SMAD6* *SMAD1*
Hematopoietic lineage (embryonic T1–2 segment PPHs)	Homothorax (Hth)	MEIS1	*Homothorax (Hth)* *Decapentaplegic (Dpp)* *Tinman (Tin)* *Pannier (Pnr)* *Heartless (Htl)* *Wingless/Wg*	*MEIS1* *BMP2* *NKX2-2* *GATA4* *FGFR3* *WNT1*
PPHs	*Dome*$^-$/Pvf2 *Notch-GAL4* *Su(H)-lacZ* *E(spl)mβ* Hand	*VEGF A–D* *NOTCH1* *RBPJ* *HES2* HAND1,2	*Odd* *Pvf2/Pvr* *Notch* *Dpp* *Mad* *Scalloped (Sd)*	*OSR2* *VEGF A–D* *NOTCH1* *BMP2* *SMAD1* *TEAD1*
PHs	*Dome*$^+$ E-cad Upd3 Wg	*PTPRQ* *CELSR1* – *WNT1*	*Patched (Ptc)* *Cubitus interruptus (Ci)* *Wg* *Wnt6* *β-catenin* *Fz2* *Col* *Stat92E* *AdoR* *Pka-C* *EGFR*	*PTCH1* *GLI3* *WNT1* *WNT6* *CTNNB1* *FZD5* *EBF1* *STAT5A* *ADORA2A* *PRKACB* *EGFR*
Intermediate PHs	*Dome*$^+$/Pxn$^+$ *Dome*$^+$/*Hml*$^+$		*EGFR* *Pointed (Pnt)*	*EGFR* *ETS1*
Plasmacytes	Peroxidasin (Pxn) *Hemollectin (Hml)* Nimrod (NimC) Eater Pvr	PXDN MUC5AC SCARF1 MEGF10 FLT1,4	*Thisbe (Ths)* *Heartless (Htl)* *Pointed (Pnt)* *u-shaped (Ush)* *Srp* *FoxO* *Pvr*	*FGF8* *FGFR3* *ETS1* *ZFPM1* *GATA1* *FOXO3* *FLT1,4*
CCs	Lozenge (Lz) Hindsight (Hnt) Sima/Hif-α Frizzled2 (Fz2) PPO1 and PPO2	*RUNX1,3* *RREB1* *HIF1A* *FZD5* –	*Notch* *Serrate (Ser)* *FoxO* *Fz2*	*NOTCH1* *JAG1* *FOXO3* *FZD5*
LMs	L1/Atilla Misshapen Myospheroid	– *MINK1* *ITGB1*	*EGFR* *FoxO* *Ph-p* *E(Pc)* *Col*	*EGFR* *FOXO3* *PHC3* *EPC1* *EBF1*

Note. Columns 3 and 5 indicate the human genes homologous to the corresponding *Drosophila* genes indicated in columns 2 and 4. The genes encoding the negative regulators of the corresponding hematopoiesis processes are marked in blue.

As noted above, the PSC was the first zone to emerge as a distinct cell population. Its cells regulate PH maintenance and differentiation in the HO's primary lobe throughout the larval stages. They perform only signaling functions and do not differentiate into hemocytes [43, 91, 96, 101–104]. PSC cells express such molecular markers as Antp, Col, the Hedgehog (Hh) signaling pathway ligand, the Serrate receptor (Ser) ligand of the Notch (N) signaling pathway, and the Wg ligand of the Wg/Wnt signaling pathway (*Fig. 2*, *Table 1*) [96, 97, 99, 105].

Until the mid-second larval instar, only *Dome*$^+$ prohemocytes expressing the *Domeless-Gal4 (Dome-Gal4)* reporter and a PPH population that does not express this reporter are present in the anterior lobe (see further). The *Dome*$^+$ PHs are maintained at the second and third larval instar and differentiate into mature hemocytes forming the CZ [6, 41, 90, 91, 99, 106]. A given population of PHs is capable of self-renewal while producing mature hemocytes [90]. Clonal analysis has shown that *Drosophila* hematopoietic "stem" cells can be located in close proximity to the PSC [90, 91]. The presence of this cell population, referred to as PPHs, or PH1, was confirmed by scRNAseq [43]. However, as has been mentioned previously, the self-renewal and asymmetric-division function characteristic of mammalian HSCs has not been identified in the hematopoietic "stem" cells of *Drosophila* [92, 93, 107]. At the first larval instar, *Dome*$^-$ PPHs are in direct contact with the dorsal aorta and the PSC. They are assumed to give rise to *Dome*$^+$ PHs [41, 43, 90, 91] that actively grow and divide during the first and early second larval instar [41, 91]. ScRNAseq has shown that *Dome*$^+$ PHs are a heterogeneous population consisting of two cell subtypes (PH 2,3), likely reflecting their differentiation hierarchy [43].

Dome$^+$ PH proliferation significantly decreases by the middle of the second larval instar. At the same time, cells at the distal edge of the MZ begin to differentiate, which is accompanied by decreased proliferation, increased granularity, and the absence of E-cadherin (E-cad) expression. MZ cells, or *Dome*$^+$ PHs, are characterized by high expression levels of Upd3 (JAK/STAT signaling pathway) and Wg ligands, E-cad and ROS [41, 99, 100, 108], and a low Col expression level [102, 109, 110]. ECM proteins, including type-IV collagen (Viking, Vkg) and Trol perlecan, have preferred localization between MZ cells [106, 111].

In the CZ, plasmatocytes express the following markers: Pxn, Hemollectin (Hml), Eater, and the P1 antigen or Nimrod-C (NimC) (*Fig. 1B'*, *Table 1*) [41, 56, 81, 99, 112, 113]. ScRNAseq has identified four plasmatocytes subtypes [43]. CCs express such transcription factors as Lozenge (Lz), Hindsight (Hnt), Sima/Hif-α, the Frizzled2 (Fz2) receptor, PPO1, and PPO2 [65, 78, 114–116]. In the absence of exposure to pathogenic factors, LMs hardly ever form in the CZ. Two LM subtypes are differentiated in the HO, expressing L1/Atilla, Misshapen, and integrin α-PS4 and its partner Myospheroid (*Fig. 1B`*, *Table 1*) [10, 43, 51, 55, 77, 80, 117].

Between *Dome*$^+$ PHs and differentiating Pxn$^+$ cells of the medullary and cortical zones reside a population of cells that simultaneously express markers of both zones. These are the so-called intermediate prohemocytes (IPHs) that represent the IZ (*Fig. 1*, *Table 1*) [34, 93, 99, 100, 118]. IPHs express the early differentiation markers Hml and Pxn, but they do not express the mature plasmatocytes marker (P1) and CCs marker (PPO1 and 2) [106]. They also cease to express E-cad. Recent scRNAseq studies have allowed for a more detailed characterization of this zone, which includes four stages of IPHs (PH4–6), early plasmatocytes (PL1), and early CCs (CC1) [43]. It has also been demonstrated that IPH cells are characterized by mitosis activation and differentiate into plasmatocytes and CCs if activated by the Ras/Raf or Ser/Notch signaling pathways, respectively [118]. The molecular mechanisms regulating this population are the least understood and require further investigations.

SIGNALING PATHWAYS INVOLVED IN MAINTENANCE AND DIFFERENTIATION OF PREPROHEMOCYTES

At the beginning of the first larval stage, the HO contains a population of multipotent PPHs, representing the earliest postembryonic population of hematopoietic progenitors that most likely disappear later than the first larval instar [91]. These cells are characterized by the lack of *Dome* PH marker expression, a low level of Dorothy (Dot)-marker expression, the activated Notch signaling pathway (*Notch-GAL4, Su(H)-lacZ*) and its target gene *enhancer of split mβ (E(spl)mβ)* (*Fig. 1*, *Table 1*) [43, 91]. In addition to Notch, maintenance of these cells is regulated by the Dpp ligand secreted by PSC cells. Dpp inactivation in the PSC or suppression of the mothers against the dpp (Mad) function in Notch$^+$ PPHs causes a significant reduction in the HO size by the 3rd larval instar. In other words, activation of the Notch and Dpp signaling pathways is required for PPH proliferation. During the 2nd and 3rd larval stages, *Dome*$^-$ PPHs begin to express the Hand and Scalloped (Sd) TFs [119]. These cells have been found to express the Pvf2 ligand of the Pvr receptor (human PDGF/VEGF receptor homolog), and its expression is dependent on Sd activity. Pvf2 inacti-

vation in these cells leads to a suppression of their proliferation and a significant subsequent reduction in HO size. At the same time, ectopic Pvf2 expression in these cells restores the proliferative defect in the HOs that have experienced partial loss of the Sd function [119].

The calcium/calmodulin signaling pathway activated through the ionotropic γ-aminobutyric acid receptor (GABABR) has also been shown to be involved in the maintenance of early *Dome*$^+$ PHs. GABABR is expressed in the PSC cells where the calcium/calmodulin pathway participates in the regulation of PPH proliferation at early larval stages without affecting hemocyte differentiation at the third larval instar. The disruption of the calcium/calmodulin pathway in PSC causes a significant decrease in PPH proliferation [120]. These data indicate there are several signaling pathways involved in the maintenance and proliferation of early *Dome*$^-$ PPHs, in particular Notch, Dpp, and Pvf2/Pvr (*Fig. 2*). The involvement of several pathways in the regulation of one process may be indicative of a complex regulation system and a possibility of mutual compensation. It should be noted that the technical difficulties in working with the HO at the first larval instar and the lack of markers make it difficult to study the *Dome*$^-$*Sd*$^+$ and *Dome*$^-$*Notch*$^+$ cell populations [91].

SIGNALING PATHWAYS INVOLVED IN MAINTENANCE AND DIFFERENTIATION PROHEMOCYTES

As previously mentioned, PHs are multipotent precursors of all hemocyte types. The multipotency and mitotic quiescence of these PHs is maintained through a variety of signals that come from three different sources (*Fig. 2*). The first type is the signals of the cytokines and growth factors secreted by the hematopoietic niche cells of the PSC. The second type is the autocrine or paracrine signals produced and received by the same population of cells in the HO's MZ. The third type is signals from differentiated cells in the CZ that are controlled by the maintaining and differentiating MZ PHs. The additional fourth type includes systemic signals originating from various tissues outside the HO that are mediated mainly through PSC in response to environmental factors.

A characteristic feature of PHs is a strictly coordinated control of their proliferation. At the first and early second larval instar, practically all HO cells, excluding PPHs and PSC cells, are *Dome*$^+$ PHs (*Fig. 1B*). At these stages, prohemocytes intensively and asynchronously proliferate. Then, when differentiated cells begin to appear at the late phase of the second larval instar, PH proliferation slows down abruptly. Further, during CZ formation, *Dome*$^+$ PHs practically cease to proliferate, while IZ and CZ cells continue at a higher proliferation rate throughout the entire third larval instar [41]. Therefore, a low proliferation rate and control over it correlate with maintenance of the prohemocyte multipotent state. As already mentioned, the four types of signals are necessary to maintain PHs in *Drosophila*: autocrine signals and signals coming from the PSC, differentiating cells, as well as signals from other tissues of the organism. Absence of any of these signals leads to the loss of PH multipotency and causes their proliferation and, consequently, differentiation [96, 103]. An important feature of PHs is correlation of their proliferation with an ability to differentiate. To date, a growing body of evidence seems to suggest that only proliferating PHs are able to accept differentiation signals, while resting PHs do not perceive them. Investigating the mechanisms regulation of the proliferative activity of intermediate PHs should contribute to a better understanding of this issue.

PSC SIGNALS REGULATE MAINTENANCE AND DIFFERENTIATION OF PROHEMOCYTES

Central role of the Hh/Ptc/Ci signaling pathway in maintaining a PH multipotent state

PSC cells act as a hematopoietic niche in the HO to secrete a number of signaling ligands or growth factors while they do not express corresponding receptors. At the same time, the receptors of these ligands are expressed in prohemocytes and the inactivation of corresponding ligands in PSC cells inhibits prohemocyte maintenance and causes them to differentiate.

The Hh ligand binding to its receptor Patched (Ptc) activates TF Cubitus interruptus (Ci). Hh is expressed exclusively in PSC cells during the second and third larval instar (*Fig. 1*, *Table 1*). While Ptc and activated Ci are expressed at a high level in *Dome*$^+$ prohemocytes, Hh inactivation does not affect PSC cells, but it stimulates the differentiation of *Dome*$^+$ PHs to differentiate into all three types of hemocytes [96, 97, 102–104, 121–124]. Besides, a suppressed Ci function causes PH differentiation, similar to the Hh inactivation in PSC cells (*Fig. 2*) [96, 121]. This process is enabled, among other things, due to the morphological features of PSC cells, whose prolong extended pseudopodia pass through several PH layers and allows delivery of the ligand deep inside the MZ [96, 102]. It has also been shown that PSC-cell ablation by apoptosis

induction does not cause the expected prohemocyte differentiation observed with the Hh inactivation [109, 110, 121]. However, it has been found that the *Dome*$^+$ PH population is heterogeneous. As such, a portion of the cells (Odd$^+$ Col$^-$) respond to the Hh signal, whereas Odd$^+$ Col$^+$ cells are not sensitive to it [110, 121]. In this regard, PSC-cell ablation is assumed not to affect certain prohemocytes. It is possible that Col$^+$ cells are a separate PH population that is controlled by signals from DV cells [91, 119]. It has also been found that the DV serves as an additional niche. Thus, the Branchless (Bnl) ligand (homologous to the fibroblast growth factor, FGF) produced by DV cells activates the FGF signaling pathway in PHs. When activated, it regulates the level of the intracellular calcium and contributes to PH maintenance in an undifferentiated state [125].

A suppressed *Roundabout* (*Robo*) gene function increases the number of PSC cells, and it also causes them to spread deeper into the HO. These events correlate with decreasing PL and CC differentiation [126]. At the same time, in response to a pathogenic invasion, the activity of the NF-kappaB Relish factor of the Imd signaling pathway is suppressed in PSC cells. The Relish inactivation manifests in the disruption of the PSC-cell cytoskeleton due to Jun-kinase activation, which leads to Hh-ligand retention thus disrupting the prohemocyte maintenance and causing their premature differentiation and activation of the cellular immune response [127]. It has also been shown that suppression of Ca^{2+} signaling or disruption of intercellular contacts between PSC cells affects their function and causes premature PH differentiation [128].

ROS regulate lamellocyte differentiation through the activation of the Spitz/EGFR and Toll/Dif signaling pathways in PSC cells

In addition to hematopoiesis regulation in the HO, PSC cells regulate lamellocyte differentiation inside and outside the HO. In this way, PSC-cell ablation through Col inactivation or apoptosis induction prevents differentiation of lamellocytes in response to a parasitic wasp infestation [97, 109]. Genetic methods have proved that this infestation leads to a significant increase in the ROS level in the PSC and that ROS are the key signal that induces lamellocyte differentiation [129]. ROS are not normally detected in PSC cells, but their level sharply increases when infected by parasitic wasps. Artificial increase in the ROS level in PSC cells due to the suppression of the mitochondrial respiratory chain also leads to a large-scale increase in the number of lamellocytes in the circulation and HO [129]. In both cases, ROS removal by mitochondrial superoxide dismutase 2 (SOD2) or catalase suppresses LM formation in the HO and circulation. In addition, activation of the Akt kinase signaling pathway (Akt1)/FoxO in PSC cells enhances the antioxidant response that abolishes LM generation. ROS have been shown to activate the epidermal growth factor receptor (EGFR) signaling pathway, enabling lamellocyte differentiation. Inactivation of Spitz (EGFR ligand) in PSC cells or the EGFR function in hemocytes suppresses LM formation (*Fig. 2*) [129]. The functions of the Star and Rhomboid proteins directly involved in the transport, cleavage, and activation of the Spitz ligand (its conversion into a soluble form), are necessary for LM induction. In addition, high ROS levels activate the Toll signaling pathway in PSC cells, which also contributes to LM induction in response to a parasitic wasp infestation [130]. Loss of the Toll signaling pathway components through inactivation of Dif and pelle disrupts LM formation. Along with many questions about the nature of ROS generation in PSC cells and signaling in response to a parasitic invasion, the question of interaction of the Spitz/EGFR and Toll/Dif signaling pathways in PSC cells in the regulation of LM differentiation remains unresolved.

LOCAL SIGNALS TO SUPPORT THE MULTIPOTENT PROPERTIES OF PROHEMOCYTES

Wg/Wnt/β-catenin signaling pathway

One of the important pathways involved in the maintenance of multipotency and self-renewal of mammalian hematopoietic stem cells is the Wnt/β-catenin signaling pathway. The Wnt ligand signals act in the both autocrine and paracrine ways. In the latter case, ligands are secreted from hematopoietic niche cells and contribute to HSC identity maintenance. In *Drosophila*, as in mammals, several genes encoding the Wnt ligands (Wg, Wnt-2, -3/5, -4, -6, -8, -10) and two genes encoding their receptors Fz and Fz2 are known. Ligands binding to the receptors cause activation of either the canonical pathway through the activation of β-catenin TF (Armadillo, Arm) or the non-canonical planar cell polarity signaling pathway, which activates transcription via JNK. The canonical Wg/Wnt/β-catenin signaling pathway is involved in the maintenance of the PH multipotent state (*Fig. 2*, *Table 1*) [99]. The Fz2 receptor that transduces signaling through the canonical pathway is expressed at a high level in *Dome*$^+$ PHs. Enhanced activation of the Wg/Wnt/β-catenin signaling pathway in *Dome*$^+$ PHs due to the overexpression of the Wg ligand

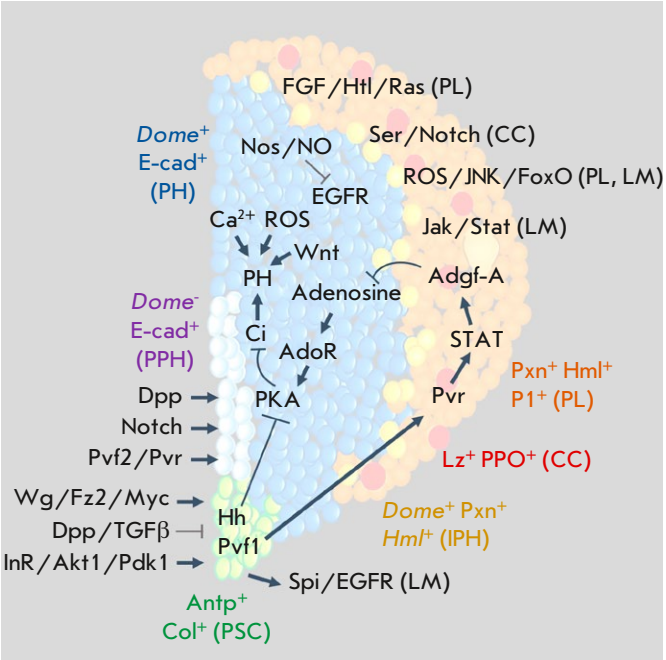

Fig. 2. Schematic representation of the participation and interaction of the main signaling pathways and TFs in the regulation of HO hematopoiesis in the fruit fly. PSC-cell (in green) maintenance and proliferation are positively and negatively controlled by the respective Wg/Fz2/Myc and Dpp/TGFβ signalling pathways. PPH (in grey) maintenance and proliferation are positively controlled by the Dpp, Notch, and Pvf2/Pvr signals. PH (in blue) maintenance (PH, blue) is positively controlled by the Hh/PKA/Ci signals from the hematopoietic niche, autocrine signals Wnt/Fz/Fz2 and Ca^{2+} and negatively controlled by the Adgf-A signal originating from differentiated CZ hemocytes (in orange). PSC cells positively control Adgf-A expression through activation of Pvr and STAT in differentiated CZ hemocytes, being a link in the equilibrium signals between PSC cells and the mature hemocytes that control PH maintenance. IPHs are marked in yellow. PL differentiation and proliferation is positively regulated by FGF/Htl/Ras and ROS/JNK/FoxO: those of CC, by Ser/Notch; and those of LM, by Spi/EGFR, Jak/Stat, and ROS/JNK/FoxO (see details in the text)

or the constitutively active form of β-catenin prevents these cells from differentiating and stimulating their maintenance in an undifferentiated state [99]. In turn, inhibition of this signaling pathway using a combination of dominant-negative forms of the Fz and Fz2 receptors in *Dome*$^+$ PHs causes disruption of HO zonation; i.e., clusters of differentiated cells "intermingle" with PH clusters (*Fig. 2*). Simultaneous expression of the dominant-negative forms of Fz and Fz2 increases the number of intermediate prohemocytes [99]. This suppresses E-cad expression, a protein that is directly involved in PH maintenance. E-cad suppression in PHs causes their differentiation, while E-cad overexpression promotes PH maintenance [41, 131]. Activation of the Wg/Wnt/β-catenin signaling pathway in *Hml*$^+$ cells of the CZ has also been shown to suppress the expression of the Tig ECM protein and affect plasmatocyte maturation [132, 133], which is additional indication of the function of this signaling pathway in the IZ cells. Recent studies have demonstrated that the Wnt6 ligand, whose expression is

controlled by the Hh signaling pathway, is also expressed in prohemocytes [134]. It is important to note that Wnt6 transmits signals through the new noncanonical Wnt-pathway mediated by the LRP6 receptor and suppressing β-catenin activity. The interaction of cytosolic β-catenin with E-cadherin suppresses the EGFR signaling pathway in PHs. Therefore, activation of the Wnt6/LRP6 pathway leads to cell cycle delay in the G2 phase, thus preventing prohemocytes from responding to signals for differentiation [134]. However, activation of the EGFR signaling pathway in intermediate prohemocytes of the IZ relieves cell cycle blockade by activating beta-catenin and allows cells to differentiate through Pointed (Pnt) TF activation [134]. Thus, activation of the signaling pathways – canonical Wg/beta-catenin and non-canonical Wnt6 – is important for maintaining PHs in a multipotent state, possibly in different PH populations, including that of IZ intermediate prohemocytes.

Calcium/calmodulin signaling pathway

The calcium/calmodulin signaling pathway is involved not only in the PSC-dependent regulation of preprohemocyte proliferation, but also in the maintenance of *Dome*$^+$ PHs (*Fig. 2*). Suppression of calcium signaling in prohemocytes leads to an increase in the number of differentiated hemocytes. On the contrary, activation of calcium signaling in PHs promotes their maintenance and proliferation, reducing significantly the number of formed mature hemocytes [120].

Collier factor activity

The Col TF is expressed in *Dome*$^+$ PHs, and its inactivation in these cells leads to their differentiation into plasmatocytes and CCs (*Table 1*) [109, 110]. The expression of this transcription factor in PHs is not controlled by signals from the PSC. At the same time, Col negatively regulates lamellocyte differentiation as well. A decrease in the level of Col has been observed during enhanced lamellocyte differentiation, while its ectopic expression in PHs prevents the formation of these cells. It remains unclear which signaling pathway activates the Col function in prohemocytes.

The FGF and Gbb/TGF-beta signaling pathways

Unlike Wnt, activation of the FGF signaling pathway in *Dome*$^+$ PHs differentiates them into mature hemocytes of all three types. Inhibition of the FGF signaling pathway causes a significant prohemocyte growth and the suppression of their differentiation. Interestingly, FGF ligand Thisbe (Ths) and the Htl receptor are expressed in PHs and in some, probably, IPHs expressing peroxidasin. Ectopic expression of the FGF-targeted transcription factors Pnt and Ush promotes prohemocyte differentiation [135]. Therefore, FGF signaling through Htl, Ras/MAPK, Pnt, and Ush promotes prohemocyte differentiation (*Fig. 2*). It has also been shown that the TGF-beta signaling pathway, through the Glass bottom boat (Gbb) ligand, is involved in the negative regulation of lamellocyte and plasmatocyte differentiation in the CZ through the suppression of the EGFR and JNK signaling pathways [136].

JAK/STAT signaling pathway

The Unpaired 1–3 (Upd1–3) cytokines acting through the Dome receptor activate the JAK kinase and Stat92E TF, inducing the transcription of target genes [102, 137]. It has been shown that the JAK/STAT signaling pathway is activated in *Dome*$^+$ prohemocytes to maintain their identity and prevent differentiation [41, 119, 137]. The Stat92E TF activity in PHs is much lower than that in differentiated CZ hemocytes [138]. However, the Stat92E TF function is essential for PH maintenance. Stat92E inactivation by a temperature-sensitive mutation leads to PH differentiation [102]. At the same time, the inactivation of JAK/STAT signaling pathway components such as Dome or JAK kinase (hopscotch, hop), or Stat92E in MZ prohemocytes, does not affect their maintenance [103, 139]. The Ush TF regulated by JAK/STAT signaling has been shown to promote the expression of E-cad and Ptc in PHs, thus participating in their maintenance and differentiation suppression [131, 140]. The Asrij (Arj) protein is involved in the phosphorylation and activation of STAT. Arj inactivation partially phenocopies the temperature-sensitive Stat92E allele that suppresses PH maintenance and induces their differentiation [141, 142]. In addition, the JAK/STAT signaling pathway positively regulates PH differentiation into lamellocytes upon cellular immune response induction (*Fig. 2*, *Table 1*) [137].

ROS are involved in the maintenance of prohemocytes

The main ROS sources in the cell are the mitochondrial respiratory chain and membrane NADPH-oxidases (NOX). They generate superoxide anion radicals which then are converted into hydrogen peroxide by superoxide dismutases. The main cellular ROS forms are hydrogen peroxide and a superoxide anion radical. ROS are powerful oxidizing agents, so upon their high concentrations and when a cellular antioxidant system is disturbed,

they cause irreversible changes in macromolecules, provoking cell aging and death. However, sublethal and physiological ROS concentrations serve as important signaling mediators involved in posttranslational modifications of signaling pathway proteins and transcription factors, thereby regulating various processes in the cell [143, 144]. Unexpectedly, it has turned out that increased ROS levels are normally maintained in the *Dome*$^+$ PHs, being in mitotic quiescence if compared to differentiated CZ hemocytes (*Fig. 2*, *Table 1*) [100]. By analogy with quiescent mammalian HSCs, it can be assumed that these cells have low mitochondrial/respiratory activity and, consequently, low ROS levels. At the same time, mammalian myeloid precursors are known to have significantly higher ROS levels than that in HSCs, which also increases during differentiation of myeloid lineage cells. The mechanism used to generate increased ROS levels in prohemocytes remains unclear. ROS have been shown to function as signaling molecules during prohemocyte differentiation. Expression of antioxidant enzymes reduces the basal ROS level in *Dome*$^+$ PHs and suppresses mature hemocytes formation. At the same time, induction of ROS excess and oxidative phosphorylation attenuation by the inactivation of mitochondrial respiratory chain complex I through the JNK signaling pathway in prohemocytes lead to their differentiation into the three types of mature hemocytes [100]. The increased ROS level in PHs also leads to a decrease in E-cad expression through the activated JNK signaling pathway and TF Srp [145]. Ectopic expression of the FoxO TFs of the JNK pathway in PHs causes their differentiation into plasmatocytes and crystal cells [100, 145]. Simultaneous FoxO activation and inactivation of the chromatin proteins Polyhomeotic proximal (Ph-p) and the Enhancer of polycomb (E(Pc)) causes PH differentiation into lamellocytes (*Fig. 2*, *Table 1*). Therefore, a moderately high but physiologically controlled ROS level is necessary for PH maintenance. However, increased production of mitochondrial ROS in PHs causes their differentiation by activation of the JNK/FoxO signaling pathway. It is noteworthy that in this context the FoxO function does not mediate antioxidant genes regulation. It has also been found that the putative PHs of the *Drosophila* larval circulation outside the HO produce high levels of ROS. These PHs have not yet been well characterized and are referred to as progenitors by analogy with the HO prohemocytes expressing increased levels of ROS and the Wg ligand [17]. These cells are generated in large excess due to the activity of the oncogenic chimeric AML1-ETO protein forcefully expressed in *Hml*$^+$ hemocytes. High ROS levels in such circulating PHs contribute to their maintenance and increased proliferation. The ectopic expression of the antioxidant enzyme SOD2 or catalase (Catalase, Cat), as well as of FoxO that activates their expression, is able to suppress the generation and excessive proliferation of hemocytes and their progenitors, all caused by the AML1-ETO oncogene [17]. In this case, it is most likely that the Akt1/FoxO signaling pathway canonically regulates antioxidant genes expression. Thus, similarities and significant differences can be observed in the regulation of the maintenance of the HO PHs and circulating PHs by ROS.

It has recently been shown that nitric oxide synthase (Nos) is particularly expressed in prohemocytes and that, through the production of nitric oxide (NO), it is involved in the posttranslational S-nitrosylation of the proteins on cysteine residues [146]. S-nitrosylation of proteins, together with cytosolic calcium, activates the Ire1-Xbp1-mediated unfolded protein response (UPR) necessary to maintain PHs in a mitotically inactive state by maintaining them in the G2 phase of the cell cycle [146]. As already mentioned, such a cell cycle block makes prohemocytes refractory to the paracrine factors inducing differentiation. It has also been shown that EGFR S-nitrosylation temporarily inactivates this receptor and, thus, renders the PHs unresponsive to the relevant signals. It is important to note that the Nos expressed in prohemocytes does not contain a reductase domain but is capable of generating NO [146]. In turn, since these cells have high ROS levels, this form of Nos can utilize ROS to synthesize NO. For that reason, it has been suggested that the interaction between ROS and NO may participate in the maintenance of appropriate levels of ROS by generating NO, and, thereby, protecting PHs from excessive ROS production.

In general, it has become evident that there is a complex network that regulates PH maintenance and differentiation in the HO and that involves several signaling pathways for local regulation of these processes. At the same time, there might be complex network interactions between the components of these signaling pathways in certain time intervals of *Drosophila* hematopoiesis. Different signaling pathways are able to induce cell differentiation, which may be indicative of the increased plasticity of *Drosophila* hematopoietic progenitor cells. Apart from these signals and the signals from the PSC, prohemocyte maintenance is controlled by signals from differentiated cells. This will be discussed in the next section.

EQUILIBRIUM SIGNALS BETWEEN PSC CELLS AND MATURE CORTICAL HEMOCYTES REGULATE PROHEMOCYTE MAINTENANCE

The *Drosophila* genetic system has been used to identify a unique mechanism that regulates progenitor-cell maintenance. It has been found that prohemocyte maintenance and differentiation are controlled "in equilibrium" by two mechanisms: (1) directly by a signal from PSC cells; and (2) by the signal of differentiated daughter cells, which is also controlled by an additional signal originating from the same hematopoietic niche. PSC cells regulate not only the maintenance of the PH multipotent state, but also the maintenance and differentiation of CZ hemocytes (*Fig. 2*). This process is regulated by the Pvf1/Pvr signaling pathway [103]. The Pvf1 ligand is secreted in PSC cells, while the Pvr receptor is expressed at high levels in cortical-zone cells. Inactivation of Pvf1 in PSC cells does not affect their proliferation and number, but it suppresses PH maintenance, causing their differentiation. A similar effect is observed when the Pvr receptor function is suppressed in differentiated hemocytes of the CZ, causing extensive PH differentiation [103, 119]. It is important that the Pvf1 ligand is transported for long distances across multiple cells by transport vesicles that include bound-but-not-signaling complexes of Pvf1 and Pvr on the prohemocyte plasma membrane.

With the use of genetic methods it has been demonstrated that Pvf1, when interacting with Pvr of cortical hemocytes, activates the STAT-dependent expression of secreted adenosine deaminase of growth factor-A (Adgf-A) (*Fig. 2*). This enzyme deaminates adenosine, converting the extracellular signaling molecules of adenosine into inert inosine [147, 148]. Deletion of adenosine by Adgf-A in CZ hemocytes leads to the suppression of the corresponding signaling pathway through the adenosine receptor (AdoR) located in PHs. As a result, the activity of cAMP-dependent protein kinase A (PKA) is reduced, which, in turn, activates the transcription factor Ci that mediates the PH maintenance in a multipotent state. It is important to note that the activation of the Hh/Ptc signaling pathway from the PSC also inhibits PKA activity in PHs, which leads to Ci activation. Therefore, the Hh-dependent signal from PSC cells and the adenosine signal from differentiated CZ hemocytes synergistically inhibit PKA activity and activate Ci, promoting prohemocyte maintenance in the MZ [96, 103]. These data could be a sign that a similar equilibrium signal may also operate in the mammalian hematopoietic system.

SIGNALING PATHWAYS MAINTAINING THE PSC-CELL FUNCTION

The Antp and Col TFs are expressed in PSC cells throughout all larval instar. These cells proliferate during the early larval instar and form a cluster of 30–40 cells that is maintained during the third larval instar (*Fig. 1*). Antp directly controls the specification, maintenance, and growth of these cells and activates the expression of Col, which in turn is involved in the maintenance of Antp expression [96, 97, 116]. The Serrate ligand of the Notch receptor is expressed later in a certain population of PSC cells and is required for CC differentiation in the CZ [96, 97, 105]. Two signaling pathways, Wg and Dpp, antagonistically regulate PSC-cell proliferation [99, 123]. All components of the Wg signaling pathway, Fz2, β-catenin/Arm, and Disheveled (Dsh) are expressed in the PSC. Wg activation is necessary to increase the number of PSC cells (*Fig. 2*, *Table 1*). Blocking the Fz2 function significantly decreases the number of PSC cells, while the ectopic expression of Wg leads to a significant increase in their number [99]. In contrast to Wg, suppression of the Dpp/TGF-beta signaling pathway increases the number of PSC cells [123]. Activation of the TGF-beta signaling pathway through the Dpp ligand ectopic expression activates the Daughters against the dpp (Dad) and Mad TFs expressed in PSC cells [123, 149]. The number of PSC cells significantly increases when this pathway is suppressed through inactivation of the Dally like (Dlp) heparan sulfate-proteoglycan-binding protein and pMad in these cells (*Fig. 2*). Simultaneous suppression of the Wg and Dpp signaling pathways restores the PSC to its wild-type size. The regulation of the number of PSC cells by Wg is Myc-dependent, since Myc inactivation reverses the increase in PSC cells caused by ectopic Wg expression [123]. In its turn, the Jumu TF of the fork head family is involved in Myc regulation while the last regulates PSC-cell proliferation [150]. Further studies are required for a detailed understanding of how these signaling pathways interact for the regulation of PSC-cell proliferation and functioning.

Studies have shown that the developed network of extracellular matrix proteins between PSC cells and PHs is important for the regulation of Dpp and Wg signaling during hematopoiesis in HO andin response to stress [151]. It has been found that the septated contacts between PSC cells are destroyed upon activation of the Toll or Imd signaling pathways or in response to a bacterial infection. Usually, the PSC-cell cluster is impermeable to large-molecule dyes. However, inactivation of

the dense septated intercellular contact proteins Coracle (Cora) or Neurexin IV (Neurexin IV, NrxIV) leads to PSC-cell permeabilization. The increased permeability increases the number of PSC cells, decreases that of PHs, and promotes plasmatocyte and crystal cell differentiation. Losing such a barrier impairs Wg and Dpp ligand signaling [151] both within the niche and signaling to PHs. It has been shown that gap junctions (GJ) and the Ca^{2+}-signaling pathway are involved in the regulation of Hh secretion [128].

In addition, the signals from the DV cells adjacent to the PSC have been proven to regulate proliferation, function, and localization of PSC cells. So, the glycoprotein Slit is secreted in the DV cells, whose receptors Roundabout 1 and 2 (Robo 1 and 2) are expressed on PSC cells. The interaction of Slit with Robo 1 and 2 regulates PSC-cell proliferation and localization [33, 126, 152]. Suppression of the Robo function in PSC or Slit expression in DV cells increases the number of PSC cells and causes them to expand deep into the HO, including through suppressed E-cad expression [126]. In turn, Robo activates the Dpp/TGF-beta signaling pathway, which suppresses the Myc TF expression and PSC cell proliferation (*Fig. 2*) [33, 123, 126].

Another important discovery has been that outside signals, namely from the nervous and humoral systems, directly affect the state and function of PSC cells. Insulin-like peptides expressed in neurons, glia, and fat body cells [153] regulate the proliferation and growth of PSC cells through insulin signaling pathway activation [31, 32, 104, 122, 154]. Inhibition of this pathway through inactivation of its various components such as the insulin receptor (InR), Akt1, phosphoinositide-dependent kinase 1 (Pdk1), and phosphoinositide-3-kinase (PI3K) reduces the number of PSC cells. It has also been discovered that activation of the rapamycin signaling pathway is involved in this process. Further studies will investigate the interactions between the detected signaling pathways and their role in the regulation of maintenance and functioning of the cells of the hematopoietic niche, which is central in regulating hematopoiesis in *Drosophila*'s hematopoietic organ.

CONCLUSION

Over the past 20 years, significant progress has been made in our understanding of the molecular mechanisms regulating hematopoiesis in the fruit fly. As the most genetically advanced model system, *Drosophila* has allowed us to describe the complex interactions between signaling pathways and the TFs involved in the regulation of the maintenance and differentiation of multipotent hemocyte precursor cells, namely preprohemocytes and prohemocytes. These cells differentiate during larval development into three types of mature hemocytes: plasmatocytes, crystal cells, and lamellocytes. It has been shown that in insects, as in mammals, the main role in the maintenance and regulation of the differentiation of hematopoietic progenitor cells is played by hematopoietic niche cells – PSC cells. Determination of these cells' fate occurs in parallel with the specification of hematopoietic progenitors in the HO. Throughout the larval instar, PSC cells coordinate prohemocyte maintenance and differentiation through secreted ligands (Hh, Pvf1, Ser, Wg/Wnt), activating the appropriate signaling pathways in hemocyte precursors. These signals are involved, among others, in the maintenance of the autocrine and paracrine signals (Wnt/ beta-catenin, calcium signaling, AFC, Stat92E) in prohemocytes, activating or inhibiting their maintenance in an undifferentiated state. Prohemocytes are maintained in a mitotically quiescent state in the MZ of the hemopoietic organ. In addition, a two-way equilibrium regulation of prohemocyte maintenance has been proven to take place through signals from differentiated (Pvr, Adgf-A, AdoR, PKA) and PSC cells (Hh, Pvf1). Recent studies using single-cell transcriptome sequencing have shown the presence of intermediate stages of prohemocyte differentiation and uncharacterized populations of mature hemocytes. Prohemocyte differentiation occurs in the so-called intermediate zone, where cells begin to divide and become susceptible to differentiation signals. But this mechanism requires further investigation. In addition, recent studies have shown that DV cells also serve as a type of hematopoietic niche, participating in prohemocyte maintenance. To date, HSCs capable of self-renewal by asymmetric cell division have not been identified in *Drosophila*. However, the most naive preprohemocyte population has been identified. These cells are regulated by PSC cells via the activation of the Notch, Dpp, and Pvf2/Pvr signaling pathways. In addition to maintaining hemocyte precursors, PSC cells participate in the regulation of the cellular immune response and the cells mediating melanization and inactivation of pathogenic objects through the Spi/EGFR, Toll, and Ser/Notch signaling pathways. Based on the results of the reviewed studies, a unique picture of the interaction of the molecular mechanisms regulating hematopoiesis in one of the representatives of arthropods has emerged. The genetic model of *Drosophila* has allowed us to de-

cipher the molecular events that regulate hematopoiesisin greater detail, and in some aspects, has proven to be ahead of the murine model. ●

This research was financially supported by Agreement with the Ministry of Education and Science of the Russian Federation No. 075-15-2021-1075 of 28-09-2021.

REFERENCES

1. Morgan T.H. // Sci. Mon. 1935. V. 41. № 1. P. 5–18.
2. Morgan T.H. // Am. Nat. 1917. V. 51. № 609. P. 513–544.
3. Nefedova L.N. // Russ. J. Dev. Biol. 2020. V. 51. № 4. P. 201–211.
4. Osadchiy I.S., Kamalyan S.O., Tumashova K.Y., Georgiev P.G., Maksimenko O.G. // Acta Naturae. 2023. V. 15. № 2. P. 70–74.
5. Brand A.H., Perrimon N. // Development. 1993. V. 118. № 2. P. 401–415.
6. Evans C.J., Olson J.M., Ngo K.T., Kim E., Lee N.E., Kuoy E., Patananan A.N., Sitz D., Tran P., Do M.-T. et al. // Nat. Meth. 2009. V. 6. № 8. P. 603–605.
7. Hu Y., Comjean A., Rodiger J., Liu Y., Gao Y., Chung V., Zirin J., Perrimon N., Mohr S. E. // Nucleic Acids Res. 2021. V. 49. № D1. P. D908–D915.
8. Cooley L., Kelley R., Spradling A. // Science. 1988. V. 239. № 4844. P. 1121–1128.
9. Bokel C. // Methods Mol. Biol. 2008. V. 420. P. 119–138.
10. Braun A., Lemaitre B., Lanot R., Zachary D., Meister M. // Genetics. 1997. V. 147. № 2. P. 623–634.
11. Nemudryi A.A., Valetdinova K.R., Medvedev S.P., Zakian S.M. // Acta Naturae. 2014. V. 6. № 3. P. 19–40.
12. Friedman A., Perrimon N. // Curr. Opin. Genet. Dev. 2004. V. 14. № 5. P. 470–476.
13. Sinenko S.A., Kim E.K., Wynn R., Manfruelli P., Ando I., Wharton K.A., Perrimon N., Mathey-Prevot B. // Dev. Biol. 2004. V. 273. № 1. P. 48–62.
14. Kaufman T. C. // Genetics. 2017. V. 206. № 2. P. 665–689.
15. St Johnston D. // Nat. Rev. Genet. 2002. V. 3. № 3. P. 176–188.
16. Reitman Z.J., Sinenko S.A., Spana E.P., Yan H. // Blood. 2015. V. 125. № 2. P. 336–345.
17. Sinenko S.A., Hung T., Moroz T., Tran Q.M., Sidhu S., Cheney M.D., Speck N.A., Banerjee U. // Blood. 2010. V. 116. № 22. P. 4612–4620.
18. Hales K.G., Korey C.A., Larracuente A.M., Roberts D.M. // Genetics. 2015. V. 201. № 3. P. 815–842.
19. Schneider D. // Nat. Rev. Genet. 2000. V. 1. № 3. P. 218–226.
20. Perrimon N. // Proc. Natl. Acad. Sci. USA. 1998. V. 95. № 17. P. 9716–9717.
21. Celniker S.E., Rubin G.M. // Annu. Rev. Genomics Hum. Genet. 2003. V. 4. P. 89–117.
22. Sinenko S.A. // Oncotarget. 2017. V. 8. № 41. P. 70452–70462.
23. Yang C.S., Sinenko S.A., Thomenius M.J., Robeson A.C., Freel C.D., Horn S.R., Kornbluth S. // Cell Death Differ. 2014. V. 21. № 4. P. 604–611.
24. Shrestha R., Gateff E. // Dev. Growth. Differ. 1982. V. 24. № 1. P. 65–82.
25. Mathey-Prevot B., Perrimon N. // Cell. 1998. V. 92. № 6. P. 697–700.
26. Lanot R., Zachary D., Holder F., Meister M. // Dev. Biol. 2001. V. 230. № 2. P. 243–257.
27. Evans C.J., Hartenstein V., Banerjee U. // Dev. Cell. 2003. V. 5. № 5. P. 673–690.
28. Millar D.A., Ratcliffe N.A. // Endeavour. 1989. V. 13. № 2. P. 72–77.
29. Evans C.J., Sinenko S.A., Mandal L., MartinezAgosto J.A., Hartenstein V., Banerjee U., Rolf B. Genetic Dissection of Hematopoiesis Using *Drosophila* as a Model System // Advances in Developmental Biology: Elsevier, 2007. P. 259.
30. Honti V., Csordas G., Kurucz E., Markus R., Ando I. // Dev. Comp. Immunol. 2014. V. 42. № 1. P. 47–56.
31. Koranteng F., Cho B., Shim J. // Mol. Cells. 2022. V. 45. № 3. P. 101–108.
32. Banerjee U., Girard J.R., Goins L.M., Spratford C.M. // Genetics. 2019. V. 211. № 2. P. 367–417.
33. Morin-Poulard I., Tian Y., Vanzo N., Crozatier M. // Front. Immunol. 2021. V. 12. P. 719349.
34. Kharrat B., Csordas G., Honti V. // Int. J. Mol. Sci. 2022. V. 23. № 14. P. 7767.
35. Tepass U., Fessler L.I., Aziz A., Hartenstein V. // Development. 1994. V. 120. № 7. P. 1829–1837.
36. Holz A., Bossinger B., Strasser T., Janning W., Klapper R. // Development. 2003. V. 130. № 20. P. 4955–4962.
37. Honti V., Csordas G., Markus R., Kurucz E., Jankovics F., Ando I. // Mol. Immunol. 2010. V. 47. № 11–12. P. 1997–2004.
38. Ghosh S., Singh A., Mandal S., Mandal L. // Dev. Cell. 2015. V. 33. № 4. P. 478–488.
39. Srdić Ž., Reinhardt C. // Science. 1980. V. 207. № 4437. P. 1375–1377.
40. Gateff E. // Science. 1978. V. 200. № 4349. P. 1448–1459.
41. Jung S.H., Evans C.J., Uemura C., Banerjee U. // Development. 2005. V. 132. № 11. P. 2521–2533.

42. Rugendorff A., Younossi-Hartenstein A., Hartenstein V. // Rouxs Arch. Dev. Biol. 1994. V. 203. № 5. P. 266–280.
43. Cho B., Yoon S.H., Lee D., Koranteng F., Tattikota S.G., Cha N., Shin M., Do H., Hu Y., Oh S. Y., et al. // Nat. Commun. 2020. V. 11. № 1. P. 4483.
44. Cattenoz P.B., Monticelli S., Pavlidaki A., Giangrande A. // Front. Cell Dev. Biol. 2021. V. 9. P. 643712.
45. Fu Y., Huang X., Zhang P., van de Leemput J., Han Z. // J. Genet. Genomics. 2020. V. 47. № 4. P. 175–186.
46. Cattenoz P.B., Sakr R., Pavlidaki A., Delaporte C., Riba A., Molina N., Hariharan N., Mukherjee T., Giangrande A. // EMBO J. 2020. V. 39. № 12. P. e104486.
47. Tattikota S.G., Cho B., Liu Y., Hu Y., Barrera V., Steinbaugh M.J., Yoon S.H., Comjean A., Li F., Dervis F., et al. // Elife. 2020. V. 9. P. e54818.
48. Russo J., Dupas S., Frey F., Carton Y., Brehelin M. // Parasitology. 1996. V. 112 (Pt 1). P. 135–142.
49. Brehelin M. // Cell Tissue. Res. 1982. V. 221. № 3. P. 607– 615.
50. Charroux B., Royet J. // Proc. Natl. Acad. Sci. USA. 2009. V. 106. № 24. P. 9797–9802.
51. Kurucz E., Vaczi B., Markus R., Laurinyecz B., Vilmos P., Zsamboki J., Csorba K., Gateff E., Hultmark D., Ando I. // Acta Biol. Hung. 2007. V. 58 Suppl. P. 95–111.
52. Franc N.C., Heitzler P., Ezekowitz R.A., White K. // Science. 1999. V. 284. № 5422. P. 1991–1994.
53. Kocks C., Cho J. H., Nehme N., Ulvila J., Pearson A. M., Meister M., Strom C., Conto S. L., Hetru C., Stuart L. M., et al. // Cell. 2005. V. 123. № 2. P. 335–346.
54. Bretscher A.J., Honti V., Binggeli O., Burri O., Poidevin M., Kurucz E., Zsamboki J., Ando I., Lemaitre B. // Biol. Open. 2015. V. 4. № 3. P. 355–363.
55. Irving P., Ubeda J.M., Doucet D., Troxler L., Lagueux M., Zachary D., Hoffmann J.A., Hetru C., Meister M. // Cell. Microbiol. 2005. V. 7. № 3. P. 335–350.
56. Kurucz E., Markus R., Zsamboki J., Folkl-Medzihradszky K., Darula Z., Vilmos P., Udvardy A., Krausz I., Lukacsovich T., Gateff E. et al. // Curr. Biol. 2007. V. 17. № 7. P. 649–654.
57. Balandin S., Ovchinnikova T. // Russ. J. Bioorganic Chem. 2016. V. 42. № 3. P. 229–248.
58. Olofsson B., Page D.T. // Dev. Biol. 2005. V. 279. № 1. P. 233–243.
59. Bunt S., Hooley C., Hu N., Scahill C., Weavers H., Skaer H. // Dev. Cell. 2010. V. 19. № 2. P. 296–306.
60. Nelson R.E., Fessler L.I., Takagi Y., Blumberg B., Keene D.R., Olson P.F., Parker C.G., Fessler J.H. // EMBO J. 1994. V. 13. № 15. P. 3438–3447.
61. Defaye A., Evans I., Crozatier M., Wood W., Lemaitre B., Leulier F. // J. Innate Immun. 2009. V. 1. № 4. P. 322–334.
62. Sears H.C., Kennedy C.J., Garrity P.A. // Development. 2003. V. 130. № 15. P. 3557–3565.
63. Guillou A., Troha K., Wang H., Franc N.C., Buchon N. // PLoS Pathog. 2016. V. 12. № 10. P. e1005961.
64. Shia A.K., Glittenberg M., Thompson G., Weber A.N., Reichhart J.M., Ligoxygakis P. // J. Cell Sci. 2009. V. 122. № 24. P. 4505–4515.
65. Binggeli O., Neyen C., Poidevin M., Lemaitre B. // PLoS Pathog. 2014. V. 10. № 5. P. e1004067.
66. Dudzic J.P., Kondo S., Ueda R., Bergman C.M., Lemaitre B. // BMC Biol. 2015. V. 13. P. 81.
67. Tang H., Kambris Z., Lemaitre B., Hashimoto C. // J. Biol. Chem. 2006. V. 281. № 38. P. 28097–28104.
68. Nam H.J., Jang I.H., You H., Lee K.A., Lee W.J. // EMBO J. 2012. V. 31. № 5. P. 1253–1265.
69. Nappi A.J., Vass E., Frey F., Carton Y. // Eur. J. Cell. Biol. 1995. V. 68. № 4. P. 450–456.
70. Ramet M., Manfruelli P., Pearson A., Mathey-Prevot B., Ezekowitz R.A. // Nature. 2002. V. 416. № 6881. P. 644–648.
71. Galko M.J., Krasnow M.A. // PLoS Biol. 2004. V. 2. № 8. P. E239.
72. Neyen C., Binggeli O., Roversi P., Bertin L., Sleiman M.B., Lemaitre B. // Dev. Comp. Immunol. 2015. V. 50. № 2. P. 166–174.
73. Rizki T.M., Rizki R.M. // Dev. Comp. Immunol. 1992. V. 16. № 2–3. P. 103–110.
74. Shrestha R., Gateff E. // Development, Growth and Differentiation. 1982. V. 24. № 1. P. 83–98.
75. Anderl I., Vesala L., Ihalainen T.O., Vanha-Aho L.M., Ando I., Ramet M., Hultmark D. // PLoS Pathog. 2016. V. 12. № 7. P. e1005746.
76. Nam H.J., Jang I.H., Asano T., Lee W.J. // Mol. Cells. 2008. V. 26. № 6. P. 606–610.
77. Honti V., Kurucz E., Csordas G., Laurinyecz B., Markus R., Ando I. // Immunol. Lett. 2009. V. 126. № 1–2. P. 83–84.
78. Tokusumi T., Shoue D.A., Tokusumi Y., Stoller J.R., Schulz R.A. // Genesis. 2009. V. 47. № 11. P. 771–774.
79. Evans C.J., Liu T., Banerjee U. // Methods. 2014. V. 68. № 1. P. 242–251.
80. Rus F., Kurucz E., Markus R., Sinenko S.A., Laurinyecz B., Pataki C., Gausz J., Hegedus Z., Udvardy A., Hultmark D., et al. // Gene Expr. Patterns. 2006. V. 6. № 8. P. 928–934.
81. Sinenko S.A., Mathey-Prevot B. // Oncogene. 2004. V. 23. № 56. P. 9120–9128.
82. Semenova N.Y., Bessmel'tsev S.S., Rugal' V.I. // Klin. Onkogematol. 2014. V. 7. № 4. P. 501–510.
83. Charbord P., Pouget C., Binder H., Dumont F., Stik G., Levy P., Allain F., Marchal C., Richter J., Uzan B., et al. // Cell Stem Cell. 2014. V. 15. № 3. P. 376–391.
84. Belyavsky A., Petinati N., Drize N. // Int. J. Mol. Sci. 2021. V. 22. № 17. P. 9231.
85. Comazzetto S., Shen B., Morrison S. J. // Dev. Cell. 2021. V. 56. № 13. P. 1848–1860.
86. Morrison S.J., Spradling A.C. // Cell. 2008. V. 132. № 4. P. 598–611.
87. Fuller M.T., Spradling A.C. // Science. 2007. V. 316. № 5823. P. 402–404.
88. Homem C.C., Knoblich J.A. // Development. 2012. V. 139. № 23. P. 4297–4310.
89. Micchelli C.A., Perrimon N. // Nature. 2006. V. 439. № 7075. P. 475–479.
90. Minakhina S., Steward R. // Development. 2010. V. 137. № 1. P. 27–31.
91. Dey N.S., Ramesh P., Chugh M., Mandal S., Mandal L. // Elife. 2016. V. 5. P. e18295.
92. Ho K.Y.L., Carr R.L., Dvoskin A.D., Tanentzapf G. // Elife. 2023. V. 12. P. e84085.
93. Girard J.R., Goins L.M., Vuu D.M., Sharpley M.S., Spratford C.M., Mantri S.R., Banerjee U. // Elife. 2021. V. 10. P. e67516.
94. Mandal L., Banerjee U., Hartenstein V. // Nat. Genet.

2004. V. 36. № 9. P. 1019–1023.
95. Medvinsky A., Dzierzak E. // Cell. 1996. V. 86. № 6. P. 897–906.
96. Mandal L., Martinez-Agosto J.A., Evans C.J., Hartenstein V., Banerjee U. // Nature. 2007. V. 446. № 7133. P. 320–324.
97. Crozatier M., Ubeda J.M., Vincent A., Meister M. // PLoS Biol. 2004. V. 2. № 8. P. E196.
98. Rodrigues D., Renaud Y., VijayRaghavan K., Waltzer L., Inamdar M. S. // Elife. 2021. V. 10. P. e61409.
99. Sinenko S.A., Mandal L., Martinez-Agosto J.A., Banerjee U. // Dev. Cell. 2009. V. 16. № 5. P. 756–763.
100. Owusu-Ansah E., Banerjee U. // Nature. 2009. V. 461. № 7263. P. 537–541.
101. Crozatier M., Meister M. // Cell. Microbiol. 2007. V. 9. № 5. P. 1117–1126.
102. Krzemien J., Dubois L., Makki R., Meister M., Vincent A., Crozatier M. // Nature. 2007. V. 446. № 7133. P. 325–328.
103. Mondal B.C., Mukherjee T., Mandal L., Evans C.J., Sinenko S.A., Martinez-Agosto J. A., Banerjee U. // Cell. 2011. V. 147. № 7. P. 1589–1600.
104. Tokusumi Y., Tokusumi T., Shoue D.A., Schulz R.A. // PLoS One. 2012. V. 7. № 7. P. e41604.
105. Lebestky T., Jung S.H., Banerjee U. // Genes Dev. 2003. V. 17. № 3. P. 348–353.
106. Krzemien J., Oyallon J., Crozatier M., Vincent A. // Dev. Biol. 2010. V. 346. № 2. P. 310–319.
107. Mohammad K., Dakik P., Medkour Y., Mitrofanova D., Titorenko V.I. // Int. J. Mol. Sci. 2019. V. 20. № 9. P. 2158.
108. Hombria J.C., Brown S., Hader S., Zeidler M.P. // Dev. Biol. 2005. V. 288. № 2. P. 420–433.
109. Benmimoun B., Polesello C., Haenlin M., Waltzer L. // Proc. Natl. Acad. Sci. USA. 2015. V. 112. № 29. P. 9052–9057.
110. Oyallon J., Vanzo N., Krzemien J., Morin-Poulard I., Vincent A., Crozatier M. // PLoS One. 2016. V. 11. № 2. P. e0148978.
111. Grigorian M., Liu T., Banerjee U., Hartenstein V. // Dev. Biol. 2013. V. 384. № 2. P. 301–312.
112. Makhijani K., Alexander B., Tanaka T., Rulifson E., Bruckner K. // Development. 2011. V. 138. № 24. P. 5379–5391.
113. Goto A., Kadowaki T., Kitagawa Y. // Dev. Biol. 2003. V. 264. № 2. P. 582–591.
114. Mukherjee T., Kim W. S., Mandal L., Banerjee U. // Science. 2011. V. 332. № 6034. P. 1210–1213.
115. Terriente-Felix A., Li J., Collins S., Mulligan A., Reekie I., Bernard F., Krejci A., Bray S. // Development. 2013. V. 140. № 4. P. 926–937.
116. Lebestky T., Chang T., Hartenstein V., Banerjee U. // Science. 2000. V. 288. № 5463. P. 146–149.
117. Tokusumi T., Sorrentino R.P., Russell M., Ferrarese R., Govind S., Schulz R. A. // PLoS One. 2009. V. 4. № 7. P. e6429.
118. Spratford C.M., Goins L.M., Chi F., Girard J.R., Macias S.N., Ho V.W., Banerjee U. // Development. 2021. V. 148. № 24. P. 200216.
119. Ferguson G.B., Martinez-Agosto J.A. // Dev. Biol. 2017. V. 425. № 1. P. 21–32.
120. Shim J., Mukherjee T., Mondal B.C., Liu T., Young G.C., Wijewarnasuriya D.P., Banerjee U. // Cell. 2013. V. 155. № 5. P. 1141–1153.
121. Baldeosingh R., Gao H., Wu X., Fossett N. // Dev. Biol. 2018. V. 441. № 1. P. 132–145.
122. Benmimoun B., Polesello C., Waltzer L., Haenlin M. // Development. 2012. V. 139. № 10. P. 1713–1717.
123. Pennetier D., Oyallon J., Morin-Poulard I., Dejean S., Vincent A., Crozatier M. // Proc. Natl. Acad. Sci. USA. 2012. V. 109. № 9. P. 3389–3394.
124. Khadilkar R.J., Rodrigues D., Mote R.D., Sinha A.R., Kulkarni V., Magadi S.S., Inamdar M.S. // Proc. Natl. Acad. Sci. USA. 2014. V. 111. № 13. P. 4898–4903.
125. Destalminil-Letourneau M., Morin-Poulard I., Tian Y., Vanzo N., Crozatier M. // Elife. 2021. V. 10. P. e64672.
126. Morin-Poulard I., Sharma A., Louradour I., Vanzo N., Vincent A., Crozatier M. // Nat. Commun. 2016. V. 7. P. 11634.
127. Ramesh P., Dey N. S., Kanwal A., Mandal S., Mandal L. // Elife. 2021. V. 10. P. e67158.
128. Ho K.Y.L., An K., Carr R.L., Dvoskin A.D., Ou A.Y.J., Vogl W., Tanentzapf G. // Proc. Natl. Acad. Sci. USA. 2023. V. 120. № 45. P. e2303018120.
129. Sinenko S.A., Shim J., Banerjee U. // EMBO Rep. 2012. V. 13. № 1. P. 83–89.
130. Louradour I., Sharma A., Morin-Poulard I., Letourneau M., Vincent A., Crozatier M., Vanzo N. // Elife. 2017. V. 6. P. e25496.
131. Gao H., Wu X., Fossett N. // Molecular and Cellular Biology. 2009. V. 29. № 22. P. 6086–6096.
132. Zhang C.U., Cadigan K.M. // Development. 2017. V. 144. № 13. P. 2415–2427.
133. Zhang C.U., Blauwkamp T.A., Burby P.E., Cadigan K.M. // PLoS Genet. 2014. V. 10. № 8. P. e1004509.
134. Goins L.M., Girard J.R., Mondal B.C., Buran S., Su C.C., Tang R., Biswas T., Banerjee U. // bioRxiv. 2023. 10.1101/2023.06.29.547151. P. 2023.2006.2029.547151.
135. Dragojlovic-Munther M., Martinez-Agosto J.A. // Dev. Biol. 2013. V. 384. № 2. P. 313–330.
136. Zhang W., Wang D., Si J., Jin L. H., Hao Y. // Cells. 2023. V. 12. № 4. P. 661.
137. Makki R., Meister M., Pennetier D., Ubeda J.M., Braun A., Daburon V., Krzemien J., Bourbon H.M., Zhou R., Vincent A., et al. // PLoS Biol. 2010. V. 8. № 8. P. e1000441.
138. Flaherty M.S., Salis P., Evans C. J., Ekas L. A., Marouf A., Zavadil J., Banerjee U., Bach E.A. // Dev. Cell. 2010. V. 18. № 4. P. 556–568.
139. Minakhina S., Tan W., Steward R. // Dev. Biol. 2011. V. 352. № 2. P. 308–316.
140. Gao H., Wu X., Fossett N. // PLoS One. 2013. V. 8. № 9. P. e74684.
141. Kulkarni V., Khadilkar R.J., Magadi S.S., Inamdar M.S. // PLoS One. 2011. V. 6. № 11. P. e27667.
142. Sinha A., Khadilkar R.J., S V.K., Roychowdhury Sinha A., Inamdar M. S. // Cell Rep. 2013. V. 4. № 4. P. 649–658.
143. Sinenko S.A., Starkova T.Y., Kuzmin A.A., Tomilin A.N. // Front. Cell Dev. Biol. 2021. V. 9. P. 714370.
144. Lennicke C., Cocheme H.M. // Mol. Cell. 2021. V. 81. № 18. P. 3691–3707.
145. Gao H., Wu X., Simon L., Fossett N. // PLoS One. 2014. V. 9. № 9. P. e107768.
146. Cho B., Shin M., Chang E., Son S., Shin I., Shim J. // Dev. Cell. 2024. V. 59. № 8. P. 1075–1090.
147. Dolezal T., Dolezelova E., Zurovec M., Bryant P. J. //

PLoS Biol. 2005. V. 3. № 7. P. e201.
148. Bajgar A., Dolezal T. // PLoS Pathog. 2018. V. 14. № 4. P. e1007022.
149. Belenkaya T.Y., Han C., Yan D., Opoka R.J., Khodoun M., Liu H., Lin X. // Cell. 2004. V. 119. № 2. P. 231–244.
150. Hao Y., Jin L.H. // Elife. 2017. V. 6. P. e25094.
151. Khadilkar R.J., Vogl W., Goodwin K., Tanentzapf G. // Elife. 2017. V. 6. P. e28081.
152. Labrosse C., Eslin P., Doury G., Drezen J.M., Poirie M. // J. Insect Physiol. 2005. V. 51. № 2. P. 161–170.
153. Nassel D.R., Liu Y., Luo J. // Gen. Comp. Endocrinol. 2015. V. 221. P. 255–266.
154. Dragojlovic-Munther M., Martinez-Agosto J.A. // Development. 2012. V. 139. № 20. P. 3752–3763.

Evaluation of HER2/neu Expression in Metastatic Axillary Lymph Node Tissue of Breast Cancer Patients Using [^{99m}Tc]Tc-(HE)$_3$-G3

O. D. Bragina[1,2*], L. A. Tashireva[1], D. M. Loos[1,3], S. V. Vtorushin[1,3], A. A. Shulga[2,4], E. N. Konovalova[2,4], M. E. Borodina[5], V. I. Chernov[1,2,6], V. M. Tolmachev[7], S. M. Deyev[2,4,6]
[1]Tomsk Cancer Research Institute, Tomsk, 634009 Russian Federation
[2]National Research Tomsk Polytechnic University, Tomsk, 634050 Russian Federation
[3]Siberian State Medical University, Tomsk, 634050 Russian Federation
[4]Shemyakin–Ovchinnikov Institute of Bioorganic Chemistry, Moscow, 117997 Russian Federation
[5]Hertsen Moscow Oncology Research Institute, Moscow, 125284 Russian Federation
[6]National Research Center Kurchatov Institute, Moscow, 123098 Russian Federation
[7]Uppsala University, Uppsala, 75185 Sweden
*E-mail: bragina_od@mail.ru
Received: June 08, 2024; in final form, June 26, 2024
DOI: 10.32607/actanaturae.27448

ABSTRACT **Anatomic visualization and molecular typing of metastatic regional lymph nodes in breast cancer patients are a serious clinical challenge in modern oncology. According to the results of previous studies, [^{99m}Tc]Tc-(HE)$_3$-G3 has proven to be a promising diagnostic agent in differentiating the HER2/neu receptor status in primary breast tumors ($p < 0.05$, Mann–Whitney test). In this regard, the purpose of this study is to explore the possibilities of using [^{99m}Tc]Tc-(HE)$_3$-G3 to determine the HER2/neu receptor status in the metastatic axillary lymph nodes (mALNs) of breast cancer patients. The study was conducted using clinical material from 20 breast cancer patients (T2-4N1-3M0-1) before systemic therapy (10 patients with positive and 10 patients with negative HER2/neu expression in mALNs) who underwent SPECT/CT scan 4 h after the administration of [^{99m}Tc]Tc-(HE)$_3$-G3. Morphological and immunohistochemical studies of mALNs with assessment of the HER2/neu status were performed on all patients. We found that mALN-to-background and mALN-to-latissimus dorsi muscle ratios for [^{99m}Tc]Tc-(HE)$_3$-G3 uptake 4 h after its administration may be used for typing of the HER2/neu status in mALNs of breast cancer patients ($p < 0.05$, Mann–Whitney test). In that case, sensitivity and specificity for the mALN-to-background ratio were identical at 80%, with the threshold value being > 12.25.**

KEYWORDS **breast cancer, lymph node metastasis, DARPinG3, HER2/neu, radionuclide diagnostics.**

ABBREVIATIONS **BC – breast cancer; US – ultrasound; CT – computed tomography; HER2/neu – human epidermal growth factor receptor-2; RP – radiopharmaceutical; mALN – metastatic axillary lymph node; IHC – immunohistochemistry; FISH – fluorescence *in situ* hybridization; ASCO/CAP – American Society of Clinical Oncology and College of American Pathologists; SPECT – single-photon emission computed tomography; LDM – latissimus dorsi muscle; SUV – standardized uptake value.**

INTRODUCTION

The condition of regional lymph nodes in breast cancer (BC) is an important prognostic factor that is significant both in choosing the modality of local and systemic therapies for these patients and in assessing the prognosis of the disease [1]. Unfortunately, traditional diagnostic methods, such as ultrasound (US), mammography, magnetic resonance imaging, and computed tomography (CT), are not characterized by high sensitivity and specificity levels in differentiating normal and metastatic lymph node structures, which leads to a large number of false-positive and

false-negative results in preclinical cancer staging [2, 3]. However, there is a need not only for anatomical detection, but also for assessing the molecular profile of all identified metastatic foci, which is an important factor in the evaluation of the tumor spread and the determination of indications for prescribing directed (targeted) therapy in BC patients, an approach that significantly improves overall and relapse-free survival rates [4, 5].

In recent years, there has been an active effort to investigate targeted radionuclidic imaging techniques that could help detect a specific molecular target [6, 7]. A particular example is the results of studies using alternative scaffold proteins that are labeled with various radioisotopes and targeted at human epidermal growth factor receptor-2 (HER2/neu) [8, 9]. These constructs offer optimal characteristics in delivering a diagnostic isotope to a target antigen: high specificity and affinity, low toxicity, and rapid elimination from the patient's body, which significantly reduces the time from agent injection to the onset of a diagnostic procedure [10–12].

For example, the data of phase I clinical trials of the agents [^{99m}Tc]Tc-ADAPT6 (ClinicalTrials.gov Identifier: NCT03991260 and ClinicalTrials.gov Identifier: NCT05412446) and ^{99m}Tc-ZHER2:41071 (ClinicalTrials.gov Identifier: NCT05203497) performed at the Department of Radionuclide Therapy and Diagnostics of the Cancer Research Institute of the Tomsk National Research Medical Center (CRI TNRMC) demonstrated that it is possibile to determine HER2/neu status in the primary tumor [13, 14] and metastatic lymph nodes in BC patients [15]. Another agent promising for targeted radionuclide diagnosis of HER2-positive breast cancer is a designed ankyrin repeat protein (DARPinG3) molecule that is constructed on the basis of 14 to 21 kDa ankyrin proteins and exhibits a high tropism for epidermal growth factor receptor type 2 [16]. The data of preclinical *in vitro* studies of [^{99m}Tc]Tc-$(HE)_3$-G3 [17] demonstrated its rapid binding to the HER2/neu receptor and slow internalization in SKOV3 and BT-74 cell lines, as well as a higher uptake in HER2-positive SKOV3 xenografts compared with that in HER2-negative Ramos xenografts and a low liver uptake in *in vivo* studies. A phase I clinical trial of [^{99m}Tc]Tc-$(HE)_3$-G3 (ClinicalTrials.gov Identifier: NCT05695859) at a dose of 3,000 μg showed that it was safe for BC patients and highly specific in assessing the HER2/neu status in the primary tumor using SPECT without CT [18].

The purpose of this study was to investigate the possibility of the clinical use of the radiopharmaceutical [^{99m}Tc]Tc-$(HE)_3$-G3 in order to determine the HER2/neu status in the metastatic axillary lymph nodes of BC patients and identify optimal parameters for determining the receptor's positive and negative status.

EXPERIMENTAL

Protein production

DARPin$(HE)_3$-G3 (amino acid sequence: MRGSHEHEHEGSDLGKKLLEAARAGQDDEVRILMANGADVNAKEYGLTPYLATAHGHLEIVEVLLKNGADVNAVDAIGFTPLHLAAFIGHLEIAEVLLKHGADVNAQDKFGKTAFDISIGNGNEDLAEILQKLN) was synthesized at the Institute of Biological Chemistry.

Characterization of clinical material

This was an open, non-randomized, and prospective study that started after registration at ClinicalTrials.gov (Identifier: NCT15122022), approval by the bioethical committee of CRI TNRMC, and the completion of an informed consent form by patients before administration of the radiopharmaceutical. The study included 20 BC patients with metastatic axillary lymph nodes (mALNs) (T2-4N1-3M0-1) before the start of systemic or local treatment. Human epidermal growth factor receptor HER2/neu expression in mALNs was positive in 10 patients (n = 10) and negative in 10 patients (n = 10). The mean age of the patients included in the study was 49.6 years.

At the preclinical stage, all patients underwent a comprehensive clinical and instrumental examination according to the 2023 Russian Society of Clinical Oncology (RUSSCO) protocols. The presence, anatomical location, and size of tumor nodes in the mammary gland and axillary region were determined using US. The mean primary tumor size was 24 ± 5 mm, and the mean metastatic axillary lymph node size was 20 ± 3 mm.

Morphological and immunohistochemical studies

In all the cases, morphological and immunohistochemical (IHC) studies of the biopsy and/or surgical material of metastatic axillary nodes were performed to determine the HER2/neu status of the largest lymph node using standard methods. The surgical material of patients who had started treatment directly from the surgical stage was studied. Metastatic lymph nodes were marked for IHC analysis under US guidance by placing a localization mark before surgical treatment. HER2/neu expression with IHC 3+ or IHC 2+ and a positive FISH (fluorescence *in situ* hybridization) was considered positive, and that with IHC 0 or 1+ was considered negative, which corresponded

Table 1. [^{99m}Tc]Tc-(HE)$_3$-G3 uptake in mALNs (SUV_{max}) and reference organs and mALN-to-reference organ ratios in BC patients

	SUV_{max} (mALN)	SUV_{max} (background mALN)	mALN/ background	SUV_{max} (liver)	SUV_{max} (LDM)	SUV_{max} (spleen)	mALN/ liver	mALN/ LDM	mALN/ spleen
HER2-positive mALNs									
1	1.8	0.3	6.7	9.1	0.3	4.0	0.2	6.2	0.5
2	2.6	0.2	15.2	5.2	0.3	2.5	0.5	8.6	1.04
3	2.2	0.2	13.5	3.0	0.3	1.3	0.7	6.2	1.7
4	10.7	0.3	33.3	4.7	0.4	2.5	2.3	26.0	4.3
5	8.7	0.3	34.9	5.7	0.4	2.1	1.5	21.3	4.2
6	2.4	0.4	5.9	4.1	0.2	1.7	0.6	10.9	1.5
7	14.0	0.3	41.2	2.9	0.5	3.1	4.9	25.9	4.5
8	6.5	0.1	50.3	8.7	0.4	4.2	0.8	17.7	1.6
18	8.7	0.4	23.5	3.4	0.3	4.4	2.6	27.2	1.9
19	4.8	0.1	36.9	6.9	0.3	0.1	0.7	15.0	4.8
	6.2 ± 4.2	0.3 ± 1.1	26.1 ± 15.4	5.4 ± 2.2	0.34 ± 0.1	2.6 ± 1.4	1.5 ± 1.4	16.5 ± 8.3	2.6 ± 1.6
HER2-negative mALNs									
9	3.9	0.5	8.6	6.3	0.5	2.1	0.6	8.4	1.8
10	3.1	0.4	8.5	15.2	0.2	8.1	0.2	21.1	0.3
11	1.2	0.1	11.0	0.6	0.3	4.9	2.2	4.5	0.2
12	0.5	0.2	2.3	2.7	0.0	0.4	0.2	13.2	1.3
13	3.8	0.3	13.7	9.7	0.7	5.6	0.4	5.2	0.7
14	6.8	0.4	18.9	6.2	0.6	1.9	1.1	11.4	3.5
15	6.8	0.7	10.4	10.3	0.8	3.7	0.7	8.7	1.8
16	1.0	0.7	1.5	13.8	0.5	6.6	0.1	2.1	0.1
17	5.6	0.5	10.8	10.1	0.6	2.5	0.6	9.5	2.3
20	1.7	0.4	4.5	1.5	0.3	0.9	1.2	5.6	1.8
	3.4 ± 2.4	0.4 ± 0.2	9.0 ± 5.3	7.6 ± 5.0	0.5 ± 0.2	3.7 ± 2.6	0.7 ± 0.6	8.9 ± 5.4	1.4 ± 1.1

Note: mALN is a metastatic axillary lymph node; LMS is the latissimus dorsi muscle.

to the 2018 ASCO/CAP (American Society of Clinical Oncology and College of American Pathologists) criteria [19, 20]. IHC was a reference method, and its data were compared with data from the radionuclide analysis.

Preparation of the radiopharmaceutical

The radiopharmaceutical [^{99m}Tc]Tc-(HE)$_3$-G3 in a dose of 3,000 μg was prepared immediately before intravenous administration to patients at the Department of Radionuclide Therapy and Diagnostics of CRI TNRMC using the protocol described previously [18]. [^{99m}Tc]Tc-(HE)$_3$-G3 was purified by size-exclusion chromatography using sterilized NAP-5 columns (Sephadex G-25, GE, Healthcare, Chicago, IL, USA) pre-equilibrated and eluted with a sterile sodium phosphate buffer. The purified fraction was brought to a volume of 10 mL using a sterile isotonic NaCl solution. A 2 μL aliquot of the compound solution was used for pH determination and radiochemical purity analysis. The pH of the radiopharmaceutical solutions was determined using pH test strips. Radiochemical purity was analyzed using instant thin layer chromatography (Agilent Technologies, Santa Clara, CA, USA).

Radionuclide study protocol

[^{99m}Tc]Tc-(HE)$_3$-G3 uptake was assessed by measuring the maximum standardized uptake (SUV$_{max}$) in mALNs, the projections of contralateral axillary lymph nodes, and those of reference organs, such as the liver, latissimus dorsi, and spleen 4 h after its administration. Additionally, parameters such as mALN-to-background and mALN-to-reference organs were calculated for each patient (*Table 1*). SUV$_{max}$ was determined in the largest mALN based on the anatomical location corresponding to the US description and biopsy sampling.

Radionuclide studies in BC patients 4 h after administration were performed on a Siemens Symbia Intevo Bold gamma camera equipped with a low-power and high-resolution collimator. In all cases, SPECT/CT of the chest and upper abdomen with reconstruction was performed using the xSPECT protocol (Siemens). The images were processed using the Syngo.via software (Siemens).

Statistical methods

Data were analyzed and visualized using the Prism 10 software (GraphPad). Values are presented as a mean ± standard deviation (M ± SD) or median and interquartile range (Me(Q1–Q3)). The differences in organ uptake at different time points were analyzed using the one-way analysis of variance (ANOVA). The nonparametric Mann–Whitney test was used to evaluate the significance of the differences between the parameters of HER2-positive and HER2-negative tumors. ROC analysis was performed to evaluate the predictive values of the parameters. All criteria were two-sided, and the differences were considered significant at $p < 0.05$.

RESULTS

IHC studies

The immunohistochemical analysis revealed that the HER2/neu receptor status was identical in the primary tumors and mALNs of all BC patients included in the study.

[^{99m}Tc]Tc-(HE)$_3$-G3 labeling and radionuclidic studies

Labeling of the radiopharmaceutical (*Fig. 1*) and radionuclidic imaging in all BC patients included in the study were performed according to the protocols described in the Experimental section. The radiochemical purity of [^{99m}Tc]Tc-(HE)$_3$-G3 was 98.7 ± 1.8%. The mean administered dose activity was 435 ± 138 MBq.

[^{99m}Tc]Tc-(HE)$_3$-G3 uptake in metastatic and contralateral axillary lymph nodes

mALNs were visualized in all BC patients, regardless of the HER2/neu status (*Fig. 2*). Quantitative data on [^{99m}Tc]Tc-(HE)$_3$-G3 uptake in anatomical structures are shown in *Table 1*.

There were no differences in SUV$_{max}$ among BC patients with different HER2/neu statuses in mALNs (6.2 ± 4.2 for positive expression and 3.4 ± 2.4 for negative expression) (p = 0.1230, Mann–Whitney test). However, there were statistical differences in the mALN-to-background ratios: it was higher in the subgroup of patients with a HER2-positive mALN status (26.1 ± 15.4) than in the subgroup with a

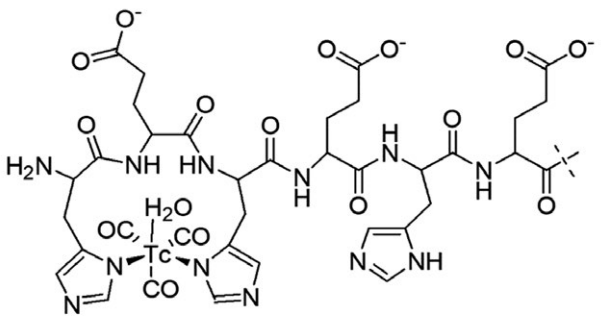

Fig. 1. Schematic of the labeling of technetium-99m with a DARPinG3 molecule using the tricarbonyl technique

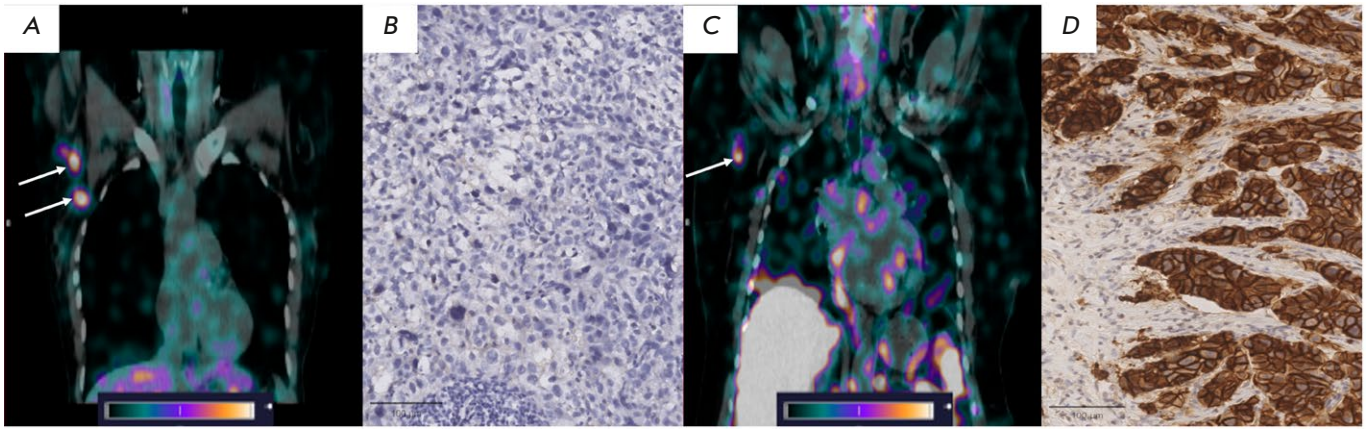

Fig. 2. [^{99m}Tc]Tc-(HE)$_3$-G3 uptake in mALNs of BC patients 4 h after administration: (*A*) – [^{99m}Tc]Tc-(HE)$_3$-G3 uptake in HER2-positive mALNs (indicated by white arrows); (*B*) – IHC imaging of a HER2-positive mALN (×400); (*C*) – [^{99m}Tc]Tc-(HE)$_3$-G3 uptake in a HER2-negative mALN (indicated by the white arrow); (*D*) – IHC imaging of a HER2-negative mALN (×400)

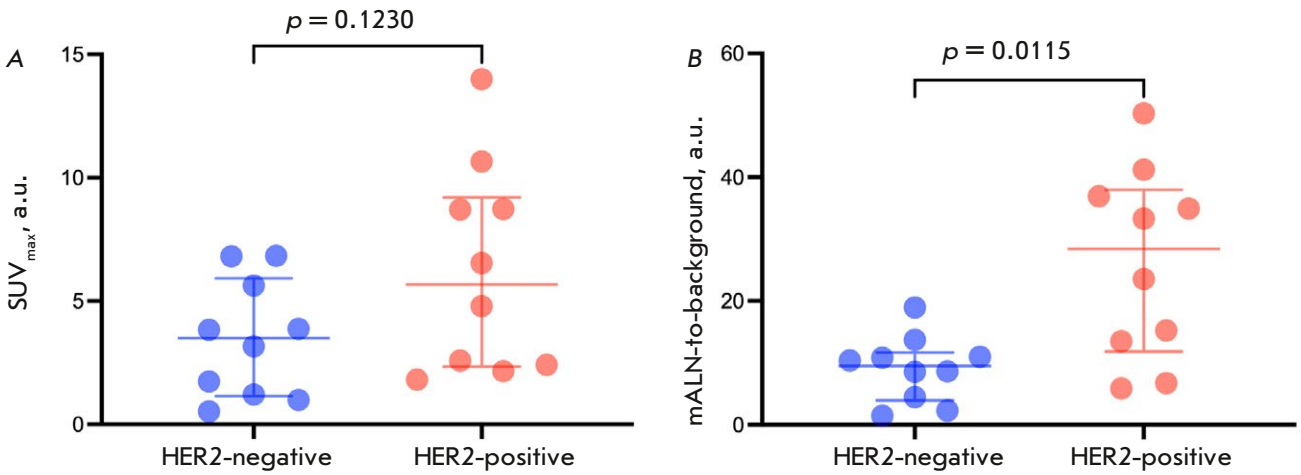

Fig. 3. SUV$_{max}$ (*A*) and mALN-to-background ratio (*B*) 4 h after administration of [^{99m}Tc]Tc-(HE)$_3$-G3 to BC patients with HER2-positive and HER2-negative mALNs

HER2-negative mALN status (9.0 ± 5.3) (p = 0.0115, Mann–Whitney test) (*Table 1*, *Fig. 3*).

[^{99m}Tc]Tc-(HE)$_3$-G3 uptake in reference organs and mALN-to-reference organ ratio

The SUV$_{max}$ of [^{99m}Tc]Tc-(HE)$_3$-G3 in the liver, LDM, and spleen was 5.4 ± 2.2, 0.4 ± 0.1, and 2.6 ± 1.4 and 7.6 ± 5.0, 0.5 ± 0.2, and 3.7 ± 2.6 for HER2-positive and HER2-negative mALNs, respectively. There were no statistical differences in the [^{99m}Tc]Tc-(HE)$_3$-G3 uptake in each organ for the positive and negative HER2/neu statuses (p > 0.05, Mann–Whitney test).

Calculations of mALN-to-reference organ ratios revealed that the mALN-to-LDM ratio was higher in HER2-positive mALNs than in HER2-negative mALNs (16.5 ± 8.3 and 8.9 ± 5.4, respectively) (p = 0.035, Mann–Whitney test) (*Table 1*, *Fig. 4*).

Determining the most informative parameter in assessing the HER2/neu status in mALNs of BC patients using [^{99m}Tc]Tc-(HE)$_3$-G3

The most informative parameter for assessing the HER2/neu status in mALNs using [^{99m}Tc]Tc-(HE)$_3$-G3 was determined by ROC analysis that identified the sensitivity and specificity parameters for each of them. The most sensitive and specific parameter for determining the HER2/neu status in the mALNs of BC patients using [^{99m}Tc]Tc-(HE)$_3$-G3

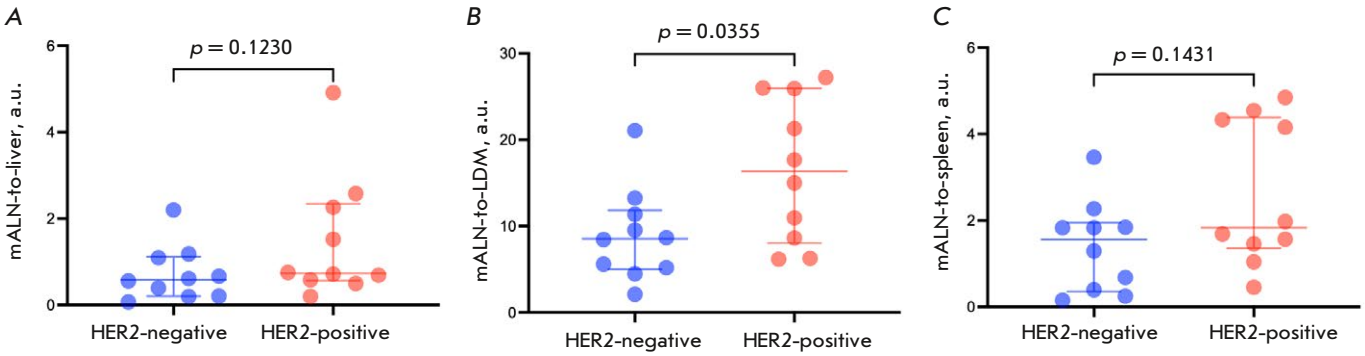

Fig. 4. mALN-to-liver (*A*), mALN-to-LDM (*B*), and mALN-to-spleen ratios (*C*) 4 h after administration of [^{99m}Tc]Tc-(HE)$_3$-G3

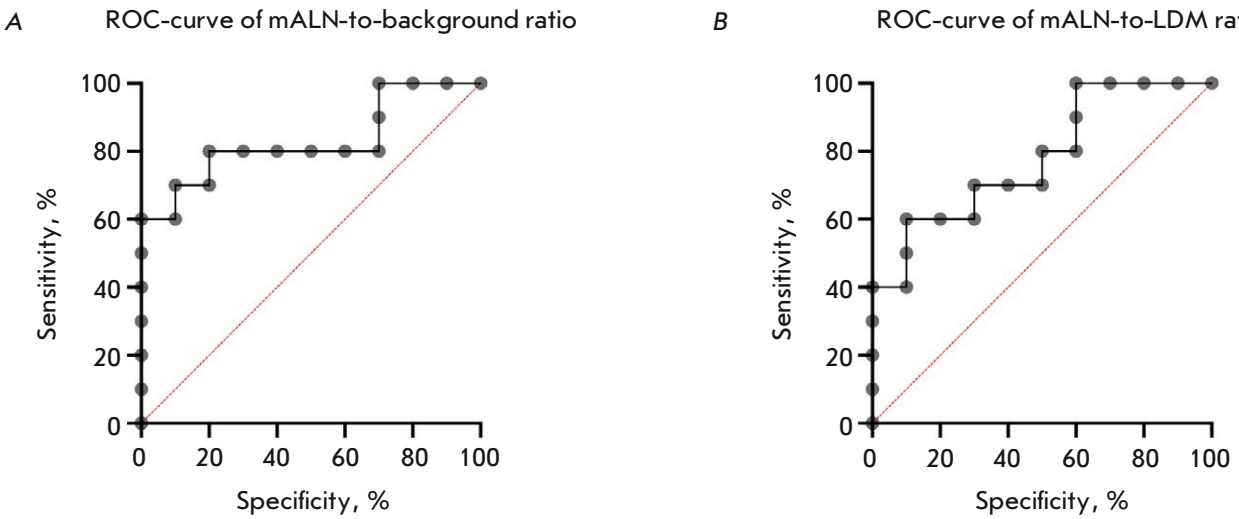

Fig. 5. ROC-curves of mALN-to-background (*A*) and mALN-to-LDM (*B*) ratios upon HER2/neu status detection in mALNs of BC patients 4 h after administration of [^{99m}Tc]Tc-(HE)$_3$-G3

was the mALN-to-background ratio: AUC of 0.83 (95% CI 0.63–1.00), sensitivity of 80%, and specificity of 80%; a threshold value of > 12.25 a.u. For the mALN-to-LDM ratio, these parameters were as follows: AUC of 0.78 (95% CI 0.58–1.00), sensitivity of 70%, and specificity of 70%; a threshold value of > 10.25 a.u. (*Fig. 5*).

DISCUSSION

The use of alternative scaffold proteins for radionuclidic receptor imaging of malignant tumors has been one of the promising developments in the field over the last 10 years. This is primarily due to the high specificity of the targeted delivery molecules and the shorter time interval between agent administration and the start of examination. Furthermore, the conduct of the diagnostic stage using modern devices that combine positron emission tomography and single-photon emission computed tomography with CT data provides a more accurate anatomical visualization and measurement of the administered agent's uptake *in vivo*.

Phase I clinical trials conducted at the Department of Radionuclide Therapy and Diagnostics of CRI TNRMC on HER2/neu in BC patients using a number of diagnostic radiopharmaceuticals ([^{99m}Tc]Tc-(HE)$_3$-G3, [^{99m}Tc]Tc-ADAPT6, and ^{99m}Tc-ZHER2:41071) [13, 14, 18] have demonstrated not only the safe character of the procedure, but also the possibility of typing primary breast tumors depending on their HER2/neu status ($p < 0.05$, Mann–Whitney test) [21]. These findings and expansion of

research towards locally advanced and metastatic BC forms promoted the planning and initiation of phase II clinical trials using [^{99m}Tc]Tc-ADAPT6 and [^{99m}Tc]Tc-(HE)$_3$-G3.

Previously published data on the use of the radiopharmaceutical [^{99m}Tc]Tc-ADAPT6 to determine the HER2/neu status in nALNs of BC patients demonstrated its high uptake (SUV_{max} = 8.7 ± 4.6) and a significant difference between HER2-positive and HER2-negative foci ($p < 0.05$, Mann–Whitney test). The ROC analysis revealed that using the threshold SUV_{max} value (4.22) in mALNs provides a 92% sensitivity level and 100% specificity [15].

In the present study, the highest statistical differences between HER2-positive and HER2-negative mALNs in BC patients 4 h after the administration of [^{99m}Tc]Tc-(HE)$_3$-G3 were observed for a mALN-to-background ratio of 26.1 ± 15.4 ($p = 0.0115$, Mann–Whitney test). According to the ROC analysis, the threshold value of the mALN-to-background ratio was 12.25, and sensitivity and specificity stood at an identical 80%.

These findings partially confirm previously reported data from preclinical and clinical trials of a comparative analysis of the diagnostic efficacy of [^{99m}Tc]Tc-ADAPT6 and [^{99m}Tc]Tc-(HE)$_3$-G3 [22]. For example, sequential administration of both diagnostic agents at an interval of 3 days before the start of systemic therapy in 11 HER2-positive BC patients demonstrated a higher uptake of [^{99m}Tc]Tc-ADAPT6 by primary breast tumors (SUV_{max} = 4.7 ± 2.1) 2 h after administration compared with that of [^{99m}Tc]Tc-(HE)$_3$-G3 (SUV_{max} = 3.5 ± 1.7) 4 h after administration ($p < 0.005$, paired *t*-test). In this case, the tumor-to-background ratio was not statistically different for both agents (15.2 ± 7.4 for [^{99m}Tc]Tc-ADAPT6 and 19.6 ± 12.4 for [^{99m}Tc]Tc-(HE)$_3$-G3) ($p > 0.05$, paired *t*-test) [23].

According to both studies, [^{99m}Tc]Tc-ADAPT6 proved to be the optimal agent for the typing of primary breast tumors, which provides the opportunity to differentiate the HER2/neu receptor status. This is important for optimizing the diagnostic stage and prescribing targeted therapy.

Given that, unlike the ADAPT6 protein, [^{99m}Tc]Tc-(HE)$_3$-G3 does not compete with trastuzumab because it binds to other HER2/neu epitopes, and the radiopharmaceutical may be useful in clinical practice to evaluate the monitoring of preoperative systemic therapy in patients with HER2/neu overexpression.

CONCLUSION

[^{99m}Tc]Tc-(HE)$_3$-G3 proved effective in differentiating the HER2/neu status in the mALNs of BC patients and demonstrated mALN-to-background ratios with 80% sensitivity and 80% specificity. To expand the indications for clinical use, [^{99m}Tc]Tc-(HE)$_3$-G3 should be further studied in the dynamics of preoperative systemic therapy in BC patients with HER2/neu overexpression. ●

This study was supported by a grant of the Ministry of Science and Higher Education of the Russian Federation No. 075-15-2024-536.

REFERENCES

1. Ge I., Erbes T., Juhasz-Böss I. // Gynecol Obstet Actions. 2022. V. 306. № 4. P. 943–957. doi: 10.1007/s00404-021-06352-9.
2. Chen H., Zhou J., Chen Q., Deng Y. // Medicine (Baltimore). 2021. V. 100. № 26. P. e26531. doi: 10.1097/MD.0000000000026531.
3. Sood R., Rositch A.F., Shakoor D., Ambinder E., Pool K., Pollak E., Mollura D., Mullen L., Harvey S. // Glob Oncol. 2019. V. 5. P. 1–17. doi: 10.1200/JGO.19.00127.
4. Han L., Li L., Wang N., Xiong Y., Li Y., Gu Y. // Interferon Cytokine Res. 2018. V. 38. № 12. P. 578–582. doi: 10.1089/jir.2018.0085.
5. Lower E.E., Khan S., Kennedy D., Baughman R.P. // Breast Cancer – Targets and Therapy. 2017. V. 9. P. 515–520. doi: 10.2147/BCTT.S137709.
6. Gebauer M., Skerra A. // Annu. Rev. Pharmacol. Toxicol. 2020. V. 60. P. 391–415. doi: 10.1146/annurev-pharmtox-010818-021118.
7. Tolmachev V., Orlova A., Sorensen J. // Semin. Cancer Biol. 2021. V. 72. P. 185–197. doi: 10.1016/j.semcancer.2020.10.005.
8. Bragina O.D., Deyev S.M., Chernov V.I., Tolmachev V.M. // Acta Naturae. 2022. V. 14. № 2. P. 4–15. doi: 10.32607/actanaturae.11611.
9. Pernas S., Tolaney S.M. // Ther. Adv. Med. Oncol. 2019. V. 11. P. 1758835919833519. doi: 10.1177/1758835919833519.
10. Tolmachev V.M., Chernov V.I., Deyev S.M. // Russ. Chem. Rev. 2022. V. 91. RCR5034. https://doi.org/10.1070/RCR5034.
11. Krasniqi A., D'Huyvetter M., Devoogdt N., Frejd F.Y., Sorensen J., Orlova A., Keyaerts M., Tolmachev V. // J. Nucl. Med. 2018. V. 59. P. 885–891. doi: 10.2967/jnumed.117.199901.
12. Eissler N., Altena R., Alhuseinalkhudhur A., Bragina O., Feldwisch J., Wuerth Q., Loftenius A., Brun N., Axelsson R., Tolmachev V., et al. // Biomedicines. 2024. V. 12. № 5. P. 1088. doi: 10.3390/biomedicines12051088.
13. Bragina O., von Witting E., Garousi J., Zeltchan R., Sandstrom M., Orlova A., Medvedeva A., Doroshenko A., Vorobyeva A., Lindbo S., et al. // J. Nucl. Med. 2021. V. 62. P. 493–499. doi: 10.2967/jnumed.120.248799.
14. Bragina O., Chernov V., Larkina M., Rybina A., Zelchan R., Garbukov E., Oroujeni M., Loftenius A., Orlova A.,

Sörensen J., et al. // Theranostics. 2023. V. 13. P. 4858–4871. doi: 10.7150/thno.86770.
15. Bragina O., Tashireva L., Loos D., Chernov V., Hober S., Tolmachev V. // Pharmaceutics. 2024. V. 16. № 4. P. 445. doi: 10.3390/pharmaceutics16040445.
16. Shilova O.N., Deyev S.M. // Acta Naturae. 2019. V. 11. № 4. P. 42–53. doi: 10.32607/20758251-2019-11-4-42-53.
17. Vorobyeva A., Schulga A., Konovalova E., Güler R., Löfblom J., Sandström M., Garousi J., Chernov V., Bragina O., Orlova A., et al. // Sci. Rep. 2019. V. 9. № 1. P. 9405. doi: 10.1038/s41598-019-45795-8.
18. Bragina O., Chernov V., Schulga A., Konovalova E., Garbukov E., Vorobyeva A., Orlova A., Tashireva L., Sorensen J., Zelchan R., et. al. // J. Nucl. Medicine. 2022. V. 63. № 4. P. 528–535. doi: https://doi.org/10.2967/jnumed.121.262542.
19. Wolff A.C., Hammond M.E.H., Allison K.H., Harvey B.E., Mangu P.B., Bartlett J.M., Bilous M., Ellis I.O., Fitzgibbons P., Hanna W., et al. // Pathol. Lab. Med. 2018. V. 42. P. 1364–1382. doi: 10.1200/JCO.2018.77.8738.
20. Wolff A.C., Somerfield M.R., Dowsett M., Hammond M.E.H., Hayes D.F., McShane L.M., Saphner T.J., Spears P.A., Allison K.H. // J. Clin. Oncol. 2023. V. 41. P. 3867–3872. doi: 10.1200/JCO.22.02864.
21. Bragina O.D., Chernov V.I., Garbukov E.Yu., Doroshenko A.V., Vorobyeva A.G., Orlova A.M., Tolmachev V.M. // Bull. Siberian Medicine. 2021. V. 20. № 1. P. 23–30. https://doi.org/10.20538/1682-0363-2021-1-23-30.
22. Tolmachev V., Bodenko V., Oroujeni M., Deyev S., Konovalova E., Shulga A., Lindbo S., Hober S., Orlova A., Vorobyeva A. // Int. J. Mol. Sci. 2022. V. 23. № 23. P. 15181. doi: 10.3390/ijms232315181.
23. Bragina O., Chernov V., Shulga A., Konovalova E., Hober S., Deyev S., Sorensen J., Tolmachev V. // Cancers. 2023. V. 15. P. 3149. doi: 10.3390/cancers15123149.

Experimental Use of Common Marmosets (*Callithrix jacchus*) in Preclinical Trials of Antiviral Vaccines

I. V. Gordeychuk[1,2*], O. S. Gancharova[1,3], S. A. Gulyaev[1], T. V. Gulyaeva[1], A. S. Zhitkevich[1], D. V. Avdoshina[1], A. V. Moroz[1], A. S. Lunin[1], S. E. Sotskova[1], E. A. Korduban[1], A. I. Tukhvatulin[4], E. O. Bayurova[1], A. A. Ishmukhametov[1,2]

[1]Chumakov Federal Scientific Center for Research and Development of Immune-and-Biological Products of Russian Academy of Sciences, Moscow, 108819 Russian Federation

[2]Institute for Translational Medicine and Biotechnology, Sechenov University, Moscow, 117418 Russian Federation

[3]Belozersky Institute of Physico-Chemical Biology, M.V. Lomonosov Moscow State University, Moscow, 119992 Russian Federation

[4]National Research Centre for Epidemiology and Microbiology named after Honorary Academician N.F. Gamaleya of the Ministry of Health of the Russian Federation, Moscow, 123098 Russin Federation

*E-mail: gordeychuk_iv@chumakovs.su

Received: January 21, 2024; in final form, April 4, 2024

DOI: 10.32607/actanaturae.27372

ABSTRACT **Common marmoset (*Callithrix jacchus*, CM) is a New World primate species that is of interest for preclinical trials of immunobiological products. In this study, we describe the approaches to long-term laboratory breeding and maintenance of CMs. We also establish the reference values of the main complete blood count and serum chemistry parameters evaluated during preclinical trials of immunobiological products and describe the histological characteristics of CM lymphoid organs during the development of post-vaccination immune response. We show that CMs bred in laboratory conditions excluding background infectious pathology are a relevant model that allows for a high degree of reliability in characterizing the safety and immunogenicity profile of antiviral vaccines during preclinical trials.**

KEYWORDS **laboratory primates, *Callithrix jacchus*, laboratory breeding of primates, antiviral vaccines, safety and immunogenicity of vaccines.**

INTRODUCTION

Nonhuman primates are the most suitable laboratory model for most human viral diseases. They allow for adequate reproduction of the stages of development of viral infections, including the route of transmission, the virus replication site, the pathogenesis features, and the development of all manner of immune response. Today, the late phases of preclinical trials that aim to assess the efficacy and safety of antiviral vaccines are mainly conducted using rhesus macaques (*Macaca mulatta*), crab-eating macaques (*M. fascicularis*), and green monkeys (*Chlorocebus sabaeus*). However, long-term maintenance of a significant number of large primates in experimental laboratories faces ethical restrictions and is extremely expensive, while primates kept in outdoor nurseries need to undergo long-term acclimatization and examination to exclude any background pathology before they can be used in experimental work. Furthermore, macaques have a much higher variability of major histocompatibility complex (MHC) class I genes compared to humans; so, in some cases the animals either need to be genotyped before inclusion in experiments or the number of animals per study group needs to be significantly increased, which further raises the cost of the trials [1].

Common marmosets (*Callithrix jacchus*, CM) are used in many areas of biomedical research, including reproductive biology, cognitive research, autoimmune and infectious diseases, oncology, and toxicology [2]. *C. jacchus* cells are also used in embryology and regenerative medicine [3].

A number of characteristics of CMs as a biological species make them a valuable laboratory model. These characteristics include: (1) phylogenetic proximity to humans; (2) small body weight (300–500 g);

and (3) the relative ease of laboratory breeding and maintenance [4]. An important feature of *C. jacchus* is the minimal diversity of both MHC class I and class II gene loci [5, 6], which contributes to highly reproducible study results.

CMs are susceptible to many viral, protozoan, and bacterial human pathogens [7], including the yellow fever virus, Epstein–Barr virus and other herpesviruses, hepatitis A virus, Junín virus, measles virus, hepatitis E virus, etc. Working with pathogens using CMs poses much fewer technical challenges, and is, therefore, associated with reduced risks for the personnel, than working with large primates. Furthermore, the genome of CMs has been fully sequenced; so, these primates can be adequately used in *in vivo* trials of novel gene therapy products, including experiments requiring transgenic animals [8, 9].

In combination with the recently elaborated procedures of assessment of the parameters of humoral and T cell-mediated immunity [10], the aforementioned factors make *C. jacchus* an optimal nonhuman primate species for the preclinical trials of safety, immunogenicity, and protectivity of antiviral vaccines. Nevertheless, broader experimental use of CMs requires solving a number of problems, including the development and standardization of laboratory husbandry protocols, as well as the functional and morphological characterization of the organs of their immune system.

In this study, we optimized the conditions of long-term laboratory breeding and maintenance of CMs, established the reference values of the main complete blood count (CBC) and serum chemistry parameters evaluated during preclinical trials of antiviral vaccines, and described the histological characteristics of the lymphoid organs of laboratory-bred CMs during the development of post-vaccination immune response.

METHODS

Ethics statement

The protocols of all the experiments involving primates described in this study were approved by the Ethics Committee of the Chumakov Federal Scientific Center for Research and Development of Immunobiological Products (protocols No. 110520-1 dated May 11, 2020, No. 140720-1 dated July 14, 2020, and No. 141021-2 dated October 14, 2021).

Laboratory breeding and maintenance of common marmosets

The animals were kept at the Laboratory of modeling of immunobiological processes with the experimental clinic of Callitrichidae of the Chumakov Federal Scientific Center for Research and Development of Immune-and-Biological Products of the Russian Academy of Sciences (Laboratory), in compliance with Sanitary Regulations 3.3686-21 "Sanitary and Epidemiological Requirements for Preventing Infectious Diseases," State Standard GOST 33218-2014 "Guidelines for Accommodation and Care of Laboratory Animals," and the Directive of the European Parliament and the Council of the European Union 2010/63/EC dated September 22, 2010.

The Laboratory facilities included the breeding zone and the experimental zone, with separated personnel and material flows. The automatic ventilation and air conditioning system ensured a year-round air temperature of 24–30°C and ⩾ 50% humidity; it contained two independent circuits for the breeding zone and the experimental zone.

The rooms of the breeding zone had windows for natural daylight, as well as daylight lamps that were switched on daily in the time interval between 7.00 a.m. and 5.00 p.m. all year round.

In the breeding zone, CMs were housed in family groups in enclosures sized 810 × 470 × 1760 mm (L × D × H). The family groups of CMs consisted of an adult animal pair and two generations of their offspring. The total number of animals per enclosure in the breeding zone ran up to six. At the age of 10–13 months, the offspring were placed into separate enclosures for immature animals. New family pairs were formed of primates aged at least 18 months; they were subsequently monitored to assess the individual compatibility of the new pair.

The daily energy value of the diet used in the Laboratory was 140 kcal per adult animal weighing 350–450 g; 18–24% of the diet consisted of protein from boiled chicken meat, baked cottage cheese, eggs, buckwheat and oatmeal porridge. The diet was daily supplemented with 360 IU of vitamin D_3, calcium gluconate, and a multivitamin complex.

Autoclavable dispensers (volume, 100 mL) of drinking water meeting the State Standard GOST R 51232-98 were mounted at the upper level of the walls of each enclosure.

Food leftovers were removed from the enclosure trays daily before morning feeding and after 12 p.m. The biological waste in the experimental zone was decontaminated by autoclaving.

Experimental manipulations with common marmosets

All the manipulations involving CMs were conducted by certified veterinarians or by researchers certified by the Federation of European Laboratory Animal

Science Associations (FELASA) and trained to work with nonhuman primates.

Experimental procedures were performed in a microbiological safety cabinet class II VIS-A-VIS, type A, installed in an operating room equipped to perform all the needed procedures with CMs, including biological material sampling, the administration of experimental preparations, and surgical interventions.

The animals were subjected to inhalational general anesthesia supplied via a full-face mask using the 410AP anesthesia machine (Univentor, Malta) with an air–gas mixture containing 4% isoflurane for anesthesia induction and 2–2.5% isoflurane for maintenance of anesthesia.

Subcutaneous radio chips of ISO 11784 standard (LifeChip, Destron Fearing, USA) in capsules made of biocompatible glass with an anti-migration coating were used for animal identification. The microchip is a passive device without a power source, so it can be used throughout the entire length of the life of an animal.

The body weight of the primates was measured using a Pioneer PA4102 electronic balance (Ohaus, USA).

All experimental manipulations with the primates were performed in the operating room, excluding any visual or auditory contact with other animals.

Complete blood count and serum chemistry

Whole blood samples for CBC and serum chemistry were collected by puncturing the femoral vein using 2.5 mL three-part syringes with 27G needles. The maximum blood volume sampled in a single procedure was under 3 mL ($\leqslant$ 8% of the circulating blood volume). For CBC, the syringes were prefilled with a Na-EDTA solution (final concentration, 5 mmol Na-EDTA per liter of blood). For the serum chemistry analysis, blood samples were collected into dry sterile test tubes and mixed and incubated at room temperature for 45 min; the serum was then separated by 10-min centrifugation (5810R, Eppendorf, Germany) at 600 g.

CBC with erythrocyte and leukocyte counts, as well as the leukocyte differential count, was carried out in a Goryaev chamber using Romanowsky staining.

The CM serum chemistry analysis was performed on a Cobas c111 automated analyzer (Roche, Switzerland) using the respective reagent kits. Values below the limit of detection of the instrument were counted as 0.

Histological analysis of post-vaccination changes in the lymphoid organs

Seven animals (three males and four females) aged 2–5 years, born in the Laboratory and included in preclinical trials of the inactivated whole-virion purified adsorbed vaccine against COVID-19 CoviVac, were used to study post-vaccination changes in the lymphoid organs of CMs [11].

On the day of the first immunization and 14 days later, 250 μL of the vaccine preparation (a suspension for intramuscular injection) were injected into the thigh muscles of the right and left legs of the animals in the experimental group (total injected volume, 500 μL per animal). The animals in the control group were injected with an identical volume of placebo containing the vaccine adjuvant (aluminum hydroxide) via the same route on the same days.

The animals were euthanized by anesthesia overdose (intramuscular injection of a threefold dose of a mixture of Xyla (De Adelaar, Netherlands) and Zoletil (Virbac, France) under isoflurane anesthesia.

Lymphoid organs (thymus, spleen, mesenteric lymph node, and inguinal lymph node draining the injection site) for histological examination were fixed immediately after necropsy by submersion in 10% buffered formalin (Biovitrum, Russia).

The organ samples were subjected to automated histological processing, which involved sequential dehydration in increasing concentrations of ethanol and xylene, embedding into Histomix paraffin medium (Biovitrum) on a Leica EG1150H paraffin embedding station (Leica, Germany), and microtomy of the resulting blocks with embedded samples on a Leica RM 2245 rotary microtome (Leica) to obtain 3 μm thick paraffin sections. The sections of lymphoid organs were mounted onto microscope slides, dried, deparaffinized, hydrated, stained with alum hematoxylin and water–alcohol eosin (Biovitrum), and placed under coverslips in a BioMount medium (Bio-Optica, Italy) to obtain stable histological specimens. One to four representative sections of proper quality were obtained per block.

The prepared sections were analyzed under a Zeiss Axio Observer A1 optical microscope (Carl Zeiss, Germany). Representative microimages were obtained using an AxioCam 305 high-resolution digital microscopy camera in the Zeiss Zen 2 lite blue edition software (Carl Zeiss). Microimage processing and panel compilation was performed using the AxioVision v.3.0 (Carl Zeiss) and GIMP (S. Kimball, P. Mattis, USA) software.

Statistical analysis

The age of the females at the time of first litter delivery, the survival rate of offspring during the neonatal period, and interdelivery intervals are presented as mean values and the standard deviation (SD). The statistical significance of differences in the parame-

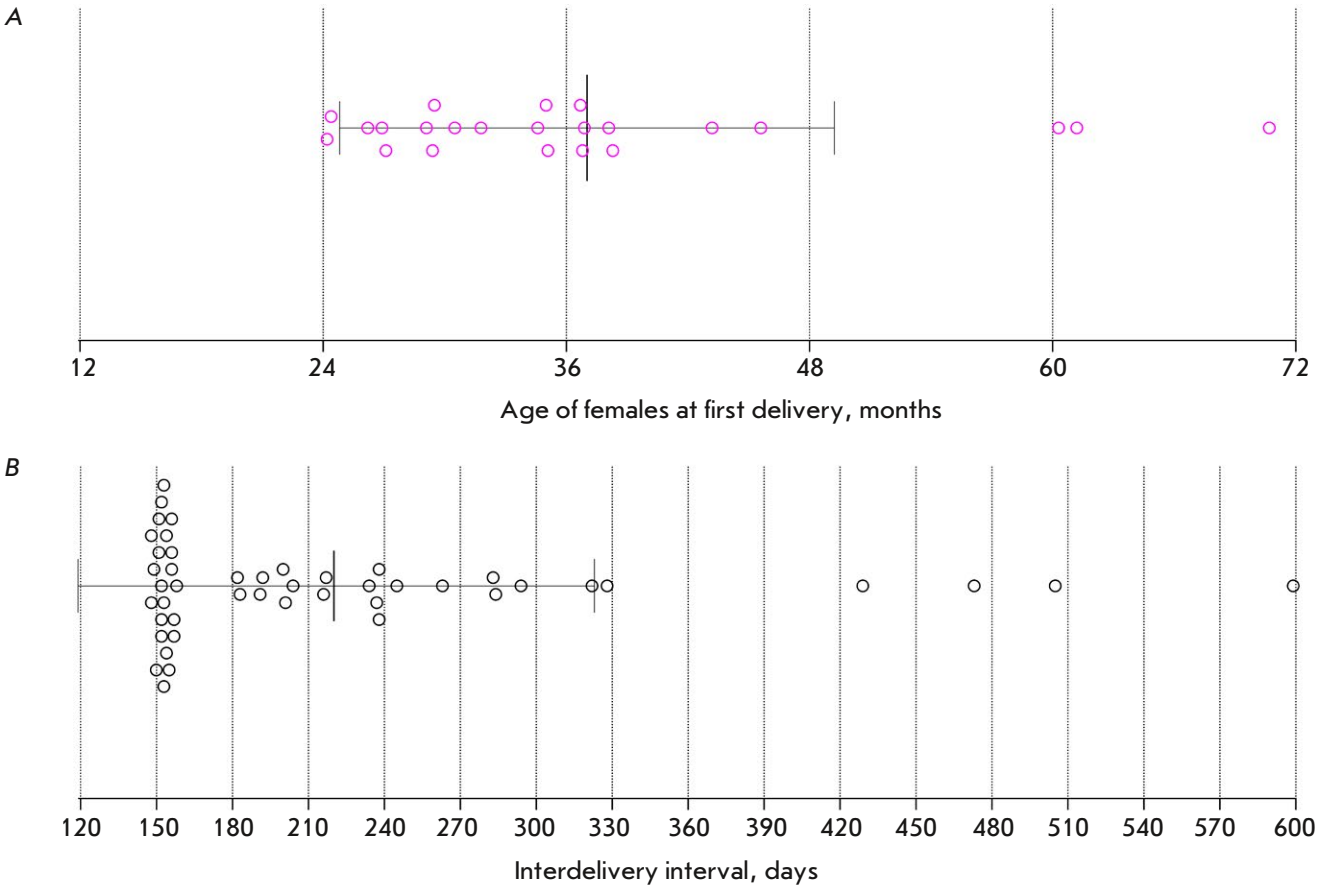

Fig. 1. Frequency of deliveries in female laboratory-bred common marmosets. (*A*) Pink circles indicate the age of females ($n = 23$) at the time of first delivery. (*B*) Black circles indicate interdelivery intervals ($n = 46$). Vertical solid lines indicate the mean value and standard deviation

ters of CBC and serum chemistry was assessed using the Mann–Whitney test in the GraphPad Prism 9 (9.3.0) software. Differences were considered significant at $p < 0.05$.

RESULTS

Laboratory breeding of common marmosets

The retrospective study was based on the data obtained by observing 23 female CMs born in the Laboratory, which delivered a total of 69 litters during the period between 2015 and 2023. *Figure 1* shows the estimated mean age of females at the first delivery, as well as the mean interdelivery interval.

The mean age of female CMs at the first delivery was 37 months (SD = 12.2); the minimal age was 24.2 months (*Fig. 1A*).

The mean interdelivery interval during the observation period was 220.1 days (SD = 102.9); 21 out of 46 litters were delivered 148–158 days after the previous delivery (*Fig. 1B*). Since the average gestation period in CMs is 143–144 days [4], the observed 148–158-day interdelivery interval meant that the next conception occurred within one or two weeks post-partum.

During the study period, a total of seven of the 23 observed females delivered one litter; four females delivered two litters; eight females, three litters; two females, four litters; one female delivered eight litters; and one female, 14 litters. All the newborn CMs that had survived the neonatal period were considered survivors, since no mortality was observed after 28 days of life. Gastrointestinal disorders during the first three days of life were the predominant cause of death. In the subsequent analysis, the infants that had died during the neonatal period were accounted as stillborn. Hence, the mean number of surviving offspring per delivery during the observation period

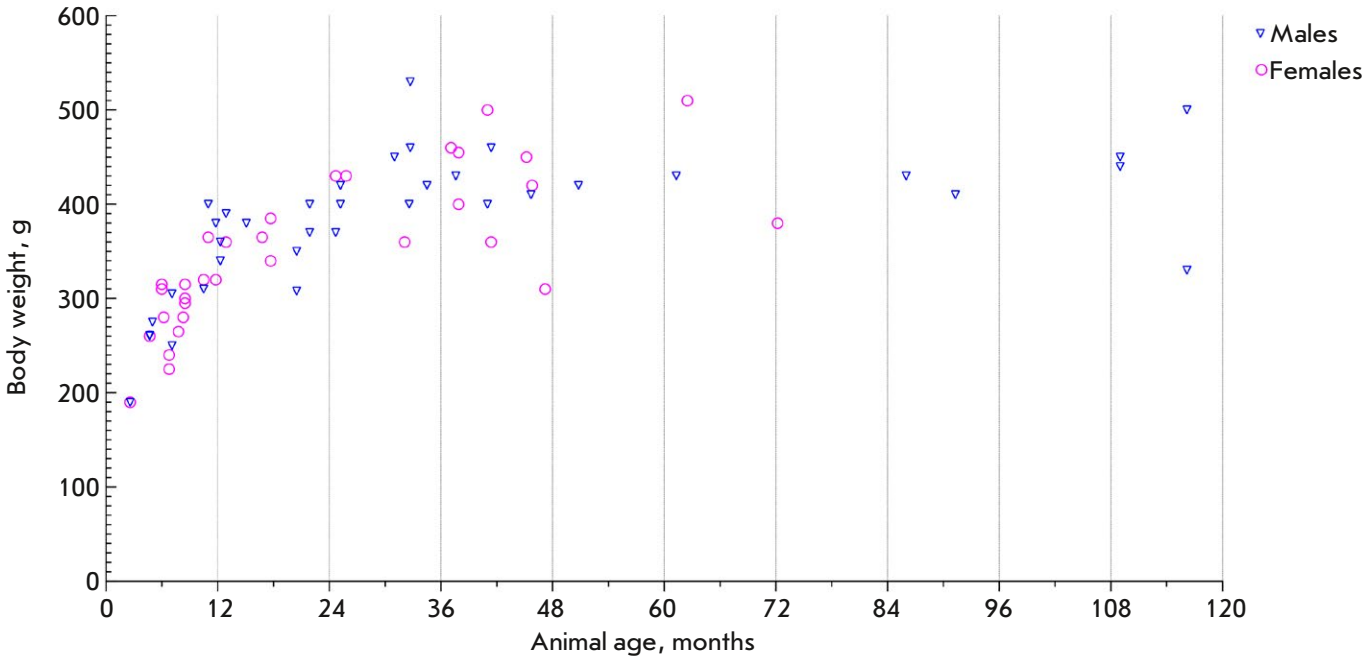

Fig. 2. Body weight and age of laboratory-bred common marmosets. The total number of animals is 69 (37 males and 32 females)

was 1.45, with significant variation between individual females.

Throughout the observation period, the most common delivery outcome (N = 69) in laboratory-bred CM females was giving birth to two infants (31/69). In 20/69 cases, there was one living newborn; and in 6/69 cases, three newborns. In 12 cases, CM females delivered one to five infants that were stillborn or died within the first three days of life.

According to our observations, there were no significant changes in female fertility until at least the eighth to ninth delivery, but this conclusion needs further verification, since only two females out of 23 delivered more than four litters during the observation period.

In April 2023, 69 laboratory-bred animals (37 males and 32 females aged from 2.6 months to 9.6 years) were weighed within a one-week period. The results are summarized in *Fig. 2*.

The body weight of CMs increased rapidly during their first 1.5 years of life. By the age of 18–20 months, the mean body weight of the animals had reached 400 g and stayed at the same level in all studied CMs aged up to 9.6 years. No significant differences in body weight were detected between the males and females (Mann–Whitney test, p = 0.0823).

Determining the reference values of the parameters of complete blood count and serum chemistry

In order to determine the reference values for CBC, blood samples were collected from a total of 38 CMs (26 males and 12 females) aged 2–5 years over the period from May 2020 to December 2021. The CBC results for laboratory-bred CMs are summarized in *Fig. 3*.

The mean erythrocyte count in the blood of laboratory-bred CMs was 6.6 (4.1–9.2) $\times 10^6$ cells/μl; the mean leukocyte count was 7.8 (3.9–15.3) $\times 10^3$ cells/μl. In the leukocyte differential, the mean percentage of lymphocytes was 32.8 (10–60)%; segmented neutrophils, 61.8 (37–89)%; band neutrophils, 0.8 (0–3)%; monocytes, 4.3 (1–8)%; basophils, 0.2 (0–1)%; and eosinophils, 0.1 (0–1)%. Females had a higher mean leukocyte count (Mann–Whitney test, p = 0.0047) compared to males. No statistically significant differences in other hematological parameters were detected between males and females.

In order to determine the reference values of the parameters of serum chemistry in laboratory-bred CMs, the creatinine level was measured in 20 animals (10 males and 10 females); the level of triglycerides, in 12 animals (five males and seven females); amylase activity, in eight animals (five males and

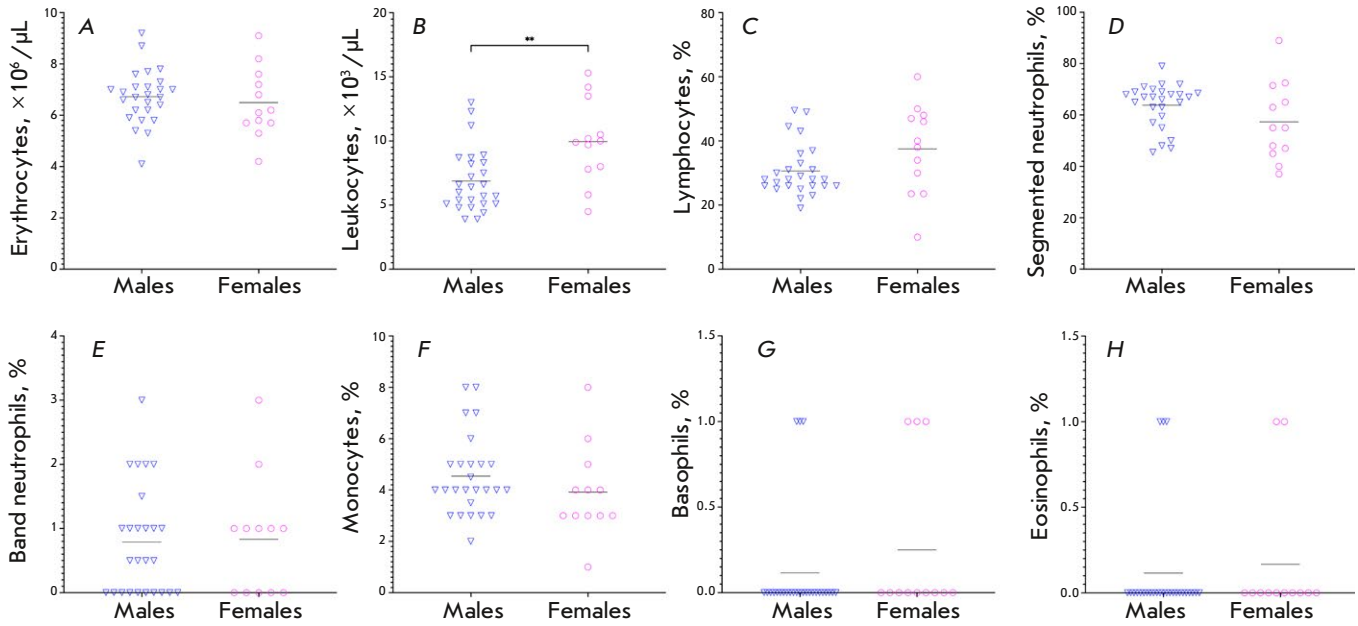

Fig. 3. Counts of (*A*) erythrocytes, (*B*) leukocytes, and the percentage of (*C*) lymphocytes, (*D*) segmented neutrophils, (*E*) band neutrophils, (*F*) monocytes, (*G*) basophils and (*H*) eosinophils in the leukocyte differential in the blood of laboratory-bred common marmosets ($N = 38$). Horizontal lines show the mean value. The statistical significance of the differences in the studied parameters between males and females was assessed using the Mann–Whitney test. **statistically significant differences ($p < 0.05$)

three females); C-reactive protein level, in 26 animals (21 males and five females); and other parameters were measured in 38 animals (26 males and 12 females). *Figure 4* shows the serum chemistry data for the laboratory-bred animals.

The mean serum level of total protein in laboratory-bred CMs was 71.3 (65–77.8) g/L; albumin level, 44.8 (38.7–53.58) g/L; ALT activity, 8.0 (2.4–24.3) U/L; AST activity, 182.8 (84.3–316.1) U/L; alkaline phosphatase activity, 106.5 (46.7–199) U/L; amylase activity, 885.7 (732.9–964) U/L; urea level, 4.8 (1.6–8.8) mmol/L; creatinine level, 51 (37.3–61.4) μmol/L; triglycerides level, 1.22 (0.48–2.17) mmol/L; total bilirubin level, 0.8 (0–2) μmol/L; direct bilirubin level, 0.4 (0–1.2) μmol/L; and C-reactive protein level, 2.3 (1.6–3.4) mg/L. No statistically significant differences in serum chemistry parameters were revealed between males and females (Mann–Whitney test, $p > 0.05$ for all the parameters).

Post-vaccination changes in the lymphoid organs of common marmosets

A histological analysis of the main lymphoid organs in four vaccinated (one male and three female) and three control (two male and one female) CMs aged 2–5 years was conducted during preclinical trials of the inactivated purified whole-virion adsorbed vaccine against COVID-19 CoviVac. We characterized the morphological structure of lymphoid organs in the animals that received a placebo and described the microstructural changes in the thymus, spleen, and lymph nodes observed during the development of the specific post-vaccination immune response.

The morphology of lymphoid organs in the control animals. The thymus (*Fig. 5A*) was preserved in all the animals. The lighter colored medullary and darker cortical substance of the organ were easily distinguishable morphologically. Accidental (stress-induced) involution of the cortical substance of the thymus, as well as lipomatosis of the cortical substance, was either absent or minimal. Histologically, the organ structure corresponded to what are normal observations for this species described in the literature [12] (including the presence of Hassall's corpuscles of the medulla).

The spleen (*Fig. 5C*) of the control primates had a proper white and red pulp structure: there were neither atrophic nor dystrophic changes, as well as no pathologic enlargement of the white pulp zones; red

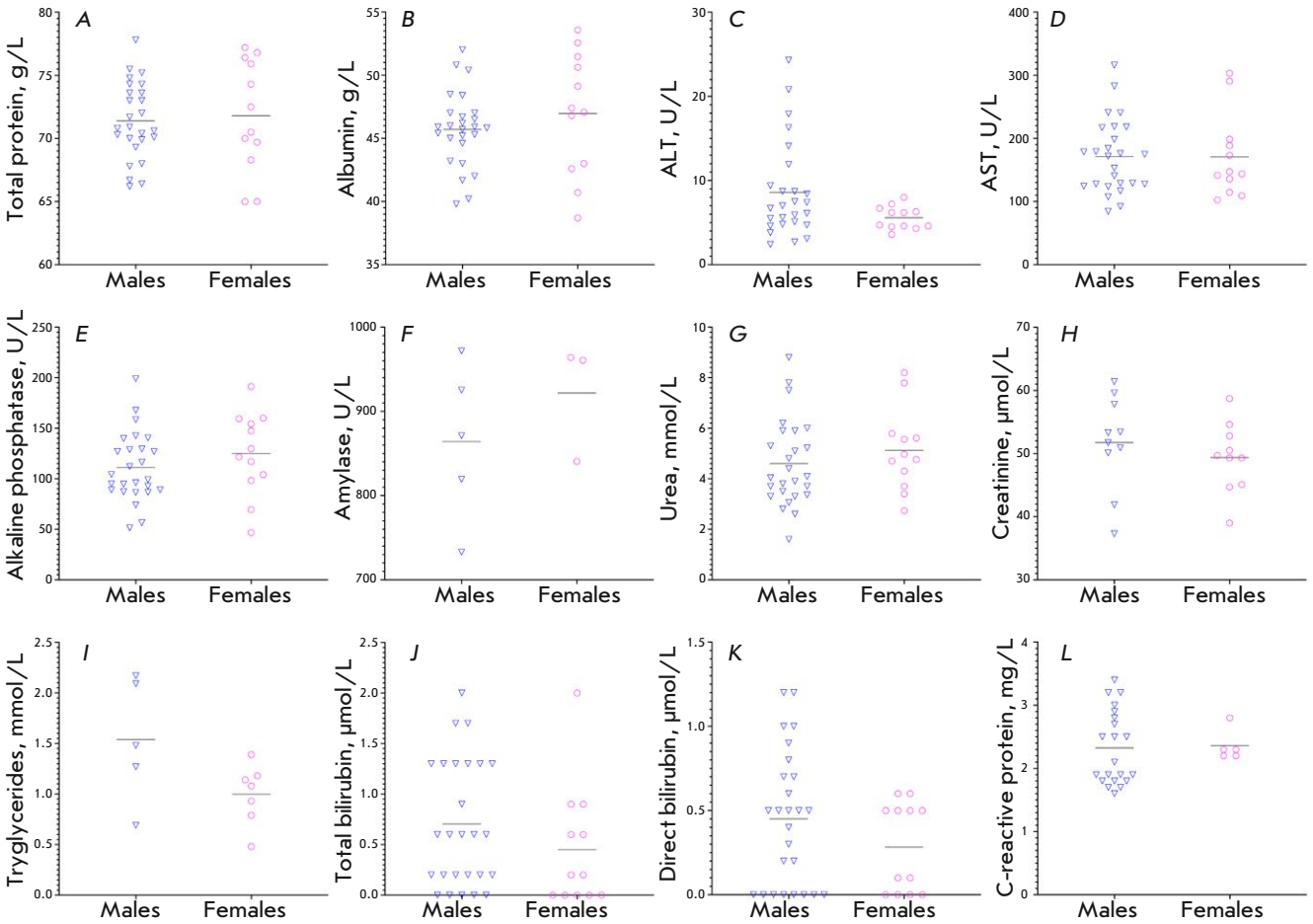

Fig. 4. Serum chemistry parameters in laboratory-bred common marmosets. (*A*) Total protein level; (*B*) albumin level; (*C*) ALT activity; (*D*) AST activity; (*E*) alkaline phosphatase activity; (*F*) amylase activity; (*G*) urea level; (*H*) creatinine level; (*I*) triglyceride level; (*J*) total bilirubin level; (*K*) direct bilirubin level; and (*L*) C-reactive protein level are presented. For creatinine, $N = 20$; for triglycerides, $N = 12$; for amylase, $N = 8$; for C-reactive protein, $N = 26$; and for other parameters, $N = 38$. Horizontal lines represent the mean value. The statistical significance of the differences in the studied parameters between males and females was assessed using the Mann–Whitney test

pulp was moderately congested. Spleen macrophages in the control animals were not vacuolated and did not show visible accumulation of the adjuvant components (aluminum hydroxide gel) or other substances. In all the animals studied, no morphological signs of myeloid metaplasia of red pulp were revealed.

In the control animals, the regional inguinal lymph node draining the placebo injection site (*Fig. 5E*) had a proper structure and consisted of the cortical plateau, the paracortical region with medullary cords, and the sinus system. In all the studied animals, the lymph node had no pathological changes and morphologically corresponded to the normal observations for the species.

The mesenteric lymph node (not shown) in both vaccinated and control animals had no distinctive features or pathological changes. Morphological manifestations of immunogenesis were observed: strongly marked germinal (light-colored) centers in the cortical plateau and minimal histiocytosis of the marginal sinus, which normally represents the function of the organ constantly undergoing antigenic stimulation from the intestine.

The morphology of the lymphoid organs of the vaccinated animals. No morphological differences were observed between the thymus of vaccinated animals (*Fig. 5B*) and those that had received the placebo.

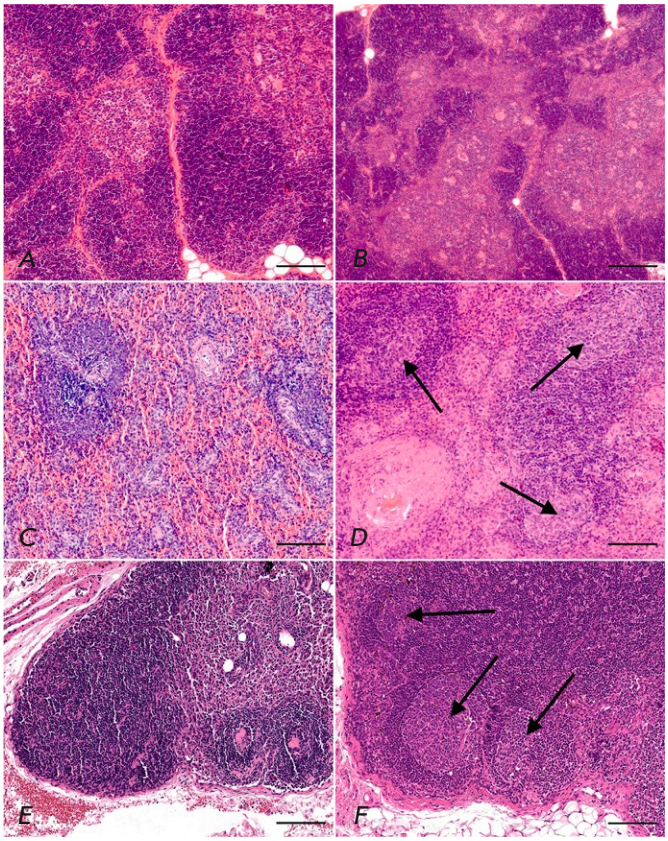

Fig. 5. Lymphoid organs of common marmosets immunized with a whole-virion inactivated vaccine CoviVac (*B*, *D*, and *E*) compared with the animals who received the placebo (*A*, *C*, and *E*). The morphology of the following lymphoid organs is presented: (*A*, *B*) – thymus; (*C*, *D*) – spleen; (*E*, *F*) – the regional (inguinal) lymph node. Arrows show the germinal centers in the cortical plateau of the lymph node and in the mantle zone of the white pulp of the spleen, the region of T-dependent B-immunogenesis. Hematoxylin and eosin, ×100 magnification. Scale bar, 200 μm

The thymus is a primary lymphoid organ where antigen-mediated B-immunogenesis does not elicit morphofunctional changes.

Formation of germinal (light-colored) centers in the mantle zone of the white pulp was detected in some spleen samples harvested from vaccinated CMs (*Fig. 5D*). This pattern morphologically indicates a T-dependent B-immunogenesis, corresponding to the development of a post-vaccination response. Otherwise, the spleen structure was identical to that in the control animals. We did not detect any vacuolization or visible accumulation of vaccine components, aluminum hydroxide gel, or other substances in the macrophages or within the marginal zone and the splenic red pulp of the vaccinated animals.

In vaccinated CMs, the regional inguinal lymph node draining the vaccine injection site (*Fig. 5F*) had a proper structure and consisted of the cortical plateau, the paracortical region with medullary cords, and the sinus system. Morphofunctional manifestations of immunogenesis of different intensities were observed: the emergence of germinal (light-colored) centers in the cortical plateau (the so-called B-dependent zone of the lymph node), as well as minimal histiocytosis of the marginal sinus, which corresponds to the development of a post-vaccination response and is morphologically similar to the events occurring in human lymph nodes upon antigen exposure.

DISCUSSION

Common marmoset *(C. jacchus*) is a nonhuman primate species endemic to the tropical Atlantic coastal zone in the northeastern regions of Brazil. In the wild, CMs live in families consisting of a stable pair of adult animals and their numerous offspring. In groups, one female is socially dominant, suppressing the reproductive activity of other females (in particular, mothers tend to dominate over daughters) [4]. CMs are diurnal and live in the dense upper and middle deciduous canopies, hiding from snakes and birds of prey.

The ethological needs of the species were taken into account for the development of techniques for the long-term laboratory maintenance of the CMs: the day/night light cycle in the animal breeding zone corresponds to daylight hours in the natural habitat; the structure of family groups matches that in the wild; and high enclosures allow the animals to move to the upper sections (i.e., to implement a behavioral cascade associated with searching for shelter when threatened). Changing of the arrangement of environmental enrichment elements inside the enclosures was performed by a veterinarian, in accordance with a cyclical scheme. Environmental enrichment elements (bells, mirrors, branches, hangers, swings, hammocks, and bars) aimed to extend the spectrum of behaviors and motion patterns and make foraging activity more challenging (feeders with drilled holes arranged in different areas within the enclosures). Primates get used to the unchanging environmental enrichment elements and lose interest within 3–5 days, which may subsequently cause stereotypy or elevated aggression within the group.

In this study, we determined the mean age of the females at the first litter delivery, the mean interdelivery interval, the survival rate of infants, and the kinetics of body weight gain in laboratory-bred

CMs. Altogether, these findings allow one to manage the colony population depending on the experimental needs. According to our data, a CM female on average gives birth to about three babies per year and the population of laboratory-bred CM colonies can be increased by both maximizing the number of pairs and choosing the most fertile females.

Safety assessment of immunobiological products using laboratory-bred CMs requires the identification of the reference values of the parameters of CBC and serum chemistry, since the published reference values are often based on results obtained by studying the biomaterial collected from a small number of animals housed in outdoor enclosures in nurseries and zoos. An analysis of the samples collected from 38 healthy male and female CMs aged 2–5 years revealed the main parameters of CBC and serum chemistry. Statistically significant differences between males and females were observed only for the leukocyte count (Mann–Whitney test, $p = 0.0047$).

During the preclinical assessment of vaccine safety and immunogenicity, it is important to characterize the immunization-induced histological changes in the lymphoid organs. In this study, we performed a histological analysis of the lymphoid organs of CMs after the administration of an inactivated whole-virion adsorbed vaccine against COVID-19 and in the placebo-treated group.

The histological examination revealed Hassall's corpuscles (clusters of concentric eosinophilic terminally differentiated epithelial cells) in the thymic medulla of the CMs, which makes their thymus morphologically similar to the human thymus. It is known that in rodents, which are most frequently used in preclinical trials of immunobiological products, including vaccines, the thymic structure differs from that of humans and their thymic medulla contains no Hassall's corpuscles [13].

Another important histologic finding was that the studied primates had no myeloid metaplasia of the splenic red pulp when the morphological signs of hematopoietic tissue occurred outside the bone marrow. Like in humans, myeloid metaplasia in CMs is regarded as a background pathological condition associated with bleeding [14]: so it is easier to classify changes in the spleen of CMs and extrapolate them to humans, as compared to the data obtained when working with rodent spleen.

Therefore, in this study, we have garnered evidence that there is high similarity between the structure of the lymphoid organs of CMs and humans both in the control animals and during the development of a post-vaccination immune response.

Our findings suggest that CMs bred under isolated laboratory conditions preventing any background infectious pathology are an adequate laboratory model for characterizing the safety and immunogenicity profiles of antiviral vaccines in preclinical trials with a high level of confidence.

CONCLUSIONS

Owing to a number of biological features particular to the species, as well as the development of procedures of breeding, long-term maintenance, and experimental management, laboratory-bred CMs have recently been used in a number of biomedical studies, including preclinical trials of inactivated [11, 15] and adenoviral vector-based [10] vaccines against COVID-19, an adenoviral vector-based vaccine against Middle East respiratory syndrome-related coronavirus [16], and a candidate recombinant vaccine against hepatitis E [17]. ●

This study was supported by the Chumakov Federal Scientific Center for Research and Development of Immunobiological Products.

REFERENCES

1. Heijmans C.M.C., de Groot N.G., Bontrop R.E. // Int. J. Immunogenet. 2020. V. 47. № 3. P. 243–260.
2. 't Hart B.A., Abbott D.H., Nakamura K., Fuchs E. // Drug Discov. Today. 2012. V. 17. № 21–22. P. 1160–1165.
3. Bayurova E., Zhitkevich A., Avdoshina D., Kupriyanova N., Kolyako Y., Kostyushev D., Gordeychuk I. // Cells. 2023. V. 12. № 16. P. 2020.
4. Tardif S.D., Smucny D.A., Abbott D.H., Mansfield K., Schultz-Darken N., Yamamoto M.E. // Comparative Medicine. 2003. V. 53. № 4. P. 364–368.
5. Antunes S.G., de Groot N.G., Brok H., Doxiadis G., Menezes A.A., Otting N., Bontrop R.E. // Proc. Natl. Acad. Sci. USA. 1998. V. 95. № 20. P. 11745–11750.
6. Cao Y.H., Fan J.W., Li A.X., Liu H.F., Li L.R., Zhang C.L., Zeng L., Sun Z.Z. // Am. J. Primatol. 2015. V. 77. № 5. P. 527–534.
7. Carrion R., Patterson J.L. // Curr. Opin. Virol. 2012. V. 2. № 3. P. 357–362.
8. Marmoset Genome Sequencing and Analysis Consortium // Nat. Genet. 2014. V. 46. № 8. P. 850–857.
9. Sasaki E., Suemizu H., Shimada A., Hanazawa K., Oiwa R., Kamioka M., Tomioka I., Sotomaru Y., Hirakawa R., Eto T., et al. // Nature. 2009. V. 459. № 7246. P. 523–527.
10. Tukhvatulin A.I., Gordeychuk I.V., Dolzhikova I.V., Dzharullaeva A.S., Krasina M.E., Bayurova E.O., Grousova D.M., Kovyrshina A.V., Kondrashova A.S., Avdoshina D.V., et al. // Emerg. Microbes Infect. 2022. V. 11. № 1. P. 2229–2247.
11. Kozlovskaya L.I., Piniaeva A.N., Ignatyev G.M., Gordey-

chuk I.V., Volok V.P., Rogova Y.V., Shishova A.A., Kovpak A.A., Ivin Y.Y., Antonova L.P., et al. // Emerg. Microbes Infect. 2021. V. 10. № 1. P. 1790–1806.
12. Kaspareit J., Friderichs-Gromoll S., Buse E., Habermann G. // Exp. Toxicol. Pathol. 2006. V. 57. № 5–6. P. 405–410.
13. Pearse G. // Toxicol. Pathol. 2006. V. 34. № 5. P. 504–514.
14. David J.M., Dick E.J., Hubbard G.B. // J. Med. Primatol. 2009. V. 38. № 5. P. 347–359.
15. Gordeychuk I.V., Kozlovskaya L.I., Siniugina A.A., Yagovkina N.V., Kuzubov V.I., Zakharov K.A., Volok V.P., Dodina M.S., Gmyl L.V., Korotina N.A., et al. // Viruses. 2023. V. 15. № 9. P. 1828.
16. Dolzhikova I.V., Grousova D.M., Zubkova O.V., Tukhvatulin A.I., Kovyrshina A.V., Lubenets N.L., Ozharovskaia T.A., Popova O., Esmagambetov I.B., Shcheblyakov D.V., et al. // Acta Naturae. 2020. V. 12. № 3. P. 114–123.
17. Gordeychuk I., Kyuregyan K., Kondrashova A., Bayurova E., Gulyaev S., Gulyaeva T., Potemkin I., Karlsen A., Isaeva O., Belyakova A., et al. // Vaccine. 2022. V. 40. № 1. P. 89–99.

Dihydroquercetin-Loaded Liposomes Change Fibrous Tissue Distribution in the Bleomycin-Induced Fibrosis Model

E. V. Ivanov[1*], M. R. Akhmetshina[1], A. R. Gizatulina[1], M. V. Gulyaev[1], O. S. Pavlova[1,2], Y. A. Pirogov[2], S. A. Gavrilova[1]

[1]Faculty of Medicine, Lomonosov Moscow State University, Moscow, 119991 Russian Federation
[2]Faculty of Physics, Lomonosov Moscow State University, Moscow, 119991 Russian Federation
*E-mail: ivanovev102@yandex.ru

Received: May 31, 2024; in final form, June 24, 2024
DOI: 10.32607/actanaturae.27440

ABSTRACT **The effects of the antioxidant dihydroquercetin (DHQ) were studied in a model of pulmonary fibrosis. DHQ penetration into the lesion was facilitated by encapsulation into liposomes. Pulmonary fibrosis was modeled in rats by intratracheal injection of bleomycin. For the first 7 days, the rats in the treatment group received a liposomal emulsion with DHQ, while in the comparator group rats received saline. In the control group, intact rats did not receive any exposure. Thirty days after the initiation, lung function and the pathological lesion volume were assessed by 7T 1H MRI and the lungs were taken for histologic examination. The proportion of fibrous tissue was counted by Masson's trichrome staining. Both experimental groups were characterized by a significant functional pulmonary deficiency, with low mortality and a small lesion area. In the rats treated with DHQ, the distribution of fibrous tissue was significantly altered. Significantly more fibrous tissue was found in the center of the lesion, while significantly less was in the interstitial space of alveoli. Lung density at the same time was lower in the treated lungs. Dihydroquercetin encapsulated in liposomes affects the mechanisms of bleomycin-induced pulmonary fibrosis progression in rats. While accelerated fibrosis of the lesion can restrict inflammatory processes, delayed fibrosis of the interstitium can further improve the functional state of the lungs.**

KEYWORDS **dihydroquercetin, bleomycin, liposomes, antioxidants, pulmonary fibrosis, 1H MRI.**

ABBREVIATIONS **ROS – reactive oxygen species; DHQ – dihydroquercetin; IS – impulse sequence; MRI – magnetic resonance imaging; FID – free induction decay; FoV – field of view; HSV – hue, saturation, value; TE – time to echo; TR – repetition time; UTE – ultrashort echo time.**

INTRODUCTION

Pulmonary fibrosis poses a significant healthcare threat, even more so now after the COVID-19 pandemic. Numerous studies have demonstrated that serious COVID-19 cases lead to pulmonary fibrosis [1]. Severe coronaviral fibrosis causes persistent respiratory insufficiency and long-term impairment. Fibrotic lesions could occur after severe pneumonia caused by other pathogens, most often viruses [2, 3]. The most severe interstitial lung disease, idiopathic pulmonary fibrosis (IPF), can be treated by numerous anti-inflammatory and antiproliferative drugs such as glucocorticoids, azathioprine, cyclophosphamide, mycophenolate mofetil, and some novel antifibrotic agents like nintedanib and pirfenidone [4, 5]. While the latter agents have shown themselves to increase progression-free survival for three to five years and reduce annual mortality, they are still insufficient when it comes to preventing IPF progression in the course of a lifetime.

Pulmonary alveoli consist of a thin alveolocyte layer vulnerable to different cellular damage sources. During the infectious process, leukocytes secrete numerous substances damaging bacteria, infected, and healthy cells. Among other sources of damage there are reactive oxygen species (ROS) produced by neutrophils and macrophages. Aside from the direct cellular damage caused by lipid peroxidation and DNA oxidation, ROS can damage the surfactant layer and basal membranes, thus subsequently im-

pairing lung repair [1, 2]. Antioxidant administration is favorable in terms of simplicity, safety, and availability. Multiple studies have been conducted to test antioxidant effectiveness in preventing, treating, or slowing pulmonary fibrosis progression. Although most antioxidant agents have failed to show a significant impact in preclinical and clinical trials, it remains unclear why they do not work as expected. The reasons include lack of potency, unfavorable pathway of administration and delivery, as well as unwanted disruption of ROS-related regulatory pathways [3, 4]. There are multiple mechanisms via which antioxidants can prove beneficial in lung fibrosis. Antioxidant resveratrol alleviates fibrosis in rodents by Smad and Smad7 expression inhibition, reduces lung fibroblasts proliferation and differentiation, and reduces collagen deposition [5].

One of the most promising antioxidants is quercetin and its derivatives such as dihydroquercetin (DHQ). In several experimental studies, quercetin has shown an ability to attenuate lung fibrosis [6, 7]. Yuan et al. demonstrated that DHQ markedly attenuates a SiO_2-induced lung inflammation and fibrosis in mice [8]. Impellizzeri et al. found similar effects of quercetin in the bleomycin-induced fibrosis model [9]. One of the major limitations in using quercetin or DHQ alone in the treatment of pulmonary fibrosis is a delivery problem, since the substance is poorly soluble. Targeted delivery of antioxidants is also important as they could be consumed by various other tissues. A delivery system could be used to overcome those issues. Liposomes were found to passively target inflammatory sites, since they are characterized by a leaky vasculature [10]. Liposomes have been evaluated as a delivery platform to treat pulmonary fibrosis with different loaded drugs *in vivo*. Liu et al. have shown successful delivery of Nrf2 blockers in ROS-sensitive liposomes through inhalation [11]. Li et al. reported the effectiveness of neutral liposomes loaded with antifibrotic drugs through inhalation in an established pulmonary fibrosis model [12]. Other researchers have used loaded liposomes to target pulmonary fibrosis through systemic parenteral infusions with RNA-based agents [13]. While the oral route of delivery has not been studied as extensively for liposome-carried antifibrotics, it remains valid, since many studies have shown that liposomes could be taken into the lymphatic system from the small intestine [14–17].

In this study, we chose dihydroquercetin stabilized in liposomes (Flamena emulsion, research company 'Flamena', Russia) as an intervention means to prevent pulmonary fibrosis progression in bleomycin-induced pulmonary fibrosis in rats, since this formulation has previously shown promising results in other pathologies thanks to its anti-inflammatory and antioxidant properties [18–21].

EXPERIMENTAL

Animal Handling

The authors followed the European Convention for the Protection of Vertebrate Animals used for Experimental and other Scientific Purposes and local rules for conducting scientific research with laboratory animals. The experiment was approved by the local bioethics committee at its meeting held on February 9, 2023, Protocol No. 2. Male Wistar rats with a body weight ranging from 200 to 250 g were procured from a conventional breeding facility in the Institute of Medical and Biological Problems (Moscow, Russia). A total of 30 rats were enrolled, 10 in each group. The experiment was launched after an initial 2-week period of acclimatization and handling. Throughout the experiment, the animals were housed in a certified vivarium with a 12-hour day/night cycle and were provided with ad libitum access to standard chow and water. Upon arrival, the animals were separated into groups based on their body weight and placed in standard T3 cages.

Fibrosis model

Thirty animals were distributed into three groups, ten animals per group: Flamena, Saline, and Intact. The rats in the Intact group were not subjected to any interventions throughout the study as a healthy control group. In the two experimental (fibrosis) groups, the animals received an intratracheal bleomycin injection (7.5 mg/kg) under isoflurane anesthesia; dosage and route of administration were chosen according to those used in refs. [22, 23]. The bleomycin solution was administered by injection to ensure accurate administration and dosage, as well as uniform delivery of the substance to the lungs. The skin of anesthetized rats was disinfected, and a short incision was made over the cricoid cartilage of the larynx. The soft tissues were separated with tweezers in such a way as not to cause bleeding and not to affect the thyroid gland. After visualization of the larynx and trachea, the head end of the manipulation table was raised. The required amount of the drug was administered slowly using a syringe. The dose and route of administration were selected according to the literature. After insertion, the tissue was sutured with atraumatic suture material and the skin was treated with an antiseptic. A 30-day period was deemed long enough to ensure that a pathological lesion of sufficient size will form and be small enough to avoid possible spontaneous healing in the long term.

Treatment

Twenty-four hours after bleomycin administration, we started treatment with equal amounts of liposome-encapsulated dihydroquercetin (Flamena emulsion) or sterile saline. According to license documents and published information, Flamena is a phospholipid emulsion which contains 30 mg/mL lecithin, 35 mg/mL glycine, and 4 mg/mL dihydroquercetin [20]. At least one membrane phospholipid is vortexed with water and ethanol to obtain a liposomal phase containing active ingredients (Patent RU 2369383, October 30, 2007). A combined route of administration was chosen to achieve greater exposure. Previously, we had found Flamena to be effective in a rat myocardial infarction model after oral administration [19]. Since other liposomal carriers had been reported to be effective in lung fibrosis as described in the Introduction section, we chose to apply both approaches because specific portions of damaged lungs could fail to receive the drug through a single route of administration. The published and digital data indicate that Flamena is safe at various doses and routes of administration [21]. A prewarmed to room temperature emulsion (25 mg/kg or 6.25 mL/kg) was administered per os through a gastral tube. The animals were then subjected to 15-min drug inhalation in a 20 L chamber through an ultrasound inhaler (approximately 5 mL of the drug was evaporated per three animals). Double drug administration was continued for 5 days.

Endpoint

The mortality rate was assessed until the endpoint. Weight was measured prior to the final procedures. MRI was performed on day 30 under isoflurane anesthesia to assess the lesion size. Under deep over-anesthesia, the rib cage was opened; the heart and lung vessels were perfused with a 1% neutral buffered formalin solution until heart arrest. Lungs were excised and washed in a buffer solution, then they were weighed with a 10 mg precision scale (Sartorius). The lungs were filled with the 1% neutral buffered formalin solution through the trachea and sliced for further histological processing through the basal and upper lobes. Slices with pathological lesions no thicker than 6 mm were immersed in a 4% neutral buffered formalin solution for 36 h.

MRI

The study was performed on a 7T MR scanner (BioSpec 70/30 USR; Bruker BioSpin, Ettlingen, Germany) operated with a ParaVision® v.5.1 console and equipped with a 105 mT/m gradient amplitude device. Lung images were recorded using a Birdcage volume radiofrequency coil with an inner diameter of 72 mm. Anesthesia was induced with 4% isoflurane in a chamber, followed by maintenance at 1.5% via a nose mask in 95% O_2 at a flow rate of 1 L/min. Isoflurane was administered using a vaporizer (Ugo Basile, Italy), while oxygen was supplied by a JAY-10 oxygen concentrator (Longfian Scitech Co. LTD, China).

Lung MR images were acquired using a 3D ultrashort echo time (UTE) pulse sequence with radial k-space filling [24]. The scan parameters were set as follows: scanning area 7 × 7 × 7 cm^3, scanning matrix 152 × 152 × 152, frequency bandwidth 100 kHz, TE = 18 μs; TR = 8 ms; flip angle = 6°; number of averages = 1; radial projections = 72,231; and polar undersampling = 1. The total acquisition time was 9 min and 38 s.

Post-processing of the MRI data

Radial pulse sequences, such as UTE, are less affected by motion artifacts, allowing for lung imaging without the requirement of breath synchronization. As a result, the lung MR images are averaged over the respiratory cycle. Furthermore, it is possible to retrospectively gate the raw data and generate two images corresponding to the inspiration and expiration respiratory phases. This additional insight enhances the diagnostic capabilities of MRI for evaluating lung conditions and respiratory disorders.

The pulmonary MRI data were processed following the methodology outlined in ref. [25]. The center of the radial k-space is oversampled, and the magnitude of the first point of each collected projection (FID, free induction decay) is modulated by the respiratory process. Consequently, the first points of each projection reflect the respiratory phase. These data can be sorted to produce two new k-spaces with incomplete filling derived from the original k-space: one representing the inspiration phase, and the other one, the expiration phase. The final step involves reconstructing gated data using the iterative sampling density compensation function, followed by resampling onto a Cartesian grid before the fast Fourier transform.

The retrospective gating method was implemented using Python 3.8 and Matlab 2019b (MathWorks, USA), resulting in two sets of MR images corresponding to the inspiration and expiration phases. Since the inspiration phase occurs faster than the expiration phase, 8–10% of the projections correspond to inspiration, while 55–60% correspond to expiration. Consequently, the image quality (signal-to-noise ratio, sharpness, and resolution) of the expiration phase is noticeably higher. Based on this, we used the expira-

tion images to delineate lung masks during exhalation and pathology masks, while the inspiration images were utilized solely for lung masks during inhalation. The lung and pathology masks were manually segmented using the ImageJ software (v.1.51j8, NIH, Bethesda, MD, USA) [26] with the freehand selection tool. From the resulting binary masks, the volumes of inspiration (V_{insp}), expiration (V_{exp}), and pathology (V_{pat}) were calculated by summing the non-zero pixels and multiplying by the voxel resolution. Additionally, the respiratory volume ($V_{resp} = V_{insp} - V_{exp}$), respiratory ratio ($V_{resp}/V_{exp}$), and pathology percentage volume (V_{pat}/V_{exp}) were calculated. The expiratory volume to lung weight ratio, V_{exp}/m, mL/g, was calculated to approximate lung density.

Histological processing and staining

Afterwards, fixation tissues were rinsed with tap water for 2 h and dehydrated with ascending isopropanol solutions, mineral oil, and liquid paraffine. Standard paraffine blocks were embedded and left to rest for at least 24 h. Paraffin-embedded blocks were sliced to 5 μm thick slices on a ThermoFisher S355 rotary microtome. Standard hematoxylin and eosin staining (Leica, USA) was performed for general tissue integrity evaluation. Fibrous tissue collagen distribution was revealed with Masson's trichrome staining (Biovitrum, Russia).

Slides were analyzed and digitalized using a Zeiss Axio A2 microscope and the Zeiss Zen software. Images were further processed with the ImageJ software. A 27-point scale was developed to analyze the degree of pathological involvement. Nine parameters were assessed with a 4-point scale, from score 0 (normal tissue) to score 3 (unfunctional tissue, total inflammation, abundant fibrosis) in each field of view (FoV): presence of alveoli, alveolar integrity, bronchial integrity, inflammation severity, type of infiltration, necrosis in FoV, presence of fibrous tissue, interstitial fibrosis, and focal fibrosis. Ten random FoVs per slide with ×200 magnification were averaged.

Masson's stained slides were pictured in three areas: pathological lesion, the nearest alveoli-containing region, and the distant alveoli-containing region. Five FoVs were picked for each area with a ×200 magnification. Blue/red segmentation was performed based on the HSV color scale. Total blue and red areas, and the blue-to-red ratio, were calculated.

Statistical analysis

All data processing and analysis were conducted using the Python 3.8 programming language and open-source code libraries. Statistical analyses were performed using the Statsmodels and Scipy libraries. Due to the small sample sizes, non-parametric statistical tests and universal statistical models were employed. The Statsmodels library's mixed-effects generalized linear model (GLM) was used to analyze time-dependent changes. The Kruskal–Wallis test was employed for dependent variables, followed by post-hoc multiple comparisons using the Dwass-Steel-Critchlow-Fligner (DSCF) test. Screening correlation analyses were conducted using simple Spearman R calculations. All p-values less than 0.05 were considered statistically significant. Data visualization was conducted using boxplots, depicting medians, quartiles, and the minimum/maximum values, with the Matplotlib and Seaborn libraries.

RESULTS

Mortality and weight gain

Throughout the experiment, the mortality rate reached 20% (N = 2) in the Saline group, of which one rat died after final anesthesia application. In the Flamena group, the mortality rate was 10% (N = 1): no significant difference was found with the chi-squared test. Since the mortality rate was low, we did not perform a survival analysis of death risk factors.

Weight gain in both groups was significantly reduced compared to that in intact rats. Through the 30 days of the experiment, Intact rats gained 23.93% (IQR 20.42, 28.33) off the baseline weight, while Saline group rats gained 14.65% (IQR -8.55, 22.08, $p = 0.047$), and Flamena group rats gained 11.58% (IQR -1.21, 17.07, $p = 0.01$). The two fibrosis groups did not show significant differences in weight gain ($p = 0.86$).

Lung weight

Lungs were weighed gross after the excision. Total lung weight in the fibrosis groups was 1.5 times higher compared to that in intact rats. In the Saline group, it reached 3.76 g (IQR 2.84, 4.22, $p = 0.001$ vs. the Intact group, *Fig. 2A*); in the Flamena group, it reached 3.77 g (IQR 3.39, 3.83, $p < 0.001$ vs. the Intact group). In the Intact group, the median lung weight was 2.43 g (IQR 2.33, 2.60). Weight values did not differ between the two fibrosis groups ($p = 0.796$).

MRI results

The results of MRI data processing for one of the rats are shown in *Fig. 1*.

Two groups did not show statistically significant differences in both the absolute pathological lesion volume (0.38 mL (IQR 0.18, 0.61): in the Saline group, 0.45 mL (IQR 0.25, 0.67), in the Flamena group,

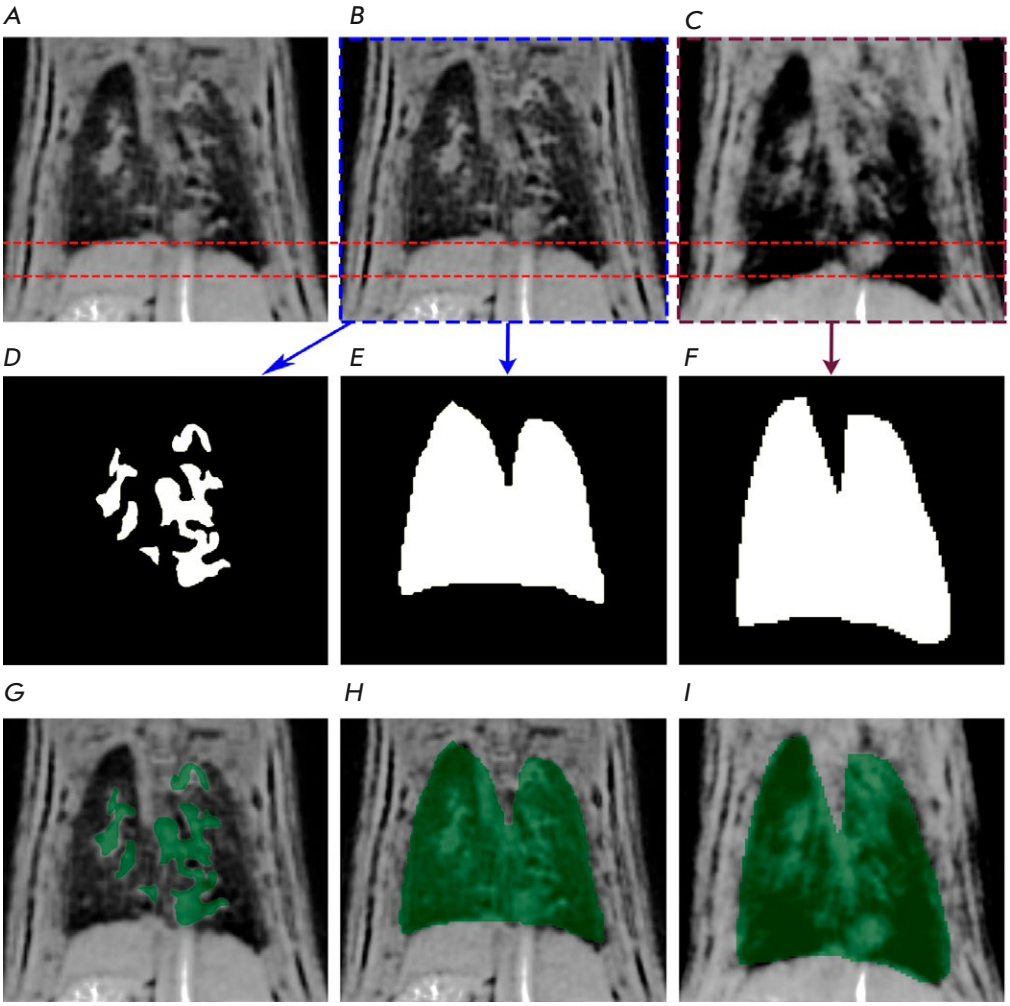

Fig. 1. Pulmonary MR images of a randomly selected rat from the Saline group along with the corresponding lung and pathology masks. The data are presented only for one slice.
(*A*) – initial MR image of the lungs;
(*B*) – image of the expiration phase;
(*C*) – image of the inspiration phase;
(*D*) – pathology mask;
(*E*) – expiration mask;
(*F*) – inspiration mask;
(*G*) – pathology mask overlaid on the initial MR image of the lungs;
(*H*) – expiration mask overlaid on the image of the expiration phase;
(*I*) – inspiration mask overlaid on the image of the inspiration phase

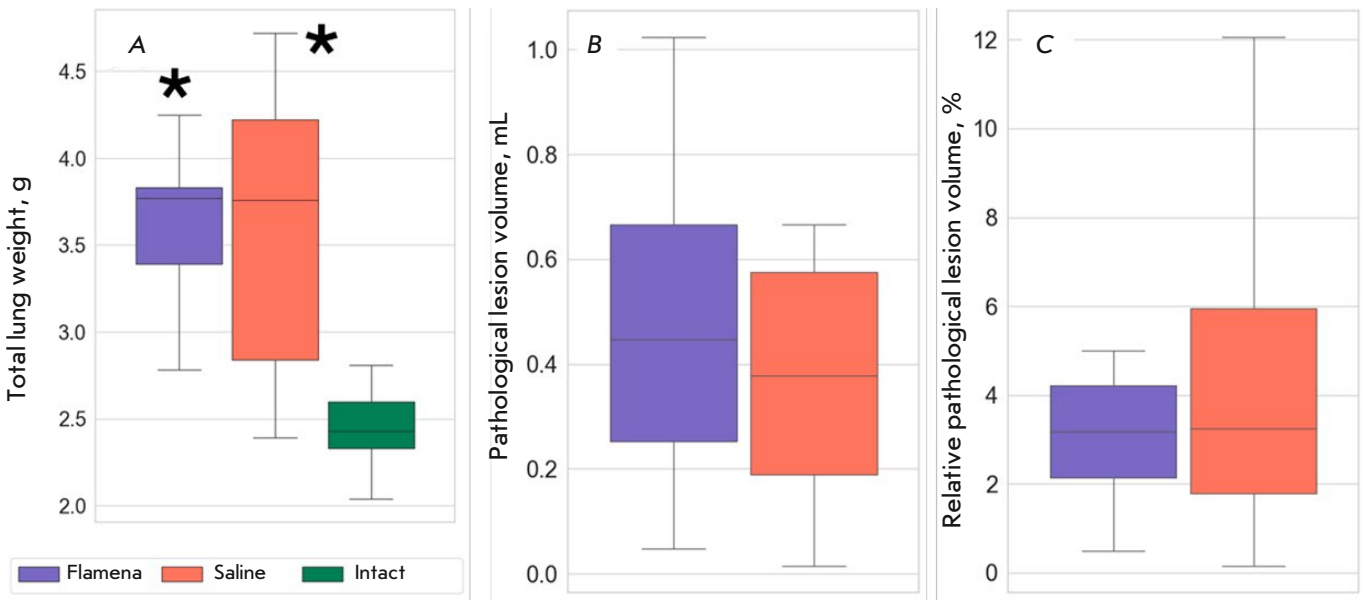

Fig. 2. Structural changes in bleomycin-induced fibrosis. (*A*) – Total lung weight, g; (*B*) – absolute pathological lesion volume, ml; (*C*) – relative pathological lesion volume, %. $^{*}p < 0.05$ compared to the Intact group

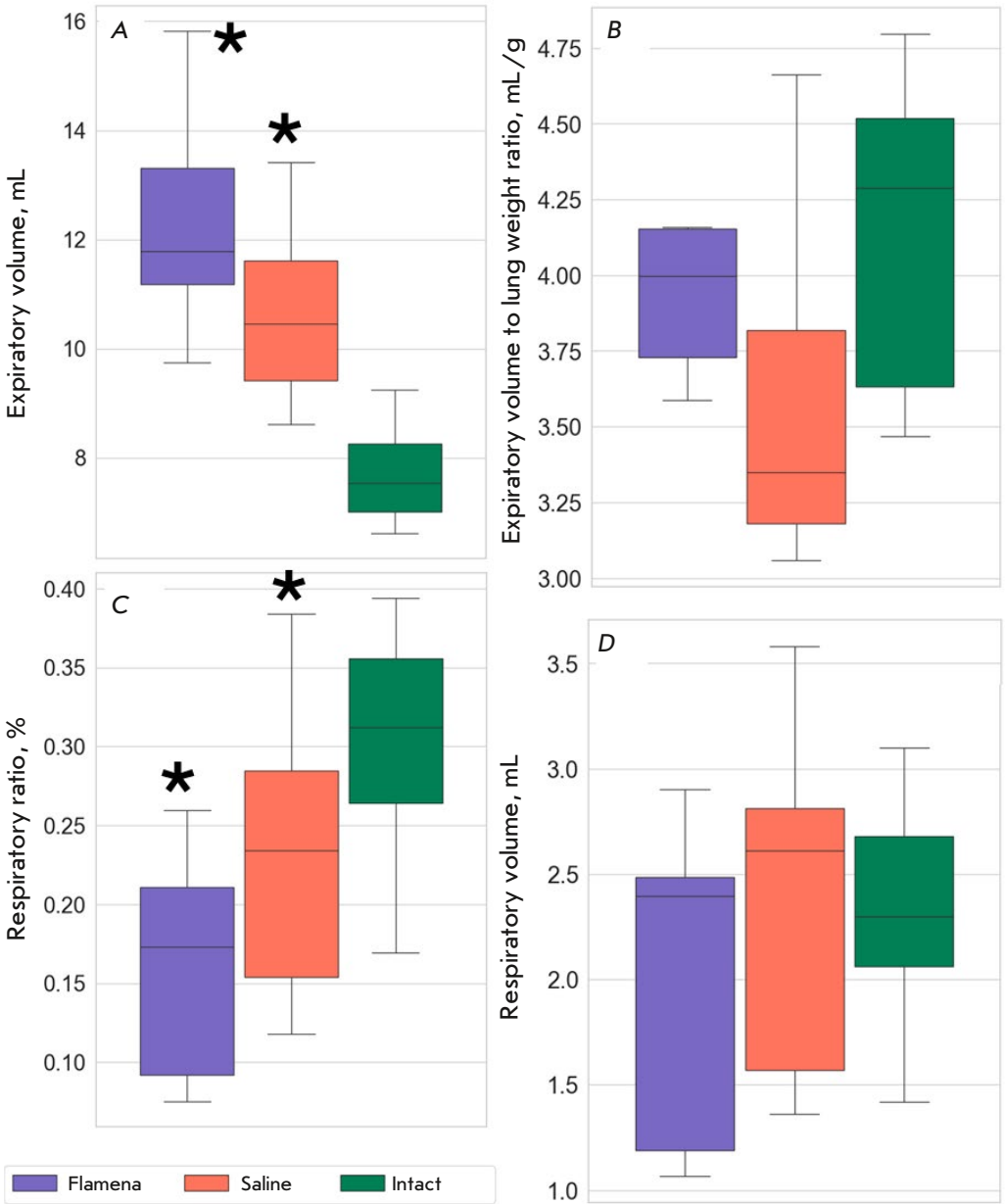

Fig. 3. Functional lung changes in bleomycin-induced fibrosis.
(*A*) – Expiratory volume, mL;
(*B*) – expiratory volume to lung weight ratio, mL/g;
(*C*) – respiratory ratio, %;
(*D*) – respiratory volume, mL.
*$p < 0.05$ compared to the Intact group

p = 0.606), and the relative lesion volume (3.24% (IQR 1.77, 6.04) in the Saline group, 3.18% (IQR 2.14, 4.22), p = 0.96, *Figs. 2B* and *2C*).

The expiratory (V_{exp}) and inspiratory volumes (V_{insp}) were higher in the fibrosis groups compared to the Intact group (*Table 1*). While the respiratory ratio (V_{resp}/V_{exp}) was significantly lower in the fibrosis groups compared to the Intact group, the respiratory volume (V_{resp}) did not differ, probably because of the uncontrolled breath ratio during MRI scanning, which led to a large spread of this value (*Fig. 3*). Among all the characteristics, the expiratory volume (V_{exp}) was the most distinct in the Flamena and Saline groups, with p = 0.074 (*Fig. 3A*). Since the lung weight was much higher in the fibrosis groups, we also calculated the expiratory volume (V_{exp}) to lung weight ratio, which was used as a surrogate for a lung density measurement (*Fig. 3B*). While in the Saline group lungs had less volume per unit of weight compared to Intact rats (p = 0.027), indicating higher density, no

Table 1. Functional parameters of the lungs for the various groups of animals used in the experiment

Group animals	V_{exp}, mL		V_{insp}, mL		V_{resp}/V_{exp}, arb. units		V_{resp}/V_{exp}, %	
	ME	IQR	ME	IQR	ME	IQR	ME	IQR
Intact	9.76	9.49–10.20	7.54	7.04–8.16	0.31*	0.27–0.35*	-	-
Saline	13.02	11.58–14.49	10.45	9.39–11.75	0.23*	0.15–0.29*	3.61	1.77–6.04
Flamena®	14.27	13.59–15.75	11.78	11.18–13.31	0.17*	0.09–0.21*	3.52	2.11–4.61

Note. ME – median values, IQR – interquartile range. *$p < 0.05$.

statistically significant differences were found in the Flamena and Intact groups ($p = 0.387$). The median values in the two fibrosis groups almost reached significant differences, with $p = 0.059$.

Lung histology

Histology analysis was performed with slices obtained from the lobe base, where larger lesions were found. H&E-stained slices were evaluated semi-numerically using a 27-point scale. While the analysis was performed with averaged random field of views, the overall score did not differ in the two groups, with a median of 12.80 points (IQR 9.36, 14.88) in the Saline group and a median of 11.50 points (IQR 10.17, 13.50, $p = 0.918$) in the Flamena group (*Fig. 4A*).

Masson's staining revealed that collagen bundles were distributed differently in the Flamena and Saline groups. Fibrosis inside the pathological lesion represented a finished inflammatory phase, and in the Flamena group, intense collagen staining was observed. Despite the same lesion size, in most slides in the Saline group, lesion did not show collagen deposition as much, with more necrosis, inflammation, and even Masson-negative fibers. The blue/red ratio in the pathological lesion was 0.61 (IQR 0.35, 0.92) in the Flamena group and 0.16 (IQR 0.07, 0.23) in the Saline group ($p = 0.006$, *Fig. 4B*). In the most affected lung tissue, the blue/red ratio was significantly higher in the Saline group, with 0.21 (IQR 0.12, 0.62) vs. 0.72 (IQR 0.64, 0.92), $p = 0.01$. In the most intact lung tissue, more intense interstitial collagen staining also was revealed in the Saline group, with a ratio of 0.71 (IQR 0.42, 0.85) vs. 0.19 (IQR 0.16, 0.34), $p = 0.01$. Intact tissue collagen staining was comparable with that in the Flamena group (0.17 (IQR 0.12, 0.2), $p = 0.27$), Interstitial fibrous tissue deposition was usually present along with interstitial space thickening and intense inflammation (*Fig. 5*).

DISCUSSION

Antioxidant treatment for pulmonary fibrosis has been evaluated in many studies with encouraging, but still not definitive, results. In our study, we evaluated dihydroquercetin stabilized in liposomes in the rat bleomycin-induced fibrosis model. The latter is one of the best studied and widely used experimental models of pulmonary fibrosis; therefore, its features are well-known. Liposomal carriage improves both DHQ stability and potency; hence, we expected to find prominent treatment effects. Liposomes also ensure selectivity towards inflammatory sites [10]. The administration regimen was semi-arbitrary; higher cumulative dosage or extended period of treatment potentially could lead to better results. Since Flamena has previously been found to be effective in the rat myocardial ischemia/reperfusion model, we expected increased exposure through the combined regimen [19]. We chose to treat rats 24 h after the bleomycin injection, emulating preventive antifibrotic treatment in a severe pulmonary infection like COVID-19.

In our study, the overall mortality rate was low and any survival statistical changes were not possible. We used 7T MRI as one of the best options to study the lesion size and lung excursion. Pathological lesions in most cases did not occupy large parts of their lungs. Hence, it was hard for any type of intervention to reveal drastic results. However, as the lung weight and its density changed, there was a significant degree

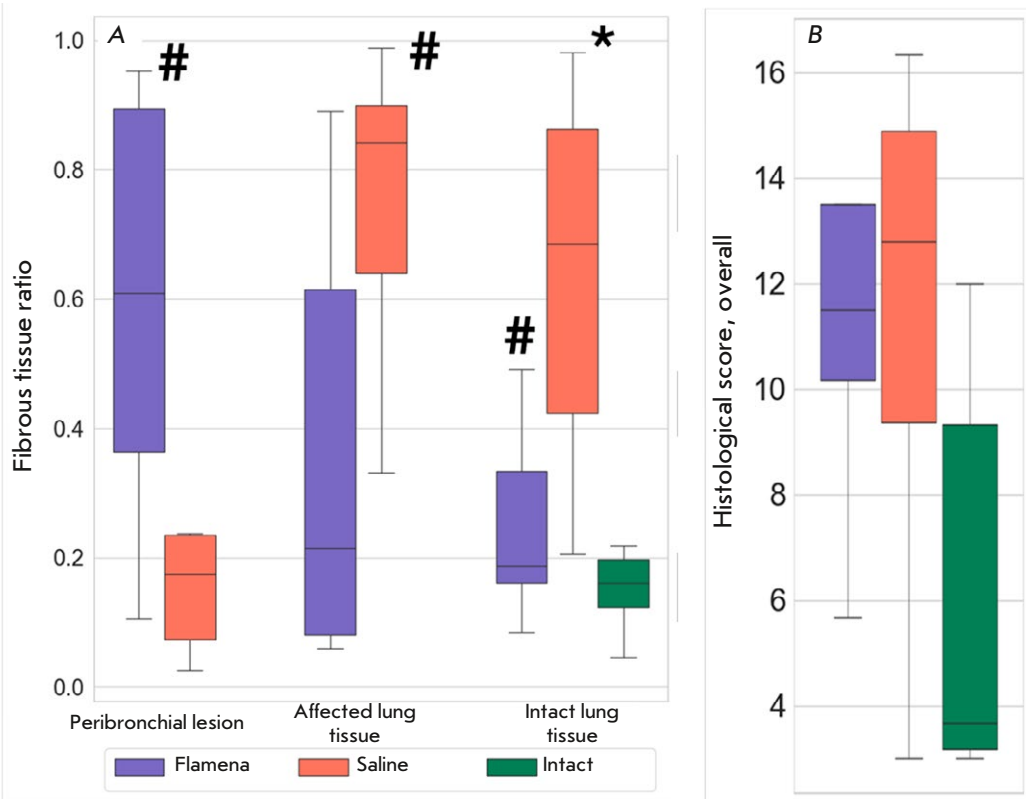

Fig. 4. Assessment of histological integrity. (*A*) – The total histological integrity score; (*B*) – blue-to-red pixel area ratio. $^{*}p < 0.05$ compared to the Intact group, $^{\#}p < 0.05$ compared to the Saline group

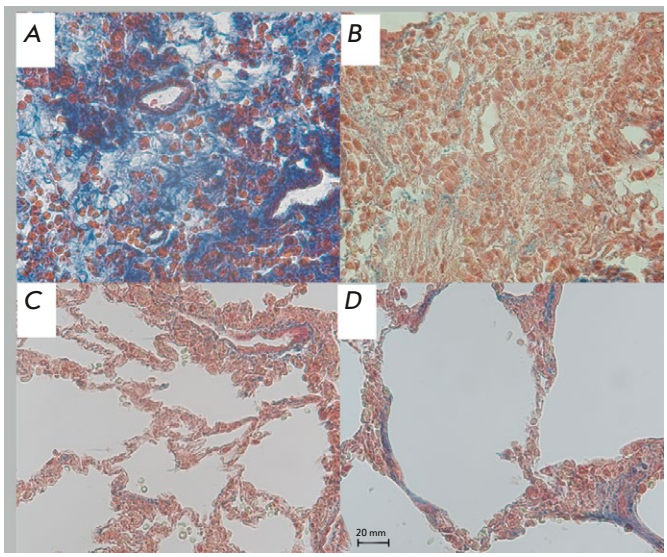

Fig. 5. Lung histology revealing collagen deposition patterns. (*A*) – Pathological lesion, the Flamena group; (*B*) – pathological lesion, the Saline group; (*C*) – distant lung tissue, the Flamena group; (*D*) – distant lung tissue, the Saline group. Masson's trichrome staining, ×200 magnification

of pulmonary disfunction. Rats treated with Flamena tended to have less dense lungs, which is an important sign of a less severe inflammation and fibrosis.

There are many varieties of bleomycin-induced fibrosis models, and they are accompanied by various degrees of pathological involvement. Single-dose intratracheal administration usually leads to comparable results. Over one month, no mortality at all or a low mortality rate is usually observed in male rats [27]. While most of the studies provide no quantitative lesion volume measurements, those that do report about 3% of fibrous tissue prevalence, same as in our study [28, 29]. Histological changes in the lung tissues identified by us were similar to those reported in the literature: widespread inflammatory infiltration, necrotic foci, and bundles of collagen fibers. Alveoli near pathological lesions had thicker walls and were usually fused and dysfunctional with damaged walls [30, 31]. According to the literature [22, 27], pulmonary fibrosis in the bleomycin model becomes significant as early as two weeks after the initiation and persists for several months. While fibrosis could be reversed 3 to 6 months after the injection in rodents, it became full blown one month after the injection [32–35].

In our study, the use of Flamena significantly changed the distribution of fibrous tissue. Interstitial fibrosis is a serious complication that can lead to further decline in lung function, and its signs were less noticeable in the treated group. On the contrary, an increase in the amount of fibrous tissue within the pathological focus is a positive sign, since it indicates a more rapid resolution of inflammatory reactions. Quercetin is a drug that eliminates the signs of aging. It interacts with aging cells, enhances their apoptosis, and reduces the fibrogenic potential. DHQ in its stabilized form is a more powerful antioxidant, and we expected it to be at least as effective as quercetin. DHQ was found to be effective in various diseases but has not been studied as extensively in bleomycin fibrosis. We have shown that DHQ, when delivered in liposomes, can alter the mechanisms of development of bleomycin fibrosis. Although this did not cause significant changes in lung function, differences may be emerge over longer periods.

CONCLUSIONS

Our study has shown that stabilized DHQ can significantly modify fibrosis and alter its features. Fibrosis within the pathological focus is necessary to prevent the spread of infection and inflammation. Faster remodeling of the lesion may be beneficial and limit excessive inflammation. Progression of interstitial fibrosis in the functional alveoli can lead to severe respiratory impairment.

In a first, we studied the effects of stabilized dihydroquercetin in liposomes on bleomycin-induced pulmonary fibrosis and found that it limited interstitial fibrosis. Further studies with longer duration and different bleomycin administration protocols are needed to determine whether DHA can reduce morbidity and mortality in the long term. ●

.

This study was supported by the Russian Science Foundation (grant No. 21-75-10038).

REFERENCES

1. Walters D.M., Cho H.Y., Kleeberger S.R. // Antioxid. Redox Signal. 2008. V. 10. № 2. P. 321–332. doi: 10.1089/ARS.2007.1901.
2. Otoupalova E., Smith S., Cheng G., Thannickal V.J. // Compr. Physiol. 2020. V. 10. № 2. P. 509–547. doi: 10.1002/CPHY.C190017.
3. Gonzalez-Gonzalez F.J., Chandel N.S., Jain M., Budinger G.R.S. // Transl. Res. 2017. V. 190. P. 61–68. doi: 10.1016/J.TRSL.2017.09.005.
4. Diebold L.P., Jain M. // Am. J. Respir. Cell Mol. Biol. 2023. V. 69. № 1. P. 3–5. doi: 10.1165/RCMB.2023-0110ED.
5. Huo R., Huang X., Yang Y., Yang Y., Lin J. // Front. Pharmacol. 2023. V. 14. P. 1139460. doi: 10.3389/FPHAR.2023.1139460.
6. Hohmann M.S., Habiel D.M., Coelho A.L., Verri W.A., Hogaboam C.M. // Am. J. Respir. Cell Mol. Biol. 2019. V. 60. № 1. P. 28–40. doi: 10.1165/RCMB.2017-0289OC.
7. Boots A.W., Veith C., Albrecht C., Bartholome R., Drittij M.J., Claessen S.M.H., Bast A., Rosenbruch M., Jonkers L., van Schooten F.J., et al. // BMC Pulm. Med. 2020. V. 20. № 1. doi: 10.1186/S12890-020-1142-X.
8. Yuan L., Sun Y., Zhou N., Wu W., Zheng W., Wang Y. // Front. Pharmacol. 2022. V. 13. P. 845600. doi: 10.3389/FPHAR.2022.845600.
9. Impellizzeri D., Talero E., Siracusa R., Alcaide A., Cordaro M., Maria Zubelia J., Bruschetta G., Crupi R., Esposito E., Cuzzocrea S., et al. // Br. J. Nutr. 2015. V. 114. № 6. P. 853–865. doi: 10.1017/S0007114515002597.
10. van Alem C.M.A., Metselaar J.M., van Kooten C., Rotmans J.I. // Pharmaceutics. 2021. V. 13. № 7. P. 1004. doi: 10.3390/PHARMACEUTICS13071004.
11. Liu J., Wu Z., Liu Y., Zhan Z., Yang L., Wang C., Jiang Q., Ran H., Li P., Wang Z. // J Nanobiotechnology. 2022. V. 20. № 1. P. 213. doi: 10.1186/S12951-022-01435-4.
12. Li D., Zhao A., Zhu J., Wang C., Shen J., Zheng Z., Pan F., Liu Z., Chen Q., Yang Y. // Small. 2023. V. 19. № 30. e2300545. doi: 10.1002/SMLL.202300545.
13. Cheng D., Li Z., Wang Y., Xiong H., Sun W., Zhou S., Liu Y., Ni C. // J. Transl. Med. 2022. V. 20. № 1. P. 523. doi: 10.1186/S12967-022-03740-W.
14. Ashkar A., Sosnik A., Davidovich-Pinhas M. // Biotechnol. Adv. 2022. V. 54. P. 107789. doi: 10.1016/J.BIOTECHADV.2021.107789.

15. Managuli R.S., Raut S.Y., Reddy M.S., Mutalik S. // Expert. Opin. Drug Deliv. 2018. V. 15. № 8. P. 787–804. doi: 10.1080/17425247.2018.1503249.
16. Zhang L., Wang S., Zhang M., Sun J. // J. Drug Target. 2013. V. 21. № 6. P. 515–527. doi: 10.3109/1061186X.2013.789033.
17. Jash A., Ubeyitogullari A., Rizvi S.S.H. // J. Mater. Chem. B. 2021. V. 9. № 24. P. 4773–4792. doi: 10.1039/D1TB00126D.
18. Mereuta I., Valica V., Parii S., Caraus V., Clecicov M., Svet V., Cernat M. // Revistă ştiinţifico-practică. 2016. V. 2. № 1. P. 75–83.
19. Matveev D.V., Gavrilova S.A., Kuznetsov M.R., Akhmetshina M.R., Ivanov E.V., Evteev A.V., Kuznetsova M.M., Nochnoy M.S. // Head and Neck J. 2022. V. 10. № 4. P. 16–23. doi: 10.25792/HN.2022.10.4.16-23.
20. Ovcharuk E.A., Khabarov S.V., Khadartseva K.A. // J. New Med. Technol. 2018. V. 25. № 3. P. 87–95. doi: 10.24411/1609-2163-2018-16234.
21. Mereuţă I., Parii S., Carauş V., Valica V. // Revista Farmaceutică a Moldovei. 2016. V. 1. № 4. P. 27–27.
22. Danaei N., Kokhdan E.P., Sadeghi H., Sadeghi H., Hassanzadeh S., Rostamzadeh D., Azarmehr N., Ghoran S.H. // Evid Based Complement Alternat Med. 2022. V. 2022. P. 1–9. doi: 10.1155/2022/6208102.
23. Ren Y.-X., Zhou R., Tang W., Wang W.-H., Li Y.-C., Yang Y.-F., Zuo J.-P. // Acta Pharmacol. Sin. 2007. V. 28. № 4. P. 518–525. doi: 10.1111/j.1745-7254.2007.00524.x.
24. Togao O., Tsuji R., Ohno Y., Dimitrov I., Takahashi M. // Magn. Reson. Med. 2010. V. 64. № 5. P. 1491–1498. doi: 10.1002/MRM.22521.
25. Stecker I.R., Freeman M.S., Sitaraman S., Hall C.S., Niedbalski P.J., Hendricks A.J., Martin E.P., Weaver T.E., Cleveland Z.I. // J. Magn. Reson. Open. 2021. V. 6–7. P. 100013. doi: 10.1016/J.JMRO.2021.100013.
26. Schneider C.A., Rasband W.S., Eliceiri K.W. // Nat. Methods. 2012. V. 9. № 7. P. 671–675. doi: 10.1038/NMETH.2089.
27. Gharaee-Kermani M., Hatano K., Nozaki Y., Phan S.H. // Am. J. Pathol. 2005. V. 166. № 6. P. 1593–1606. doi: 10.1016/S0002-9440(10)62470-4.
28. Babin A.L., Cannet C., Gérard C., Wyss D., Page C.P., Beckmann N. // J. Magn. Reson. Imaging. 2011. V. 33. № 3. P. 603–614. doi: 10.1002/JMRI.22476.
29. Scotton C.J., Hayes B., Alexander R., Datta A., Forty E.J., Mercer P.F., Blanchard A., Chambers R.C. // Eur. Respir. J. 2013. V. 42. № 6. P. 1633–1645. doi: 10.1183/09031936.00182412.
30. Izbicki G., Segel M.J., Christensen T.G., Conner M.W., Breuer R. // Int. J. Exp. Pathol. 2002. V. 83. № 3. P. 111. doi: 10.1046/J.1365-2613.2002.00220.X.
31. Mouratis M.A., Aidinis V. // Curr. Opin. Pulm. Med. 2011. V. 17. № 5. P. 355–361. doi: 10.1097/MCP.0B013E328349AC2B.
32. Li S., Shi J., Tang H. // Cell Biol. Toxicol. 2022. V. 38. № 5. P. 699–723. doi: 10.1007/S10565-021-09676-Z.
33. Moore B.B., Hogaboam C.M. // Am. J. Physiol. Lung Cell. Mol. Physiol. 2008. V. 294. № 2. P. L152-L160. doi: 10.1152/AJPLUNG.00313.2007.
34. Ishida Y., Kuninaka Y., Mukaida N., Kondo T. // Int. J. Mol. Sci. 2023. V. 24. № 4. P. 3149. doi: 10.3390/IJMS24043149.
35. Della Latta V., Cecchettini A., Del Ry S., Morales M.A. // Pharmacol. Res. 2015. V. 97. P. 122–130. doi: 10.1016/J.PHRS.2015.04.012.

7-Methylguanine Inhibits Colon Cancer Growth *in Vivo*

K. I. Kirsanov[1,2], T. I. Fetisov[1], E. E. Antoshina[1], T. G. Gor'kova[1], L. S. Trukhanova[1], S. I. Shram[3], I. Yu. Nagaev[3], Yu. A. Zolotarev[3], L. Abo Qoura[1,2], V. S. Pokrovsky[1,2], M. G. Yakubovskaya[1], V. K. Švedas[4,5], D. K. Nilov[4*]

[1]Blokhin National Medical Research Center of Oncology, Institute of Carcinogenesis, Moscow, 115478 Russian Federation

[2]RUDN University, Medical Institute, Moscow, 117198 Russian Federation

[3]National Research Centre "Kurchatov Institute", Moscow, 123182 Russian Federation

[4]Lomonosov Moscow State University, Belozersky Institute of Physicochemical Biology, Moscow, 119991 Russian Federation

[5]Lomonosov Moscow State University, Faculty of Bioengineering and Bioinformatics, Moscow, 119234 Russian Federation

[*]E-mail: nilovdm@gmail.com

Received: May 08, 2024; in final form, June 26, 2024

DOI: 10.32607/actanaturae.27422

ABSTRACT **7-Methylguanine (7-MG) is a natural inhibitor of poly(ADP-ribose) polymerase 1 and tRNA-guanine transglycosylase, the enzymatic activity of which is central for the proliferation of cancer cells. Recently, a number of preclinical tests have demonstrated the safety of 7-MG and a regimen of intragastric administration was established in mice. In the present work, the pharmacological activity of 7-MG was studied in BALB/c and BALB/c nude mice with transplanted tumors. It was found that 7-MG effectively penetrates tumor tissue and suppresses colon adenocarcinoma growth in the Akatol model, as well as in a xenograft model with human HCT116 cells.**

KEYWORDS **7-methylguanine, inhibitor, poly(ADP-ribose) polymerase 1, tRNA-guanine transglycosylase, colon cancer, BALB/c mice.**

ABBREVIATIONS **i.p. – intraperitoneal administration; i.g. – intragastric administration; 7-MG – 7-methylguanine; PARP-1 – poly(ADP-ribose) polymerase 1; TGT – tRNA-guanine transglycosylase.**

INTRODUCTION

7-Methylguanine (7-MG) is a nucleic acid metabolite that is found in small amounts in human blood and urine [1]. The study of 7-MG as a potential antitumor inhibitor began with virtual screening of natural nitrogenous bases and their derivatives against poly(ADP-ribose) polymerase 1 (PARP-1), a key DNA repair enzyme [2]. Modeling demonstrated complementarity between 7-MG and the PARP-1 active site, and further *in vitro* experiments confirmed the assumption about the competitive inhibition mechanism [3–5]. 7-MG also inhibits tRNA-guanine transglycosylase (TGT), an enzyme involved in the translation mechanism [6]. It was noted that knockout/knockdown of the TGT gene reduced the proliferation and migration of cancer cells [7].

The synthetic PARP-1 inhibitors olaparib, rucaparib, and niraparib are used in medicine as innovative anticancer drugs, but they come with serious side effects (in particular, myelodysplastic syndrome/acute myeloid leukemia) [8, 9]. At the same time, the natural inhibitor 7-MG demonstrated that it is safe in our toxicology study; a regimen of intragastric (i.g.) administration was established in mice – 50 mg/kg, 3 times per week [10]. The presence of several relevant targets (PARP-1, TGT) and the safety of 7-MG suggest prospects for further *in vivo* studies. This report describes for the first time the anticancer activity of 7-MG in colon adenocarcinoma models.

EXPERIMENTAL

BALB/c mice (male, 4 weeks old) were obtained from the breeding of the Blokhin NMRCO. A sample of mouse adenocarcinoma Akatol [11] was obtained from the tumor collection of the Blokhin NMRCO. A suspension of tumor cells (0.5 ml, 0.1 g/ml) was subcutaneously injected into the suprascapular area. Treatment with the test compounds began on day 5

after inoculation. Mice were divided into groups of 9 animals each: control group I, water (i.g., 3 times per week); group II, cisplatin (2.5 mg/kg i.p., 2 times per week for 1 week); group III, 7-MG (50 mg/kg i.g., 3 times per week); and group IV, 7-MG + cisplatin. To prepare a 7-MG suspension (5 mg/ml), the compound was mixed with distilled water, vortexed, and left in an ultrasonic bath for 5 min at a temperature of 45°C. The resulting 7-MG suspension was administered by gavage. In combination treatment, 7-MG was administered 3 h prior to cisplatin. The volume of tumor formed was determined using the formula $V = 1/2 \times length \times width^2$. The analysis of the results was conducted after the average tumor volume in the control group reached 4 000 mm^3.

A pharmacokinetic experiment was performed in male BALB/c mice on day 15 after Akatol inoculation. Mice were deprived of food for 18 h before the experiment. The animals were administered a single dose of 7-MG (50 mg/kg i.g.), and blood and tumor tissue samples were collected after 15 min (2 mice), 60 min (2 mice), and 180 min (3 mice). The samples were then frozen and subjected to lyophilization, mechanical grinding, and sequential extraction with solvents (aqueous 90% acetonitrile containing 2% trifluoroacetic acid, acetone, and aqueous 0.1% heptafluorobutyric acid). The quantitative analysis of 7-MG was performed by liquid chromatography-mass spectrometry; an LCQ Advantage MAX mass spectrometer (Thermo Electron Co., USA) was used, equipped with a Surveyor Plus high-performance liquid chromatography system and an ESI ionization source. Deuterated 7-MG, obtained by solid state isotope exchange [12], was used as an internal standard.

Immunodeficient BALB/c nude mice (female, 6–7 weeks old) were obtained from the breeding of the Laboratory of Biochemical Fundamentals of Pharmacology and Tumor Models at the Blokhin NMRCO. A suspension of HCT116 human cancer cells (0.2 ml, 1.2×10^6 cells/ml) was subcutaneously injected into both the right and left flanks of the mouse. Treatment with the test compounds began on day 10 after inoculation. Mice were divided into groups of 4 animals each: control group I, potassium phosphate buffer (i.p., 3 times per week); group II, cisplatin (1 mg/kg i.p., 3 times per week for 1 week); group III, 7-MG (50 mg/kg i.g., 3 times per week); and group IV, 7-MG + cisplatin. In combination treatment, 7-MG was administered 3 h prior to cisplatin. The tumor volume was determined using the formula $V = \pi/6 \times length \times width \times depth$.

All animal experiments were conducted in accordance with the requirements of the Local Blokhin NMRCO Committee for the Ethics of Animal Experimentation.

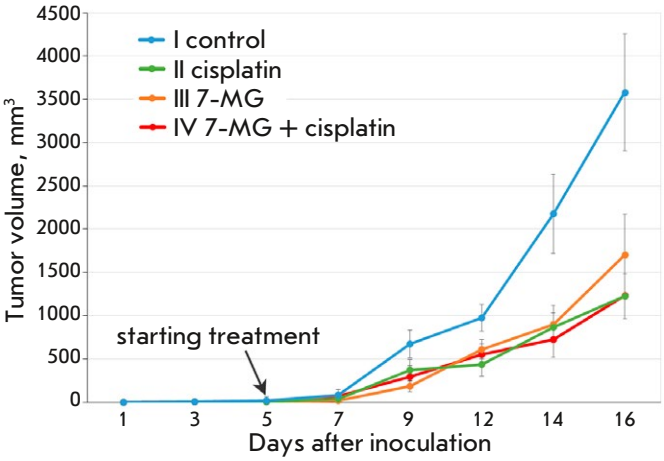

Fig. 1. Dynamics of colon adenocarcinoma growth in the Akatol model

RESULTS AND DISCUSSION

The biological activity of the 7-MG inhibitor upon i.g. administration was studied in the Akatol mouse model of colon cancer. The classic genotoxic agent, cisplatin, whose effectiveness had been previously demonstrated in the Akatol model, was used as a reference drug. On day 16 of the experiment, a significant inhibition of tumor growth by cisplatin (65.8%), 7-MG (52.5%), and their combination (65.5%) was observed (*Fig. 1*). The effects of the well-known chemotherapy drug cisplatin and the discovered PARP-1 inhibitor 7-MG were comparable, and the use of their combination did not appear to increase the antitumor activity.

According to guidelines for mouse handling, an animal can be excluded from the experimental group when a critical tumor size (4 000 mm^3) has developed. The time required for the tumor to reach such a size can be considered as the animal's survival after transplantation. *Figure 2* shows the survival curves, and that a significant increase in survival can be seen for the cisplatin and 7-MG groups.

To confirm the accumulation of 7-MG in the transplanted Akatol tumor tissue, a pharmacokinetic experiment was performed. The content of 7-MG in the tumor gradually increased following i.g. administration, and after 15, 60, and 180 min, it reached 218 ± 13, 460 ± 28, and 989 ± 59 ng/g, respectively. The ratio of 7-MG concentrations in the tumor and blood remained virtually unchanged and was on average 0.44, which, taking into account the low vascularization of the tissue, indicates effective tumor penetration of 7-MG.

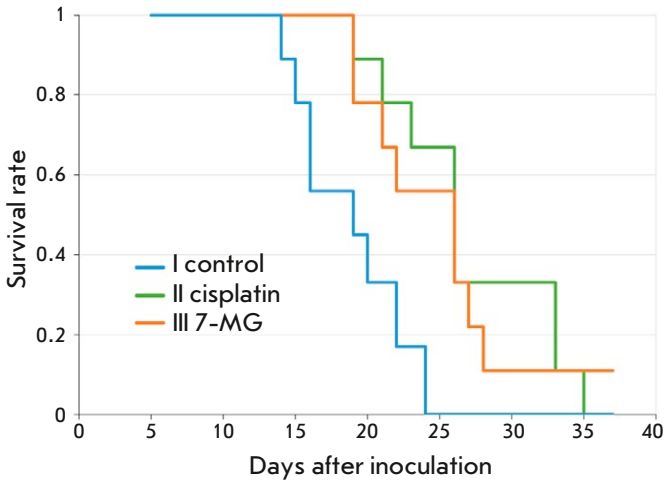

Fig. 2. Survival of mice with an inoculated Akatol tumor (animals were excluded from the group when the tumor size reached 4 000 mm^3)

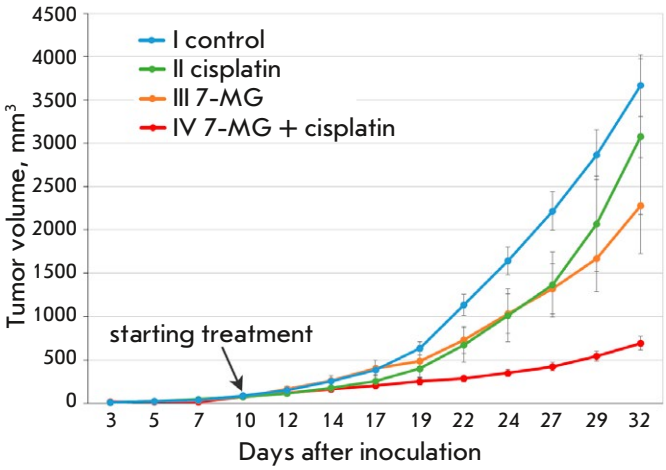

Fig. 3. Dynamics of colon adenocarcinoma growth in a xenograft model

The antitumor activity of 7-MG was also tested in a xenograft model of colon cancer obtained by transplanting HCT116 human cancer cells into the mice. On day 32 of the experiment, cisplatin, 7-MG, and their combination inhibited tumor growth by 16.1, 37.8, and 80%, respectively (*Fig. 3*). Interestingly, the combination of 7-MG and cisplatin resulted in an additive effect that was not observed in the Akatol model. It is likely that HCT116 human cancer cells are more sensitive to a combined treatment with these two agents.

CONCLUSIONS

An *in vivo* analysis of the antitumor activity of the natural compound 7-MG was conducted in the Akatol colon cancer model, as well as in a xenograft model with human HCT116 tumor cells. Inhibition of tumor growth with 7-MG treatment indicates the high effectiveness of the compound in an established regimen (50 mg/kg i.g., 3 times per week). Through a liquid chromatography-mass spectrometry analysis, high accumulation of 7-MG in tumor tissue was demonstrated. In the case of the xenograft model, the combined administration of 7-MG and the well-known chemotherapeutic drug cisplatin resulted in a significant increase in the antitumor effect (growth inhibition of 80%). The obtained data show promise for further studies of 7-MG as a new anticancer agent. ●

This work was supported by the Russian Science Foundation (grant No. 19-74-10072). The production of deuterated 7-MG was carried out within the state assignment of the NRC "Kurchatov Institute".

REFERENCES

1. Topp H., Sander G., Heller-Schöch G., Schöch G. // Anal. Biochem. 1987. V. 161. P. 49–56.
2. Nilov D.K., Tararov V.I., Kulikov A.V., Zakharenko A.L., Gushchina I.V., Mikhailov S.N., Lavrik O.I., Švedas V.K. // Acta Naturae. 2016. V. 8. № 2. P. 108–115.
3. Nilov D., Maluchenko N., Kurgina T., Pushkarev S., Lys A., Kutuzov M., Gerasimova N., Feofanov A., Švedas V., Lavrik O., et al. // Int. J. Mol. Sci. 2020. V. 21. P. 2159.
4. Kurgina T.A., Shram S.I., Kutuzov M.M., Abramova T.V., Shcherbakova T.A., Maltseva E.A., Poroikov V.V., Lavrik O.I., Švedas V.K., Nilov D.K. // Biochemistry (Mosc.). 2022. V. 87. P. 823–831.
5. Shram S.I., Shcherbakova T.A., Abramova T.V., Baradieva E.C., Efremova A.S., Smirnovskaya M.S., Silnikov V.N., Švedas V.K., Nilov D.K. // Biochemistry (Mosc.). 2023. V. 88. P. 783–791.
6. Pushkarev S.V., Vinnik V.A., Shapovalova I.V., Švedas V.K., Nilov D.K. // Biochemistry (Mosc.). 2022. V. 87. P. 443–449.
7. Zhang J., Lu R., Zhang Y., Matuszek Ż., Zhang W., Xia Y., Pan T., Sun J. // Cancers (Basel). 2020. V. 12. P. 628.
8. Ohmoto A., Yachida S. // Onco Targets Ther. 2017. V. 10. P. 5195–5208.
9. Mittica G., Ghisoni E., Giannone G., Genta S., Aglietta M., Sapino A., Valabrega G. // Recent Pat. Anticancer Drug Discov. 2018. V. 13. P. 392–410.
10. Kirsanov K., Fetisov T., Antoshina E., Trukhanova L., Gor'kova T., Vlasova O., Khitrovo I., Lesovaya E., Kulbachevskaya N., Shcherbakova T., et al. // Front. Pharmacol. 2022. V. 13. P. 842316.
11. Fetisov T.I., Tilova L.R., Lesovaya E.A., Antoshina E.E., Gor'kova T.G., Trukhanova L.S., Morozova O.V., Shipaeva E.V., Ivanov R.V., Purmal A.A., et al. // Adv. Mol. Oncol. 2016. V. 3. P. 67–72.
12. Zolotarev Y.A., Dadayan A.K., Borisov Y.A., Kozik V.S. // Chem. Rev. 2010. V. 110. P. 5425–5446.

Ceramides As Potential New Predictors of the Severity of Acute Coronary Syndrome in Conjunction with SARS-CoV-2 Infection

N. G. Lozhkina[1,2,3], O. I. Gushchina[2,3*], N. V. Basov[1,4], E. V. Gaisler[1], A. D. Rogachev[1,4], Yu. S. Sotnikova[1,4,5], Yu. V. Patrushev[1,5], A. G. Pokrovsky[1]

[1]Novosibirsk State University, Novosibirsk, 630090 Russian Federation

[2]Federal Research Center for Fundamental and Translational Medicine, Novosibirsk, 630117 Russian Federation

[3]City Clinical Hospital No. 1, Novosibirsk 630047 Russian Federation

[4]Vorozhtsov Novosibirsk Institute of Organic Chemistry, Novosibirsk, 630090 Russian Federation

[5]Boreskov Institute of Catalysis, Novosibirsk, 630090 Russian Federation

*E-mail: Varalenna@yandex.ru

Received March 25, 2024; in final form, June 07, 2024

DOI: 10.32607/actanaturae.27400

ABSTRACT **Acute coronary events (ACEs) associated with a SARS-CoV-2 infection can significantly differ from classic ACEs. New biomarkers, such as ceramides, may help in the diagnosis and treatment of this disease. This study included 73 ACE patients for whom the SARS-CoV-2 infection was verified. Two subgroups were formed: the favorable outcome subgroup and the fatal outcome subgroup. Plasma samples were collected from all patients at the time of admission for a metabolomic analysis. The analysis of metabolites revealed that the ceramide levels were significantly lower in the fatal outcome subgroup than in the survivor subgroup. Therefore, determining ceramide levels in patients with ACEs in conjunction with COVID-19 may help assess the prognosis of these patients and manage their risks.**

KEYWORDS **acute coronary syndrome, myocardial infarction, SARS-CoV-2 infection, metabolomics, ceramides.**

INTRODUCTION

Acute coronary events (ACEs) in conjunction with the SARS-CoV-2 infection can significantly differ from the classic manifestations of this disease. Many symptoms characteristic of a severe viral infection mask the manifestations of acute coronary syndrome. In turn, ACEs can also hide the signs of infection. Respiratory distress, high activity of inflammatory markers, chest pain, and, in severe clinical cases, shock and hypotension are difficult to differentiate at the starting point of their development. One of the major problems in making a clinical diagnosis is the late symptoms of the disease, including the delayed conversion of myocardial necrosis markers. For example, the titers of high-sensitivity troponin in myocardial infarction attain diagnostic significance 4 h after the onset of symptoms [1]. New biomarker sets may be useful in early diagnosis and in choosing the treatment modality. Recently, metabolomics-based strategies have been used to identify the molecular mechanisms involved in cardiovascular diseases.

Metabolomics technologies enable the identification, quantification, and characterization of low molecular weight metabolites weighing less than 1,500 Da [2]. Determination of the metabolomic profile of patients and identification of potential biomarkers may be helpful in early diagnosis of diseases and applications of personalized therapy.

Ceramides are a promising class of signaling molecules. This subclass of lipid molecules constitutes the hydrophobic backbone of all complex sphingolipids (e.g., sphingomyelin (SM), cerebrosides, gangliosides) and structurally consists of an acyl substituent of variable carbon chain length linked to the amino group of a sphingoid base, typically sphingosine. Ceramides are important components of all cell membranes. The fatty acyl chains, usually saturated or monounsaturated, may contain an OH group

linked to C2 or to the terminal carbon atom (α- and ω-hydroxy fatty acids, respectively) [3]. The value of ceramides as diagnostic markers is associated with their high stability at various temperatures (which is reflected in the ease of sampling, storage, and transportation of biological material). The results of studies of the relationship between ceramides and a cardiovascular pathology are contradictory. During the COVID-19 pandemic, these biomarkers were actively studied in patients with different types of infections, but their role in the pathogenesis, course, and prognosis of the acute coronary syndrome associated with the SARS-CoV-2 infection remains unclear. In this regard, assessing the role of a number of key metabolites, in particular ceramides, as potential new predictors of the severity of ACEs in conjunction with SARS-CoV-2 infection seems topical.

EXPERIMENTAL

Research methods and characterization of patients

The study included 73 patients who were consecutively admitted to the regional vascular center No. 1 of the Novosibirsk City Clinical Hospital No. 1 with a diagnosis of acute coronary syndrome (confirmed according to Russian and European clinical guidelines) in whom the SARS-CoV-2 infection was verified (no more than 28 days before or within 14 days after the onset of ACEs). All patients underwent a full range of examinations in accordance with current clinical guidelines for both pathologies: a complete blood count and biochemistry panel, a coagulogram with D-dimer levels, a PCR test for COVID-19, electrocardiography (ECG), echocardiography (EchoCG) at admission, computed tomography of the chest (chest CT), and coronary angiography (CAG) with percutaneous transluminal balloon angioplasty (PTCA) and stenting of the infarct-related artery using modern certified medical equipment [4, 5]. In addition to the standard examination, plasma samples were collected from all patients at the time of admission and frozen at –70°C for a metabolomic analysis that was performed at the Novosibirsk State University. The study protocol was approved at a meeting of the local ethics committee.

Inclusion criteria

Males and females aged 18 to 90 years admitted to the clinic with a diagnosis of acute coronary syndrome (with and without ST segment elevation) confirmed by a typical clinical picture, ECG, selective coronary angiography, and quantitative troponin I determination; a verified diagnosis of the SARS-CoV-2 infection (no more than 28 days before or within 14 days after the onset of an acute coronary event); signed voluntary informed consent.

Exclusion criteria

Lack of signed voluntary informed consent. The study did not include patients with malignant neoplasms, severe autoimmune diseases, terminal somatic pathology (liver cirrhosis of any severity, chronic kidney disease ⩾ S4, patients on long-term hemodialysis), and pre-existing mental disorders at baseline.

Study design

This was an open, continuous, prospective, non-randomized, and parallel group study that included patients with acute coronary syndrome and a verified new coronavirus infection who were consecutively admitted to the emergency cardiology department of City Clinical Hospital No. 1 in 2021–2023. The diagnosis of ACE was established using a set of criteria developed by the European and Russian Societies of Cardiology (2020), which were as follows: a) clinical signs or symptoms of myocardial ischemia; b) ECG changes in two or more consecutive leads for acute ST-elevation myocardial infarction (STEMI) (high-amplitude T wave, negative T wave, ST segment elevation, pathological Q wave, ST segment depression, presence of QR). The diagnosis of a novel coronavirus infection was made according to temporary guidelines for the prevention, diagnosis, and treatment of a novel coronavirus infection (version 13 of October 14, 2021), which included a) a positive result of a SARS-CoV-2 RNA test using a nucleic acid amplification technique (NAAT) or immunochromatographic SARS-CoV-2 antigen testing; b) a high clinical probability (pulmonary CT, clinical picture, and relevant epidemiological history data) [4, 5].

Sample collection, preparation, and analysis

Blood samples were collected from patients on the day of hospital admission. Venous blood was sampled into vacuum tubes containing the K-EDTA anticoagulant. Plasma was obtained by centrifugation, transferred to a clean tube, and frozen at –80°C until sample preparation. Sample preparation was performed according to [6]. Blood plasma (100 μL) was added with 400 μL of a cooled methanol and acetonitrile mixture (1 : 1). Samples were shaken on a shaker and then centrifuged at 16 000 rpm and +4°C for 15 min. The supernatant was transferred into a glass vial insert and analyzed. Samples prepared by mixing equal volumes of patient plasma were used for quality control.

The metabolomic analysis was performed according to [7]. The HPLC-MS/MS analysis was performed

on a Shimadzu LC-20AD Prominence chromatograph equipped with a gradient pump, a SIL-20AC autosampler (Shimadzu, Japan) thermostated at +10°C, and a CTO-10A Svp column thermostat at a temperature of +35°C. Chromatographic separation was performed on a monolithic column with a 1-vinyl-1,2,4-triazole-based sorbent, which was prepared according to the method in [8]. We used an aqueous $(NH_4)_2CO_3$ solution (20 mM) containing 5 vol.% acetonitrile and adjusted to a pH of 9.8 with a 25% ammonia solution as mobile phase A; mobile phase B was pure acetonitrile. The reversed phase chromatography gradient was as follows: 0 min, 0% B; 1 min, 0% B; 6 min, 98% B; 16 min, 98% B, after which the column was equilibrated for 3 min. The hydrophilic chromatography (HILIC) gradient was as follows: 0 min, 98% B; 2 min, 98% B; 6 min, 0% B; 10 min, 0% B, after which the column was equilibrated for 4 min. The flow rate was 300 μL/min, and the sample volume was 2 μL.

Metabolites were detected on an API 6500 QTRAP mass spectrometer (AB SCIEX, USA) equipped with an electrospray ionization source operating in positive and negative ionization modes. Metabolites were detected in the multiple reaction monitoring (MRM) mode. The main mass spectrometric parameters were as follows: the ion spray (IS) voltage was 5,500 V for positive and −4,500 V for negative ionization; drying gas temperature was 475°C; collision cell gas (CAD) was "high"; gas 1, gas 2, and curtain gas pressures were 33, 33, and 30 psi (227.5, 227.5, and 206.8 kPa, respectively); the declustering potential (DP) was ±91 V; the entrance potential (EP) was ±10 V; and the collision cell exit potential (CXP) was ±9 V. Device control and data collection were performed using the Analyst 1.6.3 software (AB SCIEX, USA). The chromatograms were processed using the MultiQuant 2.1 software (AB SCIEX, USA).

The samples were divided into two groups: the favorable outcome (recovery) group and the in-hospital fatal outcome group. Samples from these groups were subjected to a metabolomic analysis, and key metabolites were identified. The difference between the two subgroups of "fatal" and "survived" patients were assessed using the Mann–Whitney test. The critical value for subgroup dimension was $MW_{crit} = 32$.

RESULTS

The selected groups differed significantly in age: the mean age in the first group was 63.6 ± 9.6 years and 73 ± 8.2 years in the second (unfavorable outcome group) ($p = 0.003$). Group 1 included 37 males and 24 females, and group 2 consisted of 5 males and 6 females. All patients who died had ACS with ST elevation; in the favorable outcome group, ST elevation was diagnosed in 56 patients, and ACS without ST elevation was diagnosed in 5 patients.

The severity of the SARS-CoV-2 infection was as follows: in the favorable outcome group, the infection course was mild and asymptomatic, moderate, or severe in 22, 26, and 12 patients, respectively; in the fatal outcome group, the SARS-CoV-2 infection course was asymptomatic, mild, moderate, or extremely severe in 0, 1, 1, and 9 patients, respectively.

Analysis of the clinical and laboratory parameters revealed significant differences between the study subgroups of patients: any form of atrial fibrillation was more common in the fatal outcome group than in the survivor group ($p < 0.5$); the serum iron level was lower in the unfavorable outcome group ($p < 0.001$), and albumin was significantly lower in the unfavorable outcome group than in the survivor group ($p < 0.001$). On the contrary, the D-dimer level was higher in group 2 ($p < 0.0001$). The mean C-reactive protein concentration on admission was significantly lower in group 1 than in group 2 ($p = 0.0243$). Indicators of myocardial contractility of both the left and right ventricles were significantly worse in the fatal outcome group ($p < 0.0001$). No significant differences were found in the degree of coronary artery lesion and lipid panel parameters. Thus, our clinical, laboratory, and instrumental data are consistent with the data of other researchers [9, 10].

At the next stage, key metabolites in the blood plasma of patients were identified. Comparison of the mean indicator values revealed "saturation" of the isolated metabolites with a group of ceramides (19 compounds, *Table 1*), as well as five metabolites from the sphingomyelin (SM) class and four metabolites from the glycosylceramide (GC) class.

Comparative analysis of the levels of the identified metabolites in the samples showed that the plasma levels of all metabolites in fatal outcome patients were noticeably lower than those in survived patients. The only exception was 5-hydroxyindoleacetic acid, whose level increased more than 1.5-fold. *Figure 1* shows the normalized peak areas of several ceramides in the two groups.

DISCUSSION

Ceramides are involved in various cellular processes, including pathological ones. Their levels in resting cells are extremely low, but they can significantly increase under cellular stress or in response to various stimuli (cytokines, apoptosis receptor ligands, antitumor drugs). Furthermore, accumulating evidence indicates that the structural features of different ceramide species may underlie their specificity for certain cellular processes [11]. However, the molecu-

Table 1. The values of the key metabolites in the study groups

Metabolite	MW*	Multiplicity lethal/non-lethal
Ceramide (d18:1/22:0)	4	0.503
Ceramide (d18:1/24:0)	9	0.531
Ceramide (d18:1/24:0 OH)	11	0.579
Ceramide (d18:1/22:2 OH)	12	0.564
Ceramide (d18:1/23:0) or ceramide (d18:1/22:1 OH)	12	0.529
Ceramide (d18:1/25:0)	13	0.524
Glycosphingolipid (18:1/22:0)	13	0.486
Glycosphingolipid (18:1/24:1)	15	0.356
Ceramide (d18:1/20:1 OH)	18	0.621
Ceramide (d18:1/22:0 OH)	18	0.685
Ceramide (d18:1/24:1)	19	0.450
Ceramide (d18:1/20:0)	21	0.658
Ceramide (d18:1/18:0)	23	0.695
Ceramide (d18:1/26:1)	23	0.702
Sphingomyelin (d18:1/22:0 OH)	23	0.663
Ceramide (d18:1/16:0 OH)	24	0.712
Ceramide (d18:1/26:2)	24	0.653
Ceramide (d18:1/16:1 OH)	25	0.731
Ceramide (d18:1/24:2 OH)	27	0.641
Sphingomyelin (d18:1/22:2)	27	0.683
3-Phosphoglyceric acid	28	0.456
Ceramide (d18:1/18:0 OH)	28	0.680
Sphingomyelin (d18:1/24:0)	28	0.569
Ceramide (d18:1/18:1 OH)	29	0.719
Ceramide (d18:1/18:1)	29	0.738
Corticosterone	29	0.594
Glycosphingolipid (18:1/20:0)	29	0.648
Sphingomyelin (d18:1/16:2 OH)	29	0.750
Sphingomyelin (d18:1/18:2 OH)	30	0.686
Plasmalogen (p18:0/22:6)	31	0.655
5-Hydroxyindoleacetic acid	32	1.788
Glycosphingolipid (18:1/16:0)	32	0.561

*MW – Mann–Whitney U-statistic value.

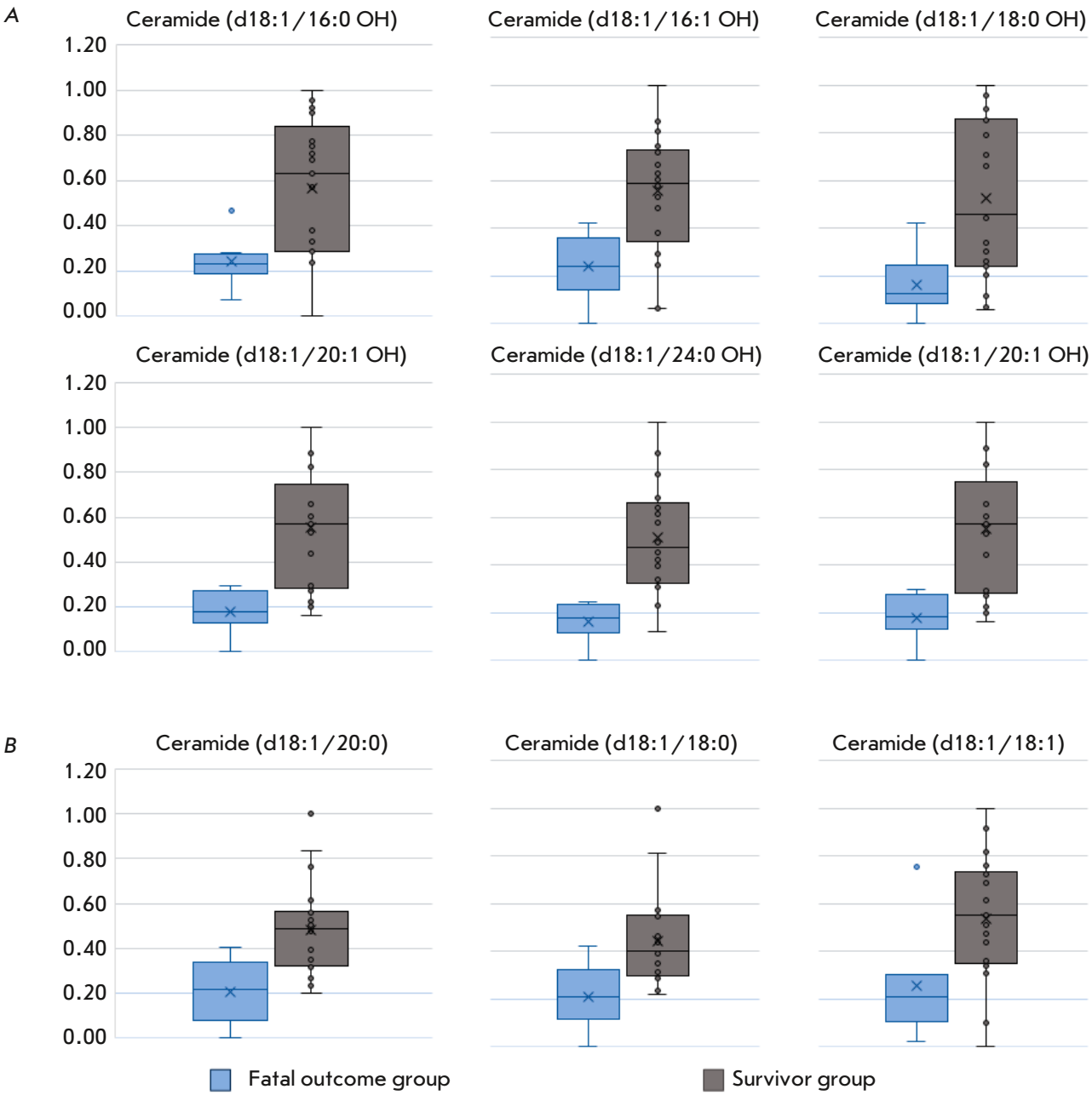

Fig. 1. Plasma ceramide levels in the study groups. (*A*) Hydroxylated ceramides; (*B*) Non-hydroxylated ceramides

lar mechanisms that underlie this specificity and the mode of ceramide action on cells remain to be studied in detail. This mechanism is thought to be associated with changes in the biophysical properties of membranes which occur during ceramide formation. These changes are partially associated with the unique molecular structure of ceramides, in particular their very small functional groups, hydrophobicity, and high melting point, which reduces their miscibility with other membrane lipids. Several studies have reported increased membrane permeability associated with ceramide formation under the action of bacterial sphingomyelin phosphodiesterase (SMase) or addition of ceramides to preformed membranes. It is suggested that the formation of ceramides on the cell membrane may lead to changes in lipid–lipid, lipid–

protein, and protein–protein interactions, which may significantly affect protein activity and thereby signaling processes [12].

There are studies on the role of ceramides in the development and progression of cardiovascular pathology. The development of atherosclerotic plaques is known to be a complex process, mainly associated with inflammation, which begins with endothelial damage and is accompanied by local invasion of immune cells, lipid accumulation, and vascular wall remodeling. Induction of cellular apoptosis was initially thought to be the main cause of ceramide-related cell damage [13]. But later, this suggestion was called into question because cellular ceramide levels were found to increase only at later apoptosis stages [14, 15]. In macrophages, endothelial cells, hepatocytes, and tumor cell lines, such as the MCF7 breast cancer cell line, ceramides have been shown to mediate the cellular effects of the tumor necrosis factor-α (TNF-α) receptor [16]. High ceramide levels were also found to be associated with myocardial cell death in a mouse myocardial infarction model. In addition, ceramides can cause vascular dysfunction via deactivation of endothelial NO synthase [17].

A reduction in ceramide levels in cells and tissues by inhibition of the enzymes involved in ceramide formation prevents the development of atherosclerosis in animal models [18]. In vascular tissues, ceramides are produced in response to hyperglycemia and TNF-α signaling and are involved in NO signaling and inflammation. Elevated ceramide levels in human blood are associated with cardiovascular events. In addition, cardiovascular risk factors, such as obesity and diabetes mellitus, are associated with ceramide accumulation [19].

One of the first studies linking blood ceramide levels and cardiovascular disease progression was conducted by Meikle et al. [20]. Since then, there have been observational studies clearly demonstrating the relationship between certain ceramide subtypes and an increased risk of cardiovascular events. The most comprehensive studies were conducted by the Hilvo Laaksonen groups [21, 22]. These studies were used for developing two different risk scores that demonstrate that, in particular, C16:0, C18:0, and C24:1 ceramides may be markers of high risk of cardiovascular events, which are independent of the other cardiovascular risk factors identified in patients with coronary heart diseases [21, 22]. It should be noted that a relationship between elevated C18:0 ceramide levels and major cardiovascular events was also present in patients without known coronary artery diseases and appeared independent of other cardiovascular risk factors.

Many studies have demonstrated the importance of ceramides in the inflammatory response. For example, ceramides are involved in pro-inflammatory signal transmission in endothelial cells [23]. In the cardiovascular system, inflammatory processes are activated by various stimuli; e.g., pathogen- or damage-associated molecular patterns [24]. Although the exact mechanisms underlying this phenomenon are not fully understood, several studies have demonstrated a correlation between ceramides and activation of inflammatory diseases. This was first reported by Koka et al., who used pharmacological inhibition of acid sphingomyelinase (ASM) by amitriptyline, as well as RNA interference (RNAi), to study endothelial cells of ASM−/− mice to show that ASM mediates the inflammatory response involving the inflammasome NLR family pyrin domain-containing protein 3 (NLRP3) [25]. These results were confirmed *in vivo* in ASM−/− mice and were also replicated in a study using RNAi against ASM in endothelial cells [26]. The role of ceramides in NLRP3 activation in macrophages is less clear. Camell et al. [27] did not find that the *de novo* synthesis pathway, which involves serine palmitoyltransferase, participates in the activation of inflammation. However, other pathways of ceramide production were not analyzed. Scheiblich et al. showed that SPT activation or external application of non-physiological C2 ceramide leads to NLRP3 activation and interleukin-1β (IL-1β) release in microglial cells [28]. Administration of ceramide C2 led to the activation of inflammation in bone marrow-derived macrophages [29]. It has been suggested that ceramides and inflammation activation are related [30, 31]. In particular, ceramides produced in reaction to ASM appear to be important for inflammatory signaling [32]. Finally, it remains unclear whether ceramides are directly activated during inflammatory processes or if activation is mediated by pathogen- or damage-associated molecular patterns. Evidence of direct activation of inflammation by ceramides is currently lacking.

Ceramides and SARS-CoV-2

Research has demonstrated that ceramide levels can be both elevated and decreased in SARS-CoV-2. Elevated ceramide levels may be associated with the activation of apoptosis, which leads to cell death and probably promotes inflammatory processes typical of severe forms of COVID-19. On the other hand, a decrease in ceramide levels may be associated with a depletion of their precursors or disruption of their synthesis by the virus [33, 34]. Although the mechanism of binding of the SARS-CoV-2 virus to its receptor [35, 36], angiotensin-converting enzyme 2 (ACE2), and TMPRSS2 protease, which activates vi-

ral polymerase, is well understood, changes in the cell membrane during infection are a complex and multifactorial process. Virus processing in the host cell is accompanied by significant changes in the membrane lipid composition, in particular changes in the levels of ceramides and other sphingolipids. These changes can be caused not only by apoptosis, but also by the virus that is able to alter membrane composition to optimize its replication, affecting the levels of ceramides and other lipids; disruption of the normal lipid metabolism in the cell, which can lead to changes in the levels of ceramides and other lipids. These pathological processes are involved in microvascular damage in SARS-CoV-2 and are, therefore, associated with cardiovascular complications in SARS-CoV-2 patients.

CONCLUSION

The present study examined a unique disease phenotype – a conjunction of acute coronary syndrome with SARS-CoV-2. Comparison with ACEs without SARS-CoV-2 revealed increased ceramide levels in the group of ACEs without SARS-CoV-2, which may indicate that they play a role in the pathogenesis of this disease combination. In addition, there was a paradoxical response of the body's metabolic system to an acute coronary event in conjunction with COVID-19: ceramide levels were significantly lower in the fatal outcome subgroup than in the survivor subgroup. The low ceramide levels in fatal outcome patients may be explained by a depletion of the precursors of these metabolites in the terminal condition, which may be due to the influence of the non-structural SARS-CoV-2 proteins that activate the metabolic pathways involved in apoptosis and inflammation. Also, active production of viral particles may lead to cellular exhaustion and destruction of the cell membrane, which may explain the unusually high levels of cell membrane components in the plasma of SARS-CoV-2 patients. But this phenomenon requires further study.

Therefore, this pilot study has showed that metabolomic profiling with a focus on ceramide levels may help assess the risk of a fatal outcome in patients with acute coronary syndrome in conjunction with the SARS-CoV-2 infection. Our findings need confirmation in other patient populations. ●

Conflict of interest.
The authors declare no conflict of interest.
Funding sources: none.

REFERENCES

1. Westwood M., Ramaekers B., Grimm S., Worthy G., Fayter D., Armstrong N., Buksnys T., Ross J., Joore M., Kleijnen J. // Health Technol. Assess. 2021. V. 25. № 33. P. 1–276.
2. Zhang A., Sun H., Wang P., Han Y., Wang X. // J. Proteomics. 2012. V. 75. № 4. P. 1079–1088.
3. Colombini M. Ceramide Channels // Adv. Exp. Med. Biol. 2019. V. 1159. P. 33–48.
4. 2020 Clinical practice guidelines for Acute ST-segment elevation myocardial infarction // Russian Journal of Cardiology. 2020. V. 25. № 11. P. 4103.
5. Temporary methodological recommendations "Prevention, diagnosis, and treatment of novel coronavirus infection (COVID-19). Version 17 (12.09.2022)". Ministry of Health of the Russian Federation. 2022. P. 1–210.
6. Li K., Naviaux J.C., Bright A.T., Wang L., Naviaux R.K. // Metabolomics. 2017. V. 13 № 10. P. 122.
7. Basov N.V., Rogachev A.D., Aleshkova M.A., Gaisler E.V., Sotnikova Y.S., Patrushev Y.V., Tolstikova T.G., Yarovaya O.I., Pokrovsky A.G., Salakhutdinov N.F. // Talanta. 2023. V. 267. P. 125168.
8. Patrushev Y.V., Sotnikova Y.S., Sidelnikov V.N. // Protect. Met. Phys. Chem. Surf. 2020. V. 56. № 1. P. 49–53.
9. Wu Z., McGoogan J.M. // JAMA. 2020. V. 323. №13. P. 1239–1242.
10. Akhtar Z., Chowdhury F., Aleem M.A. Ghosh P.K. Rahman M. Rahman M. Hossain M.E. Sumiya M.K. Islam A.M. Uddin M.J., et al. // Open Heart 2021. V. 8. e001617.
11. Colombini M. // J. Bioenerg Biomembr. 2017. V. 49. № 1. P. 57–64.
12. Chaurasia B., Summers S.A. // Annu. Rev. Physiol. 2021. V. 10. № 83. P. 303–330.
13. Hannun Y.A. // J. Biol. Chem. 1994. V. 4. № 269. № 5. P. 3125–3128.
14. Watts J.D., Gu M., Patterson S.D., Aebersold R., Polverino A.J. // Cell Death Differ. 1999. V. 6. P. 105–114.
15. Thomas R.L., Matsko C.M., Lotze M.T., Amoscato A.A. // J. Biol. Chem. 1999. V. 274. P. 80–88.
16. Al-Rashed F., Ahmad Z., Thomas R., Melhem M., Snider A.J., Obeid L.M., Al-Mulla F., Hannun Y.A., Ahmad R. // Sci. Rep. 2020. V. 10. P. 16802.
17. Lallemand T., Rouahi M., Swiader A., Grazide M.H., Geoffre N., Alayrac P., Recazens E., Coste A., Salvayre R., Nègre-Salvayre A., et al. // Arterioscler. Thromb. Vasc. Biol. 2018. V. 38. P. 1479–1492.
18. Choi R.H., Tatum S.M., Symons J.D., Summers S.A., Holland W.L. // Nat. Rev. Cardiol. 2021. V. 18. № 10. P. 701–711.
19. Junqueira D.L.M., Stach A., Caixeta A., Sallum J., Yasaki E., Tsutsui J., Rizatti E., Rochitte C.E., Ching-Jianhong, Kovalik J.P., et al. // Arq. Bras. Cardiol. 2022. V. 118. № 4. P. 768–777.
20. Meikle P.J., Hopwood J.J., Clague A.E., Carey W.F. // JAMA. 1999. V. 281. № 3. P. 249–254.
21. Hilvo M., Vasile V.C., Donato L.J., Hurme R., Laaksonen R. // Front. Endocrinol. (Lausanne). 2020. V. 11. P. 628.
22. Havulinna A.S., Sysi-Aho M., Hilvo M., Kauhanen D., Hurme R., Ekroos K., Salomaa V., Laaksonen R. // Arterioscler. Thromb. Vasc. Biol. 2016. V. 36. P. 2424–2430.
23. Laaksonen R., Ekroos K., Sysi-Aho M., Hilvo M., Vihervaara T., Kauhanen D., Suoniemi M., Hurme R., März

W., Scharnagl H., et al. // Eur. Heart J. 2016. V. 37. № 25. P. 1967–1976.
24. Takahashi M. // Cardiovasc. Res. 2022. V. 118. P. 372–385.
25. Koka S., Xia M., Chen Y., Bhat O.M., Yuan X., Boini K.M., Li P.L. // Redox Biol. 2017. V. 13. P. 336–344.
26. Chen Y., Yuan M., Xia M., Wang L., Zhang Y., Li P.L. // Front. Biosci. 2016. V. 21. P. 635–650.
27. Camell C.D., Nguyen K.Y., Jurczak M.J., Christian B.E., Shulman G.I., Shadel G.S., Dixit V.D. // J. Biol. Chem. 2015. V. 290. P. 402–413.
28. Scheiblich H., Schlütter A., Golenbock D.T., Latz E., Martinez-Martinez P., Heneka M.T. // J. Neurochem. 2017. V. 143. № 5. P. 534–550.
29. Vandanmagsar B., Youm Y.H., Ravussin A., Galgani J.E., Stadler K., Mynatt R.L., Ravussin E., Stephens J.M., Dixit V.D. // Nat. Med. 2011. V. 17. P. 179–188.
30. Hong J., Bhat O.M., Li G., Dempsey S.K., Zhang Q., Ritter J.K., Li W., Li P.L. // Biochim. Biophys. Acta Mol. Cell. Res. 2019. V. 1866. P. 849–860.
31. Grassmé H., Carpinteiro A., Edwards M.J., Gulbins E., Becker K.A. // Cell Physiol. Biochem. 2014. V. 34. P. 45–55.
32. Li C., Guo S., Pang W., Zhao Z. // Front. Cell Dev. Biol. 2019. V. 7. P. 378.
33. Wang H., Liu C., Xie X., Niu M., Wang Y., Cheng X., Zhang B., Zhang D., Liu M., Sun R., et al. // Immunity. 2023. V. 56. № 6. P. 1410–1428.
34. Gui Y.K., Li Q., Liu L., Zeng P., Ren R.F., Guo Z.F., Wang G.H., Song J.G., Zhang P. // Brain Res. Bull. 2020. V. 158. P. 122–127.
35. Kornhuber J., Hoertel N., Gulbins E. // Mol. Psychiatry. 2022. V. 27. № 1. P. 307–314.
36. Ivanisenko V.A., Gaisler E.V., Basov N.V., Rogachev A.D., Cheresiz S.V., Ivanisenko T.V., Demenkov P.S., Mishchenko E.L., Khripko O.P., Khripko Y.I., et al. // Sci. Rep. 2022. V. 12. № 1. P. 977.

LPS-Induced Acute Lung Injury: Analysis of the Development and Suppression by the TNF-α-Targeting Aptamer

A. V. Sen'kova*, I. A. Savin, E. L. Chernolovskaya, A. S. Davydova, M. I. Meschaninova, A. Bishani, M. A. Vorobyeva, M. A. Zenkova
Institute of Chemical Biology and Fundamental Medicine, Siberian Branch of the Russian Academy of Sciences, Novosibirsk, 630090 Russian Federation
*E-mail: alsenko@mail.ru
Received March 22, 2024; in final form, April 15, 2024
DOI: 10.32607/actanaturae.27393

ABSTRACT **Acute lung injury (ALI) is a specific form of lung inflammation characterized by diffuse alveolar damage, noncardiogenic pulmonary edema, as well as a pulmonary and systemic inflammation. The pathogenesis of ALI involves a cascade inflammatory response accompanied by an increase in the local and systemic levels of proinflammatory cytokines and chemokines. The development of molecular tools targeting key components of cytokine signaling appears to be a promising approach in ALI treatment. The development of lipopolysaccharide (LPS)-induced ALI, as well as the feasibility of suppressing it by an aptamer targeting the proinflammatory cytokine TNF-α, was studied in a mouse model. The TNF-α level was shown to increase significantly and remain steadily high during the development of ALI. LPS-induced morphological signs of inflammation in the respiratory system become most pronounced 24 h after induction. Intranasal administration of TNF-α-targeting aptamers conjugated with polyethylene glycol (PEG-aptTNF-α) to mice with ALI reduced the intensity of inflammatory changes in lung tissue. Assessment of the levels of potential TNF-α target genes (*Usp18*, *Traf1*, and *Tnfaip3*) showed that their expression levels in the lungs increase during ALI development, while declining after the application of PEG-aptTNF-α. Therefore, topical use of TNF-α-targeting aptamers may be an efficient tool for treating ALI and other inflammatory lung diseases.**
KEYWORDS **acute lung injury, proinflammatory cytokines, aptamers, target genes.**
ABBREVIATIONS **ALI – acute lung injury; ARDS – acute respiratory distress syndrome; TNF-α –tumor necrosis factor α; aptTNF-α – TNF-α-targeting aptamer; PEG – polyethylene glycol; LPS – lipopolysaccharide; BALF – bronchoalveolar lavage fluid.**

INTRODUCTION

Acute lung injury (ALI) and its sequela, acute respiratory distress syndrome (ARDS), refer to a specific form of lung inflammation characterized by diffuse alveolar damage, noncardiogenic pulmonary edema, as well as pulmonary and systemic neutrophil-associated inflammation [1, 2]. The etiological factors for ALI and ARDS can include various stimuli and diseases such as bacterial and viral pneumonia [3, 4], mechanical ventilation [5, 6], exposure to chemical agents [7, 8], traumatic brain injury [9], sepsis [10, 11], acute pancreatitis [12], and many other pathologies. The recent rise in morbidity and mortality from ALI/ARDS has been associated with the new coronavirus infection (COVID-19) pandemic caused by coronavirus associated with the severe acute respiratory distress syndrome (SARS-CoV-2) [13, 14]. The pathogenesis of ALI/ARDS involves the development of local and systemic cascade inflammatory responses, accompanied by the elevation of the levels of proinflammatory cytokines (TNF-α, IFN-γ, IL-6, IL-1β, GM-CSF, and G-CSF) and chemokines (CXCL10/IP10, MIP-1α, and CCL2) up to critical values, resulting in the development of multiple organ failure [14–16].

Today, the treatment of ARDS and its accompanying immune disorders is for the most part symptomatic; it aims to alleviate symptoms and often involves mechanical ventilation and the administration of corticosteroids. The use of molecular genetic tools targeting key cytokines can be a promising approach in treating this pathology. Monoclonal antibodies against TNF-α, IL-6, IL-1β, IFN-γ, and other components of cytokine signaling are among such tools [17, 18]. Oligonucleotide aptamers belong to another class of biomolecules that selectively recognize a target and are currently being considered

as a potential alternative to antibodies in developing targeted therapeutics. The advantages of aptamers over antibodies include reproducible chemical synthesis and stable key characteristics, as well as the feasibility of making additional chemical modifications in order to control the lifetime of an aptamer in the body while maintaining its affinity for the target molecule [19, 20]. Importantly, aptamers are nucleic acids by their nature, so their functional activity can be further regulated using a complementary nucleotide antidote [21, 22]. Such a set of properties kindles interest in using aptamers to suppress the activity of soluble serum proteins, including inflammation-associated ones [23, 24].

The present study analyzed the features of the development of LPS-induced ALI in mice and the feasibility of suppressing it using the aptamer targeting the proinflammatory cytokine TNF-α. It was demonstrated that TNF-α is a pivotal player in the development of ALI, and that intranasal administration of an aptamer targeting TNF-α, conjugated with 40 kDa polyethylene glycol (PEG-aptTNF-α), to mice with ALI suppresses the development of an inflammation in the respiratory system of experimental animals.

EXPERIMENTAL

Synthesis of a TNF-α-targeting DNA aptamer and control oligonucleotide

Table 1 lists the nucleotide sequences of the oligodeoxyribonucleotides used in this study. A control random-sequence non-aptameric oligonucleotide was generated on the basis of aptTNF-α DNA aptamer using the service (https://www.genscript.com/tools/create-scrambled-sequence).

The oligonucleotides were synthesized using the solid-phase phosphoramidite method at a scale of 0.4 μmol on an automated ASM-800 DNA/RNA synthesizer (Biosset, Russia) according to the protocol optimized for this setup using β-cyanoethyl-N,N-diisopropyl phosphoramidites of 5'-N-protected 2'-deoxyribonucleosides (Glen Research, USA). CPG (controlled pore glass) particles (pore diameter, 500 Å) with 3'-O-dimethoxytrityltimidine attached via the 5'-hydroxyl group (Glen Research) were used as a polymeric carrier. The oligonucleotides containing an aminohexanol residue at the 5' end were synthesized using a commercially available modifier, 6-(trifluoroacetylamino)-hexyl-(2-cyanoethyl)-(N,N-diisopropyl)-phosphoramidite (Glen Research). After the synthesis, the oligonucleotides were separated from the carrier; the protecting groups were removed by 15-min exposure to a 40% aqueous methylamine solution (300 μL) at 65°C. Fully unblocked oligonucleotides were purified by preparative electrophoresis in a 15% denaturing polyacrylamide gel (PAAG).

Synthesis of conjugates with 40 kDa polyethylene glycol

To synthesize PEGylated conjugates, a 1 μmol solution of N-hydroxysuccinimide ester of 40 kDa linear polyethylene glycol (PEG) (Sigma-Aldrich, USA) in dimethylformamide (Sigma-Aldrich) was added to a solution of 5'-amino-modified oligonucleotide (0.1 μmol) in 0.1 M tetraborate buffer (pH 9.5). The reaction mixture was incubated under stirring at 25°C during 16 h. Excess reagents were removed from the resulting conjugates by electrophoresis in denaturing 12% PAAG, followed by elution with water and concentration using Amicon 10K ultracentrifuge modules (Merck, USA). Before being administered to the animals, the purified conjugates were sterilized by passage through a filter (pore diameter, 0.22 μm).

Laboratory animals

We used 6- to 8-week-old female Balb/C mice bred in the vivarium of the Institute of Chemical Biology and Fundamental Medicine SB RAS (Novosibirsk,

Table 1. TNF-α-targeting DNA aptamer, non-aptameric scrambled oligodeoxyribonucleotide and their conjugates with PEG

Aptamer	Nucleotide sequence, 5'-3'
PEG-aptTNF-α	PEG-NH_2-$(CH_2)_6$-GCG CCA CTA CAG GGG AGC TGC CAT TCG AAT AGG TGG GCC GCT$_{inv}$
aptTNF-α	NH_2-$(CH_2)_6$-GCG CCA CTA CAG GGG AGC TGC CAT TCG AAT AGG TGG GCC GCT$_{inv}$
PEG-Scr	PEG-NH_2-$(CH_2)_6$-AGA GGC GGT ATG ACC AGG CTA ATC GGC CGA GCC TCC GTG CGT$_{inv}$
Scr	NH_2-$(CH_2)_6$-AGA GGC GGT ATG ACC AGG CTA ATC GGC CGA GCC TCC GTG CGT$_{inv}$

PEG – 40 kDa polyethylene glycol residue; T_{inv} – 3'-terminal residue of thymidine linked to the adjacent nucleotide with a 3'–3' phosphodiester bond.

Russia). The animals were housed in a well-lit room (six animals per cage). The mice had free access to food and water. All the manipulations with the animals were performed in accordance with the guidelines for proper use and care of laboratory animals (EU Directive 2010/63/EC). The animal experiments were approved by the Interinstitutional Bioethics Commission of the Institute of Cytology and Genetics SB RAS (Novosibirsk, Russia) (Protocol No. 56 dated August 10, 2019).

LPS-induced acute lung injury

Acute lung injury (ALI) was induced in mice by intranasal (i.n.) administration of LPS (055:B5, Sigma-Aldrich) at a dose of 10 μg/mouse under isoflurane anesthesia. In the experiment aiming to study the dynamics of inflammatory changes in the respiratory system, the mice were withdrawn from the experiment 6, 16, and 24 h after induction; bronchoalveolar lavage fluid (BALF), blood serum, and lung tissue samples were collected for further analysis. In the experiment focusing on the anti-inflammatory activity of the TNF-α-targeting aptamers, the aptTNF-α aptamer at a dose of 1 mg/kg or its conjugate PEG-aptTNF-α at doses of 1 and 5 mg/kg were administered to mice 1 h after i.n. induction of ALI. Mice with ALI, untreated and receiving the respective scrambled oligonucleotides (Scr at a dose of 1 mg/kg and PEG-Scr at doses of 1 and 5 mg/kg), were used as controls. All the agents were administered intranasally in 50 μL of saline under isoflurane anesthesia. The mice were withdrawn from the experiment 24 h after ALI induction, and biomaterial (BALF and lung tissue) samples were collected for further analysis. Each group consisted of six mice.

Analysis of the bronchoalveolar lavage fluid

The lungs of the mice in the control and experimental groups were washed with 1 mL of a cold saline solution. The collected BALF samples were centrifuged at 1500 rpm at 4°C during 10 min; the supernatant was collected to conduct an enzyme-linked immunosorbent assay (ELISA). The cell pellet was resuspended in 50 μL of saline; the total leukocyte count ($\times 10^5$ cells/mL) was determined in a Neubauer chamber after 1 : 20 dilution with Türk's solution.

Assessment of the levels of proinflammatory cytokines by ELISA

The levels of the proinflammatory cytokines TNF-α and IL-6 in the BALF samples were quantified using ELISA kits (#BMS607-3 and #KMC0061, Thermo Fisher Scientific, USA) in compliance with the manufacturer's instructions. Absorbance at 450 nm was measured on a Multiscan RC spectrophotometer (Thermo Labsystems, Finland).

Assessment of the cytokine profile

The levels of proinflammatory cytokines and chemokines in the BALF samples were assessed using the LEGENDplex™ Mouse Inflammation Panel (13-plex) (Biolegend, USA) in compliance with the manufacturer's instructions on a NovoCyte 3000 flow cytometer (ACEA Bioscience, USA). The data were analyzed using the Legendplex online software.

Histology

Lung tissue was fixed in 10% buffered formalin, dehydrated in ethanol and xylene solutions of ascending concentration, and embedded into HISTOMIX paraffin. Paraffin sections up to 5 μm thick were cut on a Microm HM 355S microtome and stained with hematoxylin and eosin. All histologic specimens were examined and scanned using an Axiostar Plus microscope equipped with an AxioCam MRc5 digital camera (200× magnification).

The intensity of inflammatory changes in the lungs was assessed semi-quantitatively using the following scale: 0 – no pathological changes; 1 – mild inflammation; 2 – moderate inflammation; and 3 – severe inflammation. A total of five visual fields were analyzed for each sample (30 visual fields in each group).

Quantification of gene expression levels by real-time RT-PCR

The mRNA levels of the *Usp18*, *Traf1*, *Tnfaip3*, and *Hprt* genes in lung tissue were determined by quantitative real-time reverse transcription polymerase chain reaction (RT-PCR). Total RNA was isolated from the lungs of the experimental animals using the TRIzol reagent according to the manufacturer's instructions after pre-homogenization (FastPrep-24TM 5G homogenizer equipped with a QuickPrep 24 adapter, MP Biomedicals, USA). cDNA was synthesized using RT buffer and M-MuLV-RH revertase (Biolabmix, Russia) according to the manufacturer's instructions. Real-time RT-PCR was carried out using the HS-qPCR master mix (×2) (Biolabmix) according to the manufacturer's instructions. Amplification was performed under the following temperature conditions: (1) 94°C, 5 min; (2) 94°C, 10 s; and (3) 60°C, 30 s (50 cycles) on a C1000 Touch amplifier with a CFX96 module (Bio-Rad, USA). Data were processed using the BioRad CFX Manager software. *Table 2* lists the sequences of oligonucleotides used as primers. The relative gene expression level was normalized to the level of *Hprt* expression using the ΔΔCt method.

Table 2. Specific primers for real-time RT-PCR

Gene	Primer type	Nucleotide sequence
Usp18	Forward	5'- GCCCTCATGGTCTGGTTG-3'
	Probe	5'-((5,6)-FAM)-ACGTGTTGCCTTAACTCCTTGCTTCA-BHQ1-3'
	Reverse	5'- CACTTCTCTTCCTCTCTTCTGC-3'
Traf1	Forward	5'- AGATCACCAATGTCACCAAGC-3'
	Probe	5'-((5,6)-FAM)-ACTGTCAGCCTCTTCTCTCCAGCTT-BHQ1-3'
	Reverse	5'- CATCCCCGTTCAGGTACAAG-3'
Tnfaip3	Forward	5'- AGCCAGCACTTTGTACCC-3'
	Probe	5'-((5,6)-FAM)-AGTCTTCAAACCTACCCCGGTCTCT-BHQ1-3'
	Reverse	5'- GCTTTTCCTTCATCTCATTCTCAG-5'
Hprt	Forward	5'-CCCCAAAATGGTTAAGGTTGC-3'
	Probe	5'- ((5,6)-ROX)-CTTGCTGGTGAAAAGGACCT-3'-BHQ2
	Reverse	5'-AACAAAGTCTGGCCTGTATCC-3'

Statistical analysis

Statistical analysis was conducted using the two-tailed unpaired Student's t-test in the Microsoft Excel software. The $p \leqslant 0.05$ values were considered statistically significant. Data are presented as the mean value ± standard deviation.

RESULTS

The cytokine profile and the dynamics of inflammatory changes in the respiratory system of mice with LPS-induced acute lung injury

For assessing the cytokine level and the intensity of the respiratory system inflammation, acute lung injury (ALI) was induced in mice by intranasal (i.n.) administration of LPS (10 μg/mouse), followed by the sampling of material 6, 16, and 24 h after induction (*Fig. 1A*). As early as 6 h after LPS administration, the TNF-α level in the bronchoalveolar lavage fluid (BALF) had increased 21-fold compared with that in the healthy animals and was 3.4 ng/mL, remaining approximately unchanged until 24 h after ALI induction. The IL-6 levels had also increased to 2 ng/mL 6 h after LPS administration and then gradually decreased to 1.3 ng/mL by the time point of 24 h post-induction, being manifold higher than the IL-6 levels in the healthy animals (*Fig. 1B*, left panel). Assessment of the total leukocyte count in BALF showed that the maximum value of this parameter was observed 24 h post-induction: LPS administration increased leukocyte count 8.6-fold compared with that in the healthy animals (*Fig. 1B*, middle panel). Extremely low levels of TNF-α and IL-6 were detected in the serum samples of mice with ALI at all time points, being comparable to those in the healthy animals (*Fig. 1B*, right panel).

Identification of the cytokine profiles of BALF in mice with ALI over time by multiplex ELISA showed that i.n. administration of LPS significantly increased the levels of only two proinflammatory cytokines: TNF-α and IL-6. The TNF-α level remained high throughout the entire observation period, whereas the IL-6 level had declined already 16 h after ALI induction (*Fig. 1C*). The levels of other cytokines (IL-23, IL-1α, IFN-γ, MCP-1, IL-12p70, IL-1β, IL-10, IL-27, IL-17A, IFN-β, and GM-CSF) remained unchanged.

Histological analysis of the lung tissue samples from mice with ALI showed that LPS administration induced pathological changes in the respiratory system manifesting themselves as inflammatory granulocyte infiltration, destructive (desquamation of alveolar lining) and dyscirculatory (congestion, edema and hemorrhage) disorders (*Fig. 1D*). The severity of these changes varied at different time points throughout the observation period: changes associated with circulatory disturbances were prevailing 6 h after ALI induction; after 16 h, there appeared initial signs of cell migration to the inflammation site; whereas by 24 h after ALI induction, inflammatory infiltration in the lung tissue had fully taken hold, mainly being located around vessels and bronchi (*Fig. 1D*).

Hence, assessing the dynamics of inflammatory changes and the cytokine profile in mice with ALI showed that the TNF-α level remained steadily high throughout the entire observation period, thus indicating that this cytokine plays a crucial role in the signaling pathways of the inflammatory response. The LPS-induced morphological signs of inflammation in

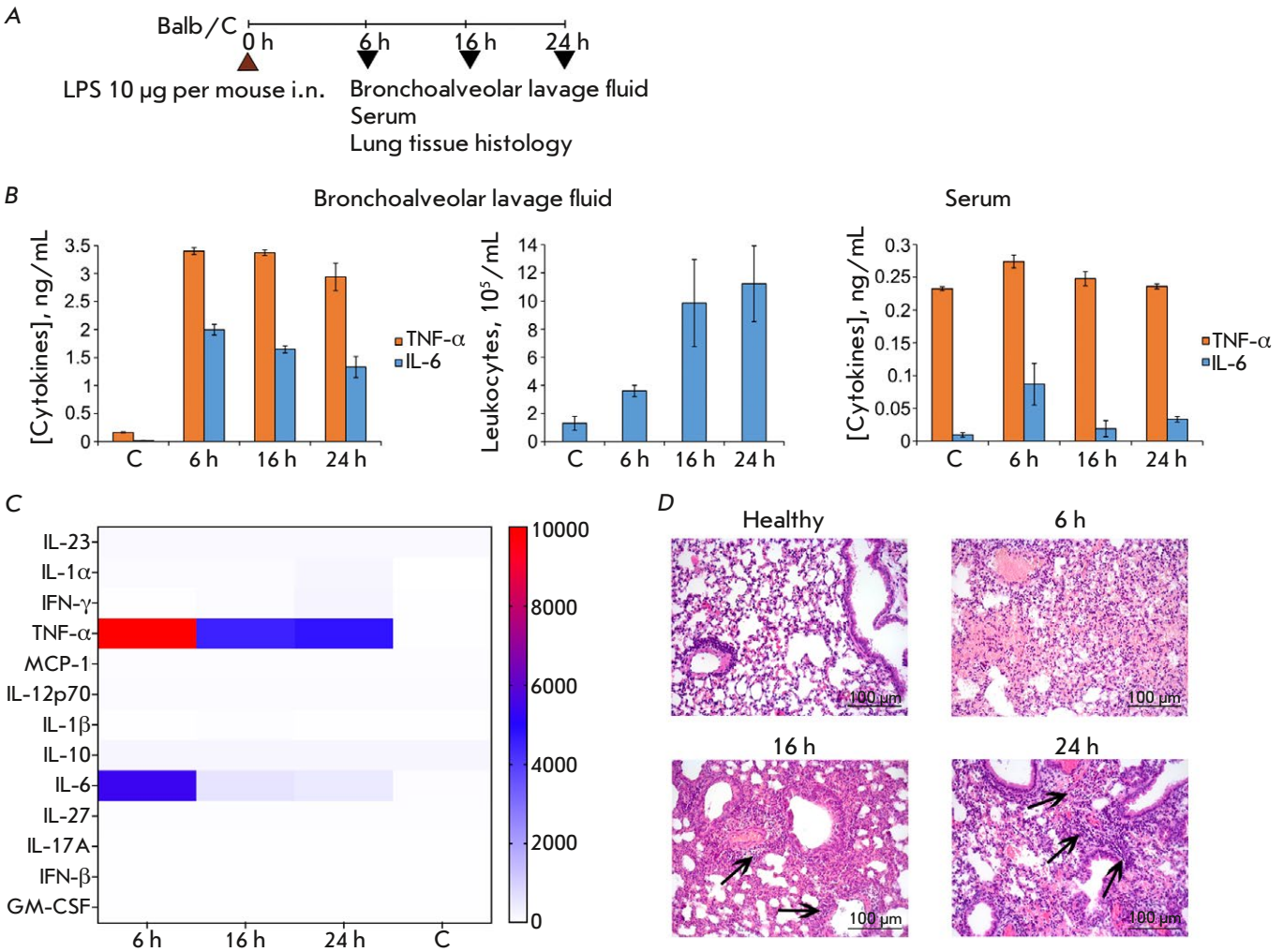

Fig. 1. The cytokine profile and inflammatory changes in the respiratory system of mice with LPS-induced acute lung injury over time. (*A*) Experimental design. Acute lung injury (ALI) was induced in Balb/C mice by intranasal (i.n.) administration of LPS (10 μg/mouse). Material was collected 6, 16, and 24 h after induction. (*B*) The levels of proinflammatory cytokines (TNF-α and IL-6) and the total leukocyte count in BALF, as well as serum levels of TNF-α and IL-6 in ALI mice 6, 16, and 24 h after induction. (*C*) The cytokine profile of BALF of ALI mice over time, assessed using multiplex ELISA. Data are presented as pg/mL. (*D*) Histological analysis of the lung tissue of ALI mice 6, 16, and 24 h after induction. Hematoxylin and eosin staining, original magnification 200×. Black arrows indicate inflammatory infiltration. C – control (healthy animals)

the respiratory system of mice were most intense 24 h after induction, making this time interval optimal for assessing the anti-inflammatory activity of the tested constructs.

The choice and synthesis of the anti-TNF-α DNA aptamer

Several nucleotide sequences of RNA and DNA aptamers capable of specifically binding TNF-α have been reported [25]. Most of them have affinity for the target protein in the nanomolar range and can inhibit the functional activity of TNF-α *in vitro*. The aptTNF-α DNA aptamer, which had been earlier shown to be able to suppress the development of inflammation in *in vivo* models of acute lung and liver injury when administered intravenously or intratracheally, was chosen for the study [26]. The total length of this aptameric oligonucleotide is 41 nucleotides, which makes its chemical synthesis rather fast and economically sound (the sequence of aptTNF-α is listed in *Table 1*). A scrambled oligonucleotide having the same length and nucleotide composition was used as

a similar non-aptameric DNA to control the specificity of aptamer activity. The *in vivo* anti-inflammatory activity of bivalent aptamers in which two aptamer modules are covalently linked by a 20 kDa polyethylene glycol residue has been demonstrated earlier [26]. In our study, we chose a different strategy to chemically modify the aptamer in order to increase its lifetime in the animal body and used modifications that are currently almost the "gold standard" for aptamers intended for use in *in vivo* experiments or clinical trials [27, 28]. An additional thymidine residue linked by the 3'–3' phosphodiester bond was inserted into the 3' end to prevent exonuclease hydrolysis; the commercially available polymer-bound 3'-O-dimethoxytritylthymidine was used in solid-phase oligonucleotide synthesis for this purpose, and 40 kDa polyethylene glycol (PEG) was inserted at the 5' end to improve the pharmacokinetic characteristics of the aptamer being topically delivered into the respiratory system of mice.

Therefore, the proposed aptamer variant ensures better synthesis control and isolation of the PEGylated conjugate, since at the detected TNF-α levels in BALF (⩽ 4 ng/mL), this protein is most likely to exist in a monomeric form rather than a trimeric one [29]. A similar set of modifications was also used for the control non-aptameric oligonucleotide.

Anti-inflammatory activity of the TNF-α-targeting aptamer in the model of LPS-induced acute lung injury

The anti-inflammatory activity of TNF-α-targeting aptamers (aptTNF-α and PEG-aptTNF-α) was studied in the model of LPS-induced ALI. Aptamers were administered intranasally (i.n.) to mice, since high levels of this cytokine were specifically detected in BALF. Respective scrambled oligonucleotides (Scr or PEG-Scr) were administered to mice in order to control the specificity of aptamer activity. The studied constructs were administered 1 h after ALI induction, followed by sampling of the material 24 h later (*Fig. 2A*), since it was the time point when morphological changes in the respiratory system of the mice were the most intense and complete.

Administration of LPS increased the total leukocyte count in the BALF of mice with ALI 7.7-fold compared to that in the healthy animals (*Fig. 2B*). Administration of aptTNF-α or the respective Scr had no effect on this parameter, whereas 5 mg/kg of the PEGylated aptamer PEG-aptTNF-α statistically significantly reduced the total leukocyte count in BALF 1.8-fold vs. control and 2.7-fold vs. PEG-Scr administered at the same dose (*Fig. 2B*). PEG-aptTNF-α administered at a dose of 1 mg/kg also caused a 1.5- and 1.8-fold drop in this parameter compared to that observed for the control and Scr, respectively. These differences (for the dose of 1 mg/kg) were statistically insignificant; however, they showed that the activity of PEG-aptTNF-α was dose-dependent. The TNF-α level in the BALF of mice with ALI was elevated 85-fold compared to that in the healthy animals, and administration of PEG-aptTNF-α had no significant effect on this parameter (*Fig. 2C*). The TNF-α level after administration of the non-PEGylated aptamer was not investigated, since it did not reduce the total leukocyte count in BALF as an indicator of the anti-inflammatory activity of the drug.

According to histological findings, administration of the constructs under study reduces the intensity of morphological manifestations of the LPS-induced ALI described previously in a dose-dependent manner. Administration of aptTNF-α and PEG-aptTNF-α at a dose of 1 mg/kg decreased the intensity of inflammatory changes in lung tissue 1.5- and 1.8-fold compared to that in the control group and 1.4- and 1.6-fold compared to the respective Scr (*Fig. 2D,E*). However, these differences were statistically significant only when comparing the aptamers and the controls. Administration of 5 mg/kg PEG-aptTNF-α led to a statistically significant decline in the inflammation intensity in the lung tissue compared both with the control group (2.2-fold) and the group receiving PEG-Scr (2-fold).

Hence, the PEG-aptTNF-α aptamer targeting pro-inflammatory TNF-α cytokine suppresses the development of LPS-induced inflammatory changes in the respiratory system of mice but does not normalize the parameters to the level of healthy animals. The anti-inflammatory activity of aptTNF-α/PEG-aptTNF-α is dose-dependent, which is most likely related to the fact that TNF-α binding increases with the preparation dose, while the anti-inflammatory effect was reliably demonstrated only for the conjugate with PEG, due to the improved pharmacokinetic characteristics of the agent.

Analysis of the expression levels of TNF-α-regulated genes in the lung tissue of mice with LPS-induced acute lung injury without treatment and after administration of the TNF-α-targeting aptamer

The next stage of our study involved a search for and assessment of the expression levels of potential TNF-α-regulated genes upon the development of LPS-induced ALI and its correction with the TNF-α-targeting aptamer to seek confirmation that the constructs used affect the ability of the secreted target protein to bind to its receptor and activate sig-

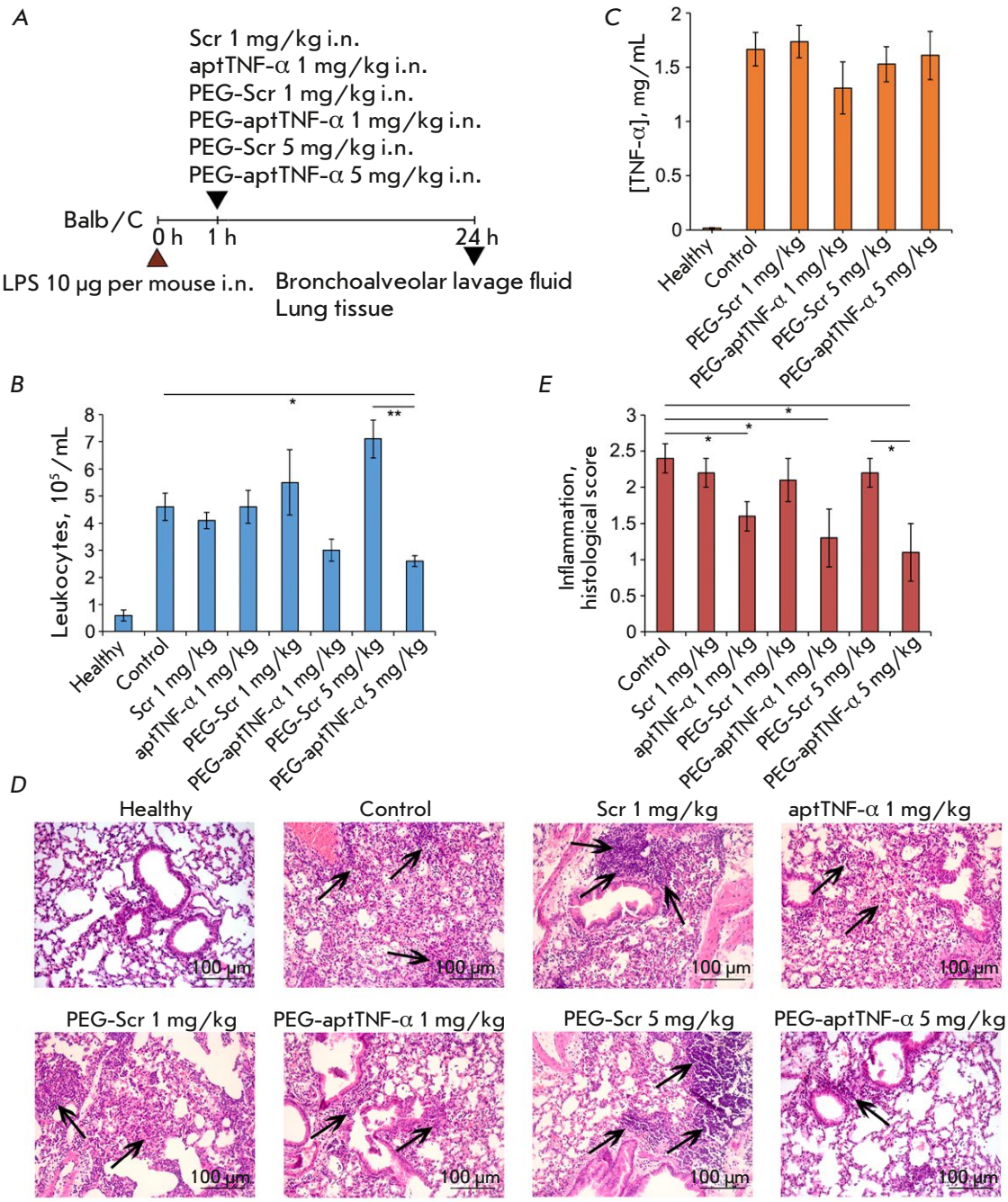

Fig. 2. The effect of TNF-α-targeting aptamers on the development of LPS-induced acute lung injury in mice. (*A*) Experimental design. Acute lung injury (ALI) was induced in Balb/C mice by intranasal (i.n.) administration of LPS (10 μg/mouse). Mice were administered i.n. TNF-α-targeting aptamers: aptTNF-α at a dose of 1 mg/kg and PEG-aptTNF-α at doses of 1 and 5 mg/kg 1 h after induction. Mice with ALI without treatment and treated with the scrambled oligonucleotide (Scr and PEG-Scr) were used as controls. Mice were sacrificed 24 h after induction, and material was collected for subsequent analysis. (*B*, *C*) The total number of leukocytes (*B*) and TNF-α level (*C*) in the bronchoalveolar lavage fluid (BALF) of mice with LPS-induced ALI without treatment and after administration of TNF-α-targeting aptamers. (*D*, *E*) Histological examination (*D*) and semi-quantitative assessment of the intensity of the inflammatory changes (*E*) in the lungs of mice in the control and experimental groups. Hematoxylin and eosin staining, original magnification 200×. Black arrows indicate inflammatory infiltration. The following scale was used to assess inflammation in the lungs: 0 – no pathological changes; 1 – mild inflammation; 2 – moderate inflammation; and 3 – severe inflammatory changes. Data are presented as the mean ± standard deviation; $^{*}p < 0.05$, $^{**}p < 0.01$

naling. The genes (namely, *Usp18*, *Traf1,* and *Tnfaip3*) were chosen based on the published data according to which their expression levels are upregulated by TNF-α in a broad range of biological and pathological processes, such as LPS-induced sepsis [30], myocardial ischemia reperfusion injury [31], cerebral ischemia [32], activation of the NF-ϰB and type I interferon-mediated signaling pathways [33–36], as well as hematopoiesis and regeneration of the myeloid lineage [37].

The expression levels of the *Usp18*, *Traf1*, and *Tnfaip3* genes in the lung tissue of mice were assessed by RT-PCR (*Fig. 3*). The lungs of healthy animals were characterized by low expression levels of the genes under study (assumed equal to unity (1)), whereas administration of LPS significantly increased their expression levels (control): *Usp18*, sevenfold; *Traf1*, twofold; and *Tnfaip3*, 61-fold compared to those in healthy animals.

The following patterns were revealed when assessing the effect of aptamers on the expression of the studied genes in the lung tissue of mice with ALI. Administration of PEG-aptTNF-α at a dose of 1 mg/kg led to a statistically significant decline in the *Usp18* gene expression level to a level typical of healthy animals: 5.9-fold vs. control and 2.6-fold vs. PEG-Scr. PEG-aptTNF-α administered at a dose of 5 mg/kg also resulted in a 2.6- and 3-fold decrease in the *Usp18* expression level compared to the control and PEG-Scr groups, respectively. However, statistically significant differences were revealed only between the aptamer and scrambled oligonucleotide (*Fig. 3*). Administration of PEG-aptTNF-α at doses of 1 and 5 mg/kg caused a 3.5- and 2.6-fold decrease in *Traf1* gene expression compared with the control and 1.8- and 1.7-fold decrease compared with PEG-Scr, respectively. However, no statistically significant differences in the effects of PEG-aptTNF-α and PEG-Scr at a dose of 5 mg/kg were observed (*Fig. 3*). For the *Tnfaip3* gene, the only statistically significant difference was the 1.6-fold decrease in the expression level upon exposure to 1 mg/kg PEG-aptTNF-α vs. the PEG-Scr group (*Fig. 3*). Administration of PEG-Scr at doses of 1 and 5 mg/kg had no statistically significant effect on the expression of all the studied genes. Administration of 1 mg/kg aptTNF-α resulted in a statistically insignificant 1.7- to 2.4-fold decline in the expression levels of the *Usp18* and *Traf1* genes and a 1.3-fold increase in expression vs. the control group in the case of the *Tnfaip3* gene (*Fig. 3*).

Hence, the most prominent decline in the expression levels of potential target genes was observed when administering 1 mg/kg PEG-aptTNF-α, whereas significant anti-inflammatory effects were detected when this aptamer was administered at a dose of 5 mg/kg, which may be related to the choice of time points to quantify the expression levels of these genes, when the maximum effect of a higher aptamer dose on the expression of TNF-α-associated genes has already passed.

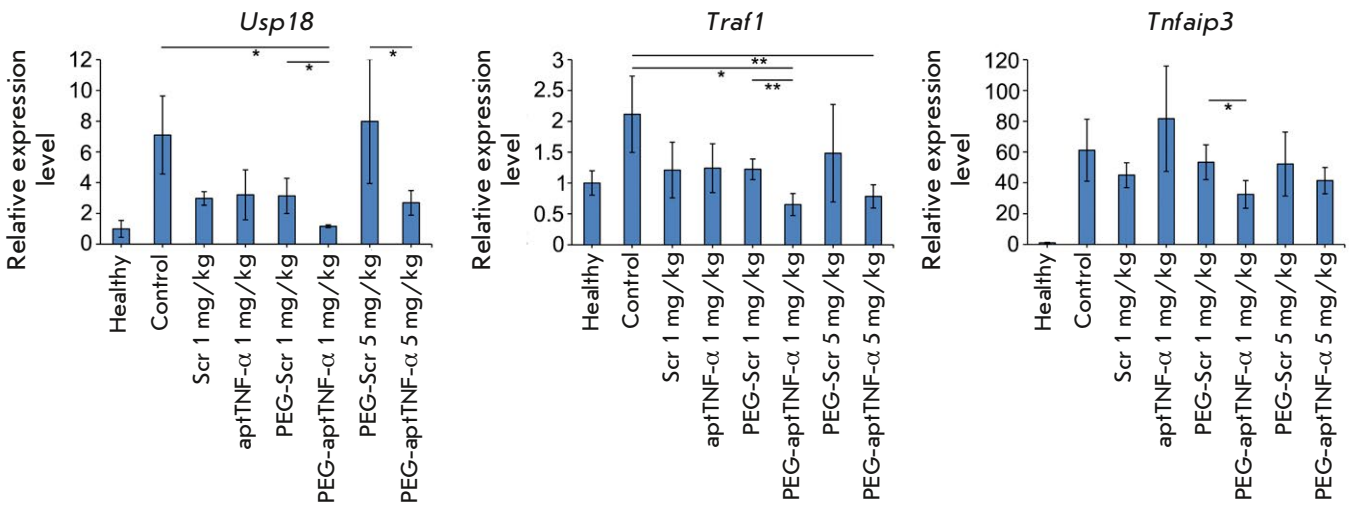

Fig. 3. The expression levels of potential target genes of TNF-α (*Usp18*, *Traf1*, and *Thfaip3*) in the lung tissue of mice with LPS-induced acute lung injury without treatment and after administration of aptamers. Gene expression levels were normalized to the expression level of *Hprt*, which was used as an internal standard. Three samples from each group were analyzed in triplicate. Data are presented as the mean ± standard deviation; $^{*}p < 0.05$, $^{**}p < 0.01$

DISCUSSION

TNF-α, a pleiotropic cytokine produced by activated macrophages, T cells, and natural killer cells, is among the most important immune response regulators; therefore, affecting the level of this cytokine can be an efficient strategy for correcting immune disorders associated with cancer, as well as inflammatory, metabolic, and infectious diseases [38, 39]. Taking into account the variety of diseases and biological processes involving TNF-α, several dozen genes and signaling pathways regulate TNF-α and are regulated by it [40, 41].

Today, monoclonal antibodies are the key anti-TNF-α drugs approved for clinical use; however, they cause adverse events such as increased susceptibility to infections, as well as the development of demyelinating diseases and malignancies [41]. Anti-TNF-α agents of a different nature, such as aptamers, may possibly reduce the rate and severity of complications.

In this study, the anti-inflammatory activity of the TNF-α-targeting aptamer, as well as the effect of chemical modifications on its effectiveness, was studied in the mouse model of LPS-induced ALI. The choice of the aptamer administration route was justified and verified by the cytokine profile data in BALF and serum samples upon development of ALI in mice over time. The TNF-α level in BALF was shown to be significantly higher than that in serum, thus indicating that topical intranasal administration of the aptamer is more promising compared to its systemic administration. As for the aptamer doses used in the experiment, we chose concentrations that were likely to ensure the target effect taking into account that PEGylated aptamer concentrations in the range of 1–10 mg/kg are optimal for *in vivo* experiments and clinical studies [42].

PEG-aptTNF-α was found to exhibit a stronger anti-inflammatory effect than its unmodified analog, which may be due to its longer lifetime in the animal body. PEG-aptTNF-α was dose-dependent: at a dose of 5 mg/kg, its effectiveness was higher compared to a dose of 1 mg/kg. However, despite the anti-inflammatory activity observed in BALF and lung tissue, no significant decline in the TNF-α level was detected in BALF. This discrepancy can result from the fact that the aptamer and anti-TNF-α antibodies used in ELISA may bind to different spatially distant epitopes of TNF-α, interaction with the aptamer having no effect on antibody binding. However, while no data obtained in structural or molecular modeling studies are available that would indicate to which particular TNF-α epitope anti-TNF-α aptamer binds, this hypothesis requires further verification.

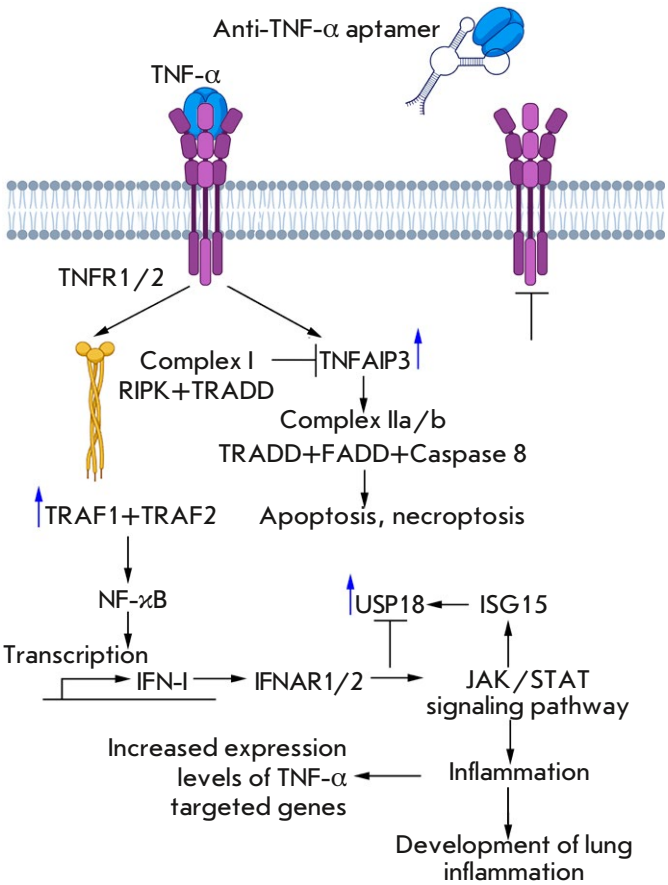

Fig. 4. The general scheme of TNF-α signaling

Since direct measurements of the TNF-α level failed to yield the anticipated results, we decided to assess the effect of the TNF-α-targeting aptamer by analyzing the mRNA expression level of the genes involved in the regulation and transduction of TNF-α signaling. Genes directly involved in the TNF-α regulatory pathway, whose expression level increases during the development of ALI, were chosen as potential TNF-α-regulated genes.

In the early phase of signaling, the soluble form of TNF-α binds to the tumor necrosis factor receptor 1 (TNFR1), causing receptor trimerization and involvement of the TNFR1-associated death domain protein (TRADD) and receptor-interacting serine/threonine protein kinase 1 (RIPK1) (*Fig. 4*). Next, TRADD interacts with the TRAF1/TRAF2 heterodimer to form complex I, which activates the NF-κB signaling pathway and induces the synthesis of proinflammatory cytokines, including IFN-I [33]. Through IFNAR1/2 receptors and the JAK/STAT signaling pathway, IFN-I has a further impact on the next important component of the development of the inflammato-

ry response: the ISG15/USP18 axis, which regulates the activity of the immune system [36] and reduces the inflammatory response intensity by inhibiting the JAK/STAT signaling pathway, indicating that there possibly exists a negative feedback loop between USP18, IFN-I, and, therefore, TNF-α [43, 44].

TNF-α-induced protein 3 (TNFAIP3), also known as A20, is another key molecule in the mechanism of reverse regulation. The basal level of TNFAIP3 expression is low in most cells but increases rapidly as the inflammatory response develops [45]. TNFAIP3 is recruited to the TNFR1 signaling complex, where it deubiquitinates RIPK1, thus resulting in a loss of stability by complex I and inhibits further activation of NF-κB. TRADD dissociated from complex I forms complexes with the Fas-associated death domain protein (FADD) and caspase 8 (complex IIa) or with RIPK1, FADD, and caspase 8 (complex IIb), which further leads to apoptosis or necroptosis [46].

Taking into account the involvement of the aforementioned genes in TNF-α signaling and regulation, as expected, administration of the TNF-α-targeting aptamer reduced the expression level of the target genes chosen for validation (namely, *Traf1* as a component of the heterodimeric complex, which is directly involved in TNF-α signal transduction; *Tnfaip3*, which inhibits the activation of the proinflammatory NF-κB signaling pathway; and *Usp18*, which regulates the intensity of the inflammatory response after NF-κB activation via the negative feedback mechanism), suggesting that it is reasonable to use TNF-α-regulated genes to assess the biological activity of the anti-TNF-α aptamer. Similar to the case with morphological changes in the respiratory system of mice, PEG-aptTNF-α exhibited a stronger effect on gene expression levels than unmodified aptamers did.

Hence, this study once again demonstrated the importance of TNF-α as a therapeutic target in ALI, as well as the benefits of using chemically modified aptamers to suppress its function. A secretory protein is a very attractive target for an aptamer, since the agent does not need to be delivered into the cell for binding to it; instead, a therapeutic aptamer can be systemically or locally administered to organs and tissues where target protein levels are elevated. Furthermore, it is very encouraging that the aptamer can be administered after the onset of the pathology and that its activity can be inhibited with an antidote, which makes therapeutic aptamers almost "ideal drugs."

CONCLUSIONS

It has been found in this study that TNF-α is among the pivotal players in cytokine signaling during the development of LPS-induced ALI and that intranasal administration of anti-TNF-α aptamers efficiently mitigates the LPS-induced inflammatory changes in the respiratory system of mice, affects the TNF-α-regulated genes, and can be viewed as a tool for treating ALI of different etiologies and other pulmonary diseases accompanied by immune disorders. ●

This work was supported by the Russian Science Foundation (grant No. 19-74-30011) and the Russian state-funded project for ICBFM SB RAS (grant No. 121031300042-1).

REFERENCES

1. Mowery N.T., Terzian W.T.H., Nelson A.C. // Curr. Probl. Surg. 2020. V. 57. № 5. P. 100777.
2. Chen X., Tang J., Shuai W., Meng J., Feng J., Han Z. // Inflamm. Res. 2020. V. 69. № 9. P. 883–895.
3. Lucas R., Hadizamani Y., Gonzales J., Gorshkov B., Bodmer T., Berthiaume Y., Moehrlen U., Lode H., Huwer H., Hudel M., et al. // Toxins (Basel). 2020. V. 12. № 4. P. 223.
4. Shah R.D., Wunderink R.G. // Clin. Chest Med. 2017. V. 38. № 1. P. 113.
5. Goligher E.C., Douflé G., Fan E. // Am. J. Respir. Crit. Care Med. 2015. V. 191. № 12. P. 1367–1373.
6. Agrawal D.K., Smith B.J., Sottile P.D., Albers D.J. // Front. Physiol. 2021. V. 12.
7. Pauluhn J. // Toxicology. 2021. V. 450.
8. Laskin D.L., Malaviya R., Laskin J.D. // Toxicol. Sci. 2019. V. 168. № 2. P. 287–301.
9. Zhang C.N., Li F.J., Zhao Z.L., Zhang J.N. // Am. J. Physiol. - Lung Cell. Mol. Physiol. 2021. V. 321. № 5. P. 885–891.
10. Sever I.H., Ozkul B., Erisik Tanriover D., Ozkul O., Elgormus C.S., Gur S.G., Sogut I., Uyanikgil Y., Cetin E.O., Erbas O. // Exp. Lung Res. 2021. P. 1–10.
11. Jiao Y., Zhang T., Zhang C., Ji H., Tong X., Xia R., Wang W., Ma Z., Shi X. // Crit. Care. 2021. V. 25. № 1. P. 356.
12. Kong L., Deng J., Zhou X., Cai B., Zhang B., Chen X., Chen Z., Wang W. // Cell Death Dis. 2021. V. 12. № 10. P. 928.
13. Jamal M., Bangash H.I., Habiba M., Lei Y., Xie T., Sun J., Wei Z., Hong Z., Shao L., Zhang Q. // Virulence. 2021. V. 12. № 1. P. 918–936.
14. Ramasamy S., Subbian S. // Clin. Microbiol. Rev. 2021. V. 34. № 3.
15. Dharra R., Kumar Sharma A., Datta S. // Cytokine. 2023. V. 169.
16. Gao Y., Zhou A., Chen K., Zhou X., Xu Y., Wu S., Ning X. // Chem. Sci. 2024. V. 15. № 6. P. 2243.
17. Attiq A., Yao L.J., Afzal S., Khan M.A. // Int. Immunopharmacol. 2021. V. 101. P. 108255.
18. Patel S., Saxena B., Mehta P. // Heliyon. 2021. V. 7. № 2.
19. Adachi T., Nakamura Y. // Mol. 2019, Vol. 24, Page 4229. 2019. V. 24. № 23. P. 4229.
20. Ji D., Feng H., Liew S.W., Kwok C.K. // Trends Biotech-

nol. 2023. V. 41. № 11. P. 1360–1384.
21. Stoll H., Steinle H., Wilhelm N., Hann L., Kunnakattu S.J., Narita M., Schlensak C., Wendel H.P., Avci-Adali M. // Molecules. 2017. V. 22. № 6. P. 954.
22. Yu H., Frederiksen J., Sullenger B.A. // RNA. 2023. V. 29. № 4. P. rna.079503.122.
23. Stephens M. // Pharmacol. Ther. 2022. V. 238. P. 108173.
24. Luo Z., Chen S., Zhou J., Wang C., Li K., Liu J., Tang Y., Wang L. // Front. Bioeng. Biotechnol. 2022. V. 10. P. 976960.
25. Shatunova E.A., Korolev M.A., Omelchenko V.O., Kurochkina Y.D., Davydova A.S., Venyaminova A.G., Vorobyeva M.A. // Biomedicines. 2020. V. 8. № 11. P. 1–44.
26. Lai W.Y., Wang J.W., Huang B.T., Lin E.P.Y., Yang P.C. // Theranostics. 2019. V. 9. № 6. P. 1741–1751.
27. Qi S., Duan N., Khan I.M., Dong X., Zhang Y., Wu S., Wang Z. // Biotechnol. Adv. 2022. V. 55. P. 107902.
28. Zhang Y., Zhang H., Chan D.W.H., Ma Y., Lu A., Yu S., Zhang B., Zhang G. // Front. Cell Dev. Biol. 2022. V. 10. P. 104–108.
29. Daub H., Traxler L., Ismajli F., Groitl B., Itzen A., Rant U. // Sci. Rep. 2020. V. 10. № 1.
30. Hu B., Ge C., Zhu C. // Int. Immunol. 2021. V. 33. № 9. P. 461–468.
31. Xu W., Zhang L., Zhang Y., Zhang K., Wu Y., Jin D. // J. Am. Heart Assoc. 2019. V. 8. № 21. P. e012575. doi: 10.1161/JAHA.119.012575.
32. Xiang J., Zhang X., Fu J., Wang H., Zhao Y. // Neuroscience. 2019. V. 419. P. 121–128.
33. Courtois G., Fauvarque M.O. // Biomed. 2018, Vol. 6, Page 43. 2018. V. 6. № 2. P. 43.
34. Catrysse L., Vereecke L., Beyaert R., van Loo G. // Trends Immunol. 2014. V. 35. № 1. P. 22–31.
35. MacParland S.A., Ma X.-Z., Chen L., Khattar R., Cherepanov V., Selzner M., Feld J.J., Selzner N., McGilvray I.D. // J. Virol. 2016. V. 90. № 12. P. 5549–5560.
36. Sarasin-Filipowicz M., Wang X., Yan M., Duong F.H.T., Poli V., Hilton D.J., Zhang D.-E., Heim M.H. // Mol. Cell. Biol. 2009. V. 29. № 17. P. 4841–4851.
37. Yamashita M., Passegué E. // Cell Stem Cell. 2019. V. 25. № 3. P. 357–372.
38. Savenkova D.A., Gudymo A.S., Korablev A.N., Taranov O.S., Bazovkina D. V., Danilchenko N. V., Perfilyeva O.N., Ivleva E.K., Moiseeva A.A., Bulanovich Y.A., et al. // Int. J. Mol. Sci. 2024. V. 25. № 2. P. 1156.
39. Wong M., Ziring D., Korin Y., Desai S., Kim S., Lin J., Gjertson D., Braun J., Reed E., Singh R.R. // Clin. Immunol. 2008. V. 126. № 2. P. 121–136.
40. Falvo J. V., Tsytsykova A. V., Goldfeld A.E. // Curr. Dir. Autoimmun. 2010. V. 11. № 1. P. 27–60.
41. Leone G.M., Mangano K., Petralia M.C., Nicoletti F., Fagone P. // J. Clin. Med. 2023, Vol. 12, Page 1630. 2023. V. 12. № 4. P. 1630.
42. Kovacevic K.D., Gilbert J.C., Jilma B. // Adv. Drug Deliv. Rev. 2018. V. 134. P. 36–50.
43. Malakhova O.A., Kim K. Il, Luo J.K., Zou W., Kumar K.G.S., Fuchs S.Y., Shuai K., Zhang D.E. // EMBO J. 2006. V. 25. № 11. P. 2358–2367.
44. François-Newton V., de Freitas Almeida G.M., Payelle-Brogard B., Monneron D., Pichard-Garcia L., Piehler J., Pellegrini S., Uzé G. // PLoS One. 2011. V. 6. № 7.
45. Devos M., Mogilenko D.A., Fleury S., Gilbert B., Becquart C., Quemener S., Dehondt H., Tougaard P., Staels B., Bachert C., et al. // J. Invest. Dermatol. 2019. V. 139. № 1. P. 135–145.
46. Martens A., van Loo G. // Cold Spring Harb. Perspect. Biol. 2020. V. 12. № 1. P. a036418. doi: 10.1101/cshperspect.a036418.

A Vector Nanoplatform for the Bioimaging of Deep-Seated Tumors

E. I. Shramova[1], S. M. Deyev[1–3], G. M. Proshkina[1*]
[1]Shemyakin-Ovchinnikov Institute of Bioorganic Chemistry, Moscow, Russian Academy of science, Moscow, 117997 Russian Federation
[2]Sechenov First Moscow State Medical University (Sechenov University), Moscow, 119991 Russian Federation
[3]National Research Centre "Kurchatov Institute", Moscow, 123098 Russian Federation
*E-mail: gmb@ibch.ru
Received May 12, 2024; in final form, May 16, 2024
DOI: 10.32607/actanaturae.27425

ABSTRACT **Today, in preclinical studies, optical bioimaging based on luminescence and fluorescence is indispensable in studying the development of neoplastic transformations, the proliferative activity of the tumor, its metastatic potential, as well as the therapeutic effect of antitumor agents. In order to expand the capabilities of optical imaging, sensors based on the bioluminescence resonance energy transfer (BRET) mechanism and, therefore, independent of an external light source are being developed. A targeted nanoplatform based on HER2-specific liposomes whose internal environment contains a genetically encoded BRET sensor was developed in this study to visualize deep-seated tumors characterized by overexpression of human epidermal growth factor receptor type 2 (HER2). The BRET sensor is a hybrid protein consisting of the highly catalytic luciferase NanoLuc (an energy donor) and a LSSmKate1 red fluorescent protein with a large Stokes shift (an energy acceptor). During the bioimaging of disseminated intraperitoneal tumors formed by HER2-positive SKOV3.ip1cells of serous ovarian cystadenocarcinoma, it was shown that the developed system is applicable in detecting deep-seated tumors of a certain molecular profile. The developed system can become an efficient platform for optimizing preclinical studies of novel targeted drugs.**
KEYWORDS **bioluminescence resonance energy transfer, DARPins, protein with a large Stokes shift LSSmKate1, epidermal growth factor receptor type 2 HER2, NanoLuc luciferase, molecular targeted bioimaging.**
ABBREVIATIONS **BRET – bioluminescence resonance energy transfer; DARPins – designed ankyrin repeat proteins; HER2 – human epidermal growth factor receptor 2; LSS protein – large Stokes shift protein.**

INTRODUCTION

Despite the tremendous progress achieved in cancer treatment thanks to early diagnosis and innovative therapies, cancer remains among the leading causes of death worldwide. Thus, according to the World Health Organization, the incidence of cancer in 2022 stood at 20 million new cases, almost 50% of which (9.7 million) ended in patient death (https://www.who.int/news/item/01-02-2024-global-cancer-burden-growing--amidst-mounting-need-for-services). Since metastatic spread is the main cause of death for cancer patients, it is important to develop novel model systems and technologies for preclinical studies that would allow one to assess both the tumor progression process and tumor response to therapy.

Current knowledge of the molecular foundations of oncogenesis, which makes tumor profiling (or typing) feasible, drives the development of targeted therapies selectively addressing particular molecular targets specific to a given cancer type or subtype: cell surface antigens, growth factors, receptors, or signal transduction pathways, which regulate the cell cycle, proliferation, metastatic spread, and angiogenesis.

Along with advances in tumor molecular profiling techniques, preclinical techniques of non-invasive targeted molecular imaging of tumors and metastases are undergoing intensive development in experimental oncology [1–3]. *In vivo* monitoring of the spread of cell populations exogenously introduced into a model organism is crucial for understanding oncogenesis as

well as assessing the therapeutic effect of antitumor agents in preclinical pharmacological research [2, 4].

Whole-body real-time optical bioimaging based on fluorescent and luminescent systems is an indispensable tool in modern preclinical studies [1, 3, 5].

Bioluminescence imaging is based on the detection of visible light emitted as a result of the oxidation of a specific substrate by luciferase [6]. In order to monitor tumor growth or regression, as well as assess the *in vivo* effectiveness of an antitumor drug, the luciferase gene is either constitutively or inducibly expressed in tumor cells that are further used to form the animal model of the cancer [7, 8]. Bioluminescence imaging is widely employed in preclinical studies, but the introduction of this method into clinical practice is being hindered by the fact that the cell line transfected with the luciferase gene needs to be the end product.

Fluorescence imaging allows one to visualize a tumor by detecting light generated by fluorescent proteins, quantum dots, or fluorescent dyes [1]. However, the need for an external light source in order to excite a fluorescent tag imposes significant limitations on the application of this method in detecting deep-seated tumors: as exciting light passes through tissues, its intensity drops abruptly because of diffraction, which reduces the spatial resolution of fluorescence images, as diffusion causes light scattering by tissues, as well as photon absorption by biological chromophores (melanin, hemoglobin, and oxyhemoglobin) [1, 9, 10].

The aforementioned limitations can be overcome using optical bioimaging methods based on the resonance energy transfer mechanism: bioluminescence resonance energy transfer (BRET) or fluorescence resonance energy transfer (FRET), which are increasingly employed in preclinical studies [11]. Although BRET and FRET systems rely on the same mechanism: (Förster resonance energy transfer from donor to acceptor) [12], BRET systems are preferred because the absence of autofluorescence and photobleaching associated with fluorophore excitation ensures increased detection sensitivity at the whole-body level.

The conventional BRET systems consist of luciferase, which acts as a resonance energy donor in the presence of its bioluminescent substrate, and an acceptor represented by a fluorescent protein, dye, or quantum dots. For optical bioimaging in animals to be efficient, a BRET system needs to possess such properties as high energy transfer from a donor to an acceptor and excellent spectral resolution; furthermore, it needs to contain an acceptor emitting in the red spectral region. The red and near-infrared spectral regions are predilected in imaging deep tissues and the whole body, as there is no light absorption by hemoglobin, melanin, and water in this spectral region.

Approximately two dozen high-sensitivity BRET systems have been developed [11]. They employ luciferase from coral *Renilla reniformis* (RLuc), the North American firefly *Photinus pyralis* (Fluc), and genetically engineered NanoLuc luciferase from the deep-sea shrimp *Oplophorus gracilirostris* as energy donors, as well as proteins of different colors, including those whose emission maximum lies in the red spectral region [13–19] as acceptors.

In all the aforementioned studies focusing on the development of BRET sensors based on fluorescent proteins, tumor models comprising genetically engineered cells that stably express the BRET sensor gene were used to monitor tumor cells in an animal body. In this study, we propose a different approach which involves detection of deep-seated tumors in an animal body using a BRET sensor exogenously introduced into the body and exhibiting tropicity for tumors with a given molecular profile.

We chose the tumor-associated antigen HER2 (human epidermal growth factor receptor type 2) as a target. It is known that 15–20% of human breast and ovarian tumors are characterized by an upregulated *HER2* expression [20, 21]. In modern medical practice, the HER2 tumor marker is a therapeutic target for monoclonal antibodies (Pertuzumab and Trastuzumab) and kinase inhibitors (Lapatinib) in patients with HER2-positive breast tumors [22].

In this study, we designed a platform for detecting HER2-positive tumors based on tumor-specific liposomes loaded with a genetically encoded BRET sensor (*Fig. 1*). The BRET sensor is NanoLuc-LSSmKate1, a hybrid protein based on the highly catalytic NanoLuc luciferase and the large Stokes shift red fluorescent protein LSSmKate1 ($\lambda_{ex}/\lambda_{em}$ = 463/624 nm) [23]. In the presence of a substrate, furimazine, NanoLuc luciferase acts as a source of endogenous bioluminescence, thus becoming an energy source for exciting the LSSmKate1 red fluorescent protein. The tropicity of liposomes for the HER2 antigen on the tumor cell surface is determined by the HER2-specific protein DARPin_9-29 [24]. The *in vivo* functionality of the developed system was demonstrated experimentally using the model of deep-seated disseminated tumors.

EXPERIMENTAL

Cloning the *NanoLuc-LSSmKate1* gene and production of the NanoLuc-LSSmKate1, NanoLuc, and DARPin_9-29 proteins

The nucleotide sequence encoding *LSSmKate1* was obtained by introducing K69Y/P131T/S148G/M167E/

T183S/M196V mutations into the *mKate2* coding sequence (plasmid pmKate2-N, Evrogen, Russia). The sequences encoding NanoLuc luciferase and the LSSmKate1 red fluorescent protein were then merged in one reading frame and cloned into the pET22b vector. A linker encoding the GGGGS polypeptide inserted between the coding sequences of the *NanoLuc* and *LSSmKate1* genes. The peptide linker ensured that the two functional domains (NanoLuc luciferase and the LSSmKate1 fluorescent module) in the hybrid protein were not sterically hindered, and that they were able to retain their functional properties while being brought closer together for efficient BRET.

The fidelity of the final construct was verified by sequencing. The coding sequence of the *NanoLuc-LSSmKate1* gene corresponds to a protein with the following primary structure: MVFTLEDFV GDWRQTAGYNLDQVLEQGGVSSLFQNLGVSVTPI QRIVLSGENGLKIDIHVIIPYEGLSGDQMGQIEKIF KVVYPVDDHHFKVILHYGTLVIDGVTPNMIDYFG RPYEGIAVFDGKKITVTGTLWNGNKIIDERLINPD GSLLFRVTINGVTGWRLCERILAGGGGSMVSELIK ENMHMKLYMEGTVNNHHFKCTSEGEGKPYEGTQ TMRIKVVEGGPLPFAFDILATSFMYGSYTFINHTQ GIPDFFKQSFPEGFTWERVTTYEDGGVLTATQDTS LQDGCLIYNVKIRGVNFTSNGPVMQKKTLGWEA GTEMLYPADGGLEGRSDEALKLVGGGHLICNLKS TYRSKKPAKNLKVPGVYYVDRRLERIKEADKETY VEQHEVAVARYCDLPSKLGHKLNAAALEHHHHHH.

The proteins (NanoLuc-LSSmKate1, NanoLuc, and DARPin_9-29) used in this study were produced by auto-induction [25]. *E. coli* BL21(DE3) colonies transformed with pET22-NanoLuc-LSSmKate1, pET22-NanoLuc, or pET22-DARP were cultured in a ZYM-5052 medium for autoinduction in the presence of ampicillin (100 μg/mL) at 25°C and 200 rpm overnight. The autoinduction medium containing equimolar concentrations of sodium hydrogen phosphate and potassium dihydrogen phosphate prevents acidification of the culture medium by bacterial metabolic products and ensures that neutral pH values are maintained even for high cell-density cultures (OD_{600} ~ 10). Balanced concentrations of glucose, lactose, and glycerol, as well as the high intensity of culture stirring (200 rpm), make it possible to automatically induce gene expression of the target protein (upon glucose depletion in the medium) without controlling the culture density. Biomass was precipitated by 15-min centrifugation at 6,000 *g*, resuspended in 20 mM NaPi, pH 8.0, 150 mM NaCl, and lysozyme (30 μg/mL). Cells were disrupted by ultrasonication; debris was removed by high-speed centrifugation (25,000 *g*). Imidazole was added to the clarified lysate to a final concentration of 30 mM. The lysate was filtered through a membrane (pore diameter, 0.2 μm) and applied onto a 1 mL HisTrap column (Cytiva). Proteins were isolated according to the manufacturer's protocol. Protein concentrations were determined spectrophotometrically according to the Beer–Lambert law using the following extinction coefficients: NanoLuc-LSSmKate1, λ_{280} = 54570 $M^{-1}cm^{-1}$; NanoLuc, ε_{280} = 25400 $M^{-1}cm^{-1}$; and DARPin, ε_{280} = 4470 $M^{-1}cm^{-1}$.

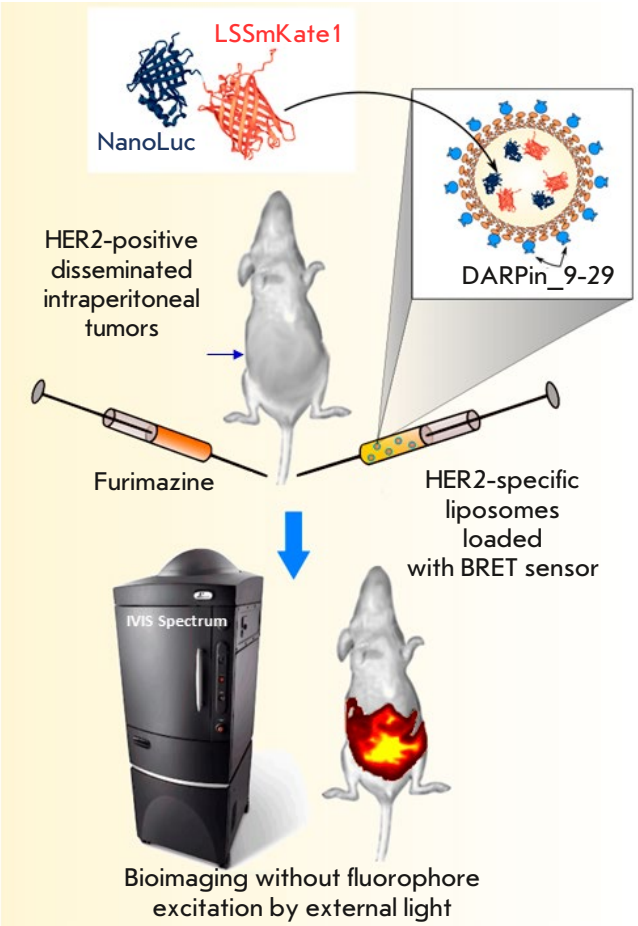

Fig. 1. Targeted nanoplatform based on the NanoLuc-LSSmKate1 BRET sensor and HER2-specific liposomes for the non-invasive diagnosis of deep-seated tumors. Conceptual scheme of the experiment: the genetically encoded NanoLuc-LSSmKate1 BRET sensor is incorporated into liposomes whose outer surface is modified with the DARPin_9-29 HER2-specific module. In the presence of a luciferase substrate in the animal body, the red fluorescent protein is activated without an external light source, allowing intravital real-time detection of deep-seated tumors in the animal body

Extinction coefficients were determined using the ProtParam tool software (https://web.expasy.org).

Quantification of BRET efficiency in the NanoLuc-LSSmKate1 system

The luminescence spectra of NanoLuc-LSSmKate1 and NanoLuc in the presence of 5 μM furimazine were recorded to evaluate BRET efficiency in the NanoLuc-LSSmKate1 system. The measurements were performed 10s after the addition of the luciferase substrate to an IVIS Spectrum CT system (PerkinElmer, USA) in the excitation block mode; the emission spectrum was recorded in the wavelength range of 500–740 nm with an increment of 20 nm. BRET efficiency was calculated as the ratio between the energies emitted by the acceptor (NanoLuc-LSSmKate1) and the donor (NanoLuc) [26, 27].

Production of HER2-specific liposomes loaded with NanoLuc-LSSmKate1

NanoLuc-LSSmKate1 was encapsulated into liposomes according to the procedure described in ref. [28]. A phospholipid suspension (0.3 mL, final concentration of 4 g/L) prepared from L-α-phosphatidylcholine pellets (Avanti Polar Lipids, Soy 40%) was mixed with 0.2 mL of NanoLuc-LSSmKate1 (final concentration, 150 μM in 20 mM NaPi, pH 6.0). Encapsulation was based on electrostatic interaction between the positively charged polyhistidine tag on the protein (pK_a of histidine's imidazole ~ 6) and the negatively charged inner liposome membrane at neutral pH. The suspension consisting of phospholipids and NanoLuc-LSSmKate1 was subjected to five cycles of rapid freezing (–150°C) and thawing (+30°C), followed by extrusion through a filter with 100-nm pores. The free protein and lipids were separated from the liposomes by gel permeation chromatography on a column packed with the Sepharose CL-2B sorbent.

The outer surface of the liposomes was functionalized with HER-2-specific DARPin_9-29 at the amino groups of phosphotidylethanolamine. For this purpose, the liposomes, loaded with NanoLuc-LSSmKate1, were incubated in the presence of a tenfold molar excess of sulfo-EMCS (N-ε-maleimidocaproyloxysul fosuccinimide ester). Simultaneously, DARPin_9-29 (100 μM in 20 mM NaPi, pH 7.5) was incubated with 2-iminothiolane (6 mM, Traut's reagent that allows for insertion of the SH group at primary amines of the protein). Both reactions were conducted at room temperature for 40 min; the products were then separated from non-bound modifying agents on a NAP5 column (Cytiva). Conjugation of sulfo-EMCS-proteoliposomes to DARPin-SH was performed during 40 min at room temperature; DARPin-Lip(NanoLuc-LSSmKate1) was separated from non-bound DARPin_9-29 by gel permeation chromatography on a Sepharose CL-2B packed column.

Cell lines

A SKOV3.ip1 ovarian serous cystadenocarcinoma cell line derived from the intraperitoneal ascitic fluid of an immunodeficient mouse, which was intraperitoneally injected with SKOV3 human ovarian adenocarcinoma cells [29], as well as a SKOV3.ip1-NanoLuc cell line stably expressing the NanoLuc luciferase gene (collection of cell lines of the Laboratory of Molecular Immunology, Institute of Bioorganic Chemistry RAS), was used in this study. SKOV3.ip1 and SKOV3.ip1-NanoLuc are characterized by overexpression of the HER2 receptor (10^6 receptors/cell). Cells were cultured under standard conditions (37°C in a humidified atmosphere containing 5% CO_2) in RPMI 1640 (PanEco, Russia) supplemented with 2 mM L-glutamine (PanEco), 10% fetal bovine serum (Gibco), and an antibiotic (10 U/mL penicillin, 10 μg/mL streptomycin, PanEco).

Flow cytometry

The functional activity of the DARPin_9-29 targeted module within the liposomes was studied by assessing the interaction between DARP-Lip(NanoLuc-LSSmKate1) and HER2-positive SKOV3.ip1 cells using flow cytometry. Cells (100,000 cells in 200 μL of the complete growth medium) were incubated at 37°C for 10 min in the presence of 300 nM DARP- Lip(NanoLuc-LSSmKate1) (concentration specified for NanoLuc-LSSmKate1). The cells were washed thrice with phosphate-buffered saline and analyzed on a NovoCyte 3000 flow cytometer. LSSmKate1 fluorescence was excited using a 488 nm laser and detected at 615 ± 20 nm (PerCP-H channel).

Confocal microscopy

Binding of the targeted module within DARP-Lip(NanoLuc-LSSmKate1) to the HER2 receptor on the SKOV3.ip1 cell surface was studied by confocal microscopy. For this purpose, 4,000 SKOV3.ip1 cells were inoculated into the wells of a 96-well glass-bottom microplate (Eppendorf) and cultured overnight. The next day, 300 nM of DARP-Lip(NanoLuc-LSSmKate1) was added to the cells (concentration specified for NanoLuc-LSSmKate1). The cells with the conjugate were incubated for 20 and 90 min. Nuclei were stained with 10 nM of the Hoechst 33342 dye for 10 min at 37°C. The cells were washed thrice with phosphate-buffered saline; after addition of the FluoroBright medium (Gibco), the cells were analyzed on an LSM 980

confocal microscope (Carl Zeiss) using a 63× Plan-Apochromat oil immersion lens. The fluorescence of the Hoechst 33342 dye was excited using a 405 nm laser and detected at 410–520 nm; LSSmKate1 was excited using a 488 nm laser, and fluorescence was detected in the wavelength range of 600–755 nm.

Bioluminescence imaging in the animals

In vivo studies were carried out using Balb/c nude/nude mice. Experiments involving laboratory animals were performed in compliance with the principles of humane animal treatment as specified in the European Union Directives (86/609/ECC) and the Declaration of Helsinki, in accordance with the Guidelines for Proper Conduct of Animal Experiments (Protocol of the Committee Controlling Animal Housing and Use of the Institute of Bioorganic Chemistry, RAS, No. 368/2022 dated December 19, 2022). The model of disseminated intraperitoneal metastases was obtained by intraperitoneal inoculation of 2×10^6 SKOV3.ip1-NanoLuc cells in 100 μL of a serum- and antibiotic-free culture medium. Growth of intraperitoneal tumors was assessed according to the luminescence signal. For this purpose, 7 μg of furimazine (Nano-Glo, Promega) in 100 μL of PBS was injected into the retro-orbital sinus of mice 10 days after inoculation, and bioimaging was performed on an IVIS Spectrum CT system (Perkin Elmier) in the luminescence mode. Fluorescence bioimaging of intraperitoneal tumors was conducted in the epifluorescence mode in the wavelength range of 600–740 nm (with an increment of 20 nm) without any excitation light (the excitation block mode); the agents injected to mice into different retro-orbital sinuses were as follows: 60 min before anesthesia, 2 μM DARP-Lip(NanoLuc-LSSmKate1) (concentration specified for NanoLuc-LSSmKate1); 30 s before anesthesia, and 7 μg of furimazine. Imaging was carried out immediately after the animals had fallen asleep.

RESULTS AND DISCUSSION

Among all the luciferases currently used in BRET sensors, NanoLuc is an ideal energy donor, as it stands out for its extraordinary luminance (luminescence intensity) and small size [30]. The LSSmKate1 red protein with a large Stokes shift having an emission maximum at 624 nm was chosen as the energy acceptor [23]. This protein meets two important conditions: (1) the excitation spectrum of LSSmKate1 (excitation maximum, 463 nm) coincides with that of the oxidized form of the luciferase substrate (emission maximum, 460 nm) (*Fig. 2A*); (2) the emission spectrum of LSSmKate1 lies in the transparency window of biotissue (600–1000 nm), where the absorption coefficient of tissue is minimal [31].

BRET efficiency is known to depend on distance: for nonradiative energy transfer to be efficient, the distance between a donor and an acceptor should be ⩽ 10 nm [32]. That is why it seemed reasonable to obtain the NanoLuc-LSSmKate1 hybrid protein carrying functional modules (luciferase and fluorescent protein) arranged as close as possible. The scheme of BRET sensor operation is shown in *Fig. 2B*: NanoLuc luciferase oxidizes the furimazine substrate, which emits photons in the visible spectral region when converted to its oxidized form, furimamide. This energy is partially absorbed by the acceptor, the LSSmKate1 fluorescent protein, which then becomes excited and fluoresces.

The NanoLuc-LSSmKate1 construct and the respective protein were prepared according to the procedure described in the Experimental section. The absorption spectrum of the purified NanoLuc-LSSmKate1 protein is characterized by strong absorption in the visible spectral region, as indicated by the presence of a peak at 460 nm and the bright yellow color of the purified protein (*Fig. 2C*).

The efficiency of resonance energy transfer in the NanoLuc–LSSmKate1 system, calculated as the ratio between the emission of the donor–acceptor system (NanoLuc–LSSmKate1) at the emission maximum wavelength of the acceptor (624 nm) and the emission of this system at the emission maximum wavelength of the donor (NanoLuc, 460 nm) minus the same ratio detected for the donor only [8, 33], was equal to 0.3 (*Fig. 2D*).

To selectively deliver the BRET sensor to HER2-positive tumors, we used liposomes whose outer surface was modified with the HER2-specific module DARPin_9-29 (Designed Ankyrin Repeat Proteins), which interacts with subdomain I of the HER2 receptor with high affinity (K_D = 3.8 nM) [24]. DARPin proteins belong to a new class of targeted non-immunoglobulin-based molecules. These molecules differ from antibodies by their high expression level, monomericity in solutions, small size, resistance to proteases, and high solubility [34, 35]. These features allow DARPins to compete with antibodies as alternative targeted components within multifunctional compounds designed for cancer therapy.

The method of loading liposomes with the BRET sensor is based on the electrostatic interaction between the positively charged polyhistidine tag (pK_a of histidine's imidazole ~ 6) and the negatively charged inner liposome membrane at neutral pH [28]. The concentration of liposomes loaded with NanoLuc–LSSmKate1 was quantified spectrophotometrically

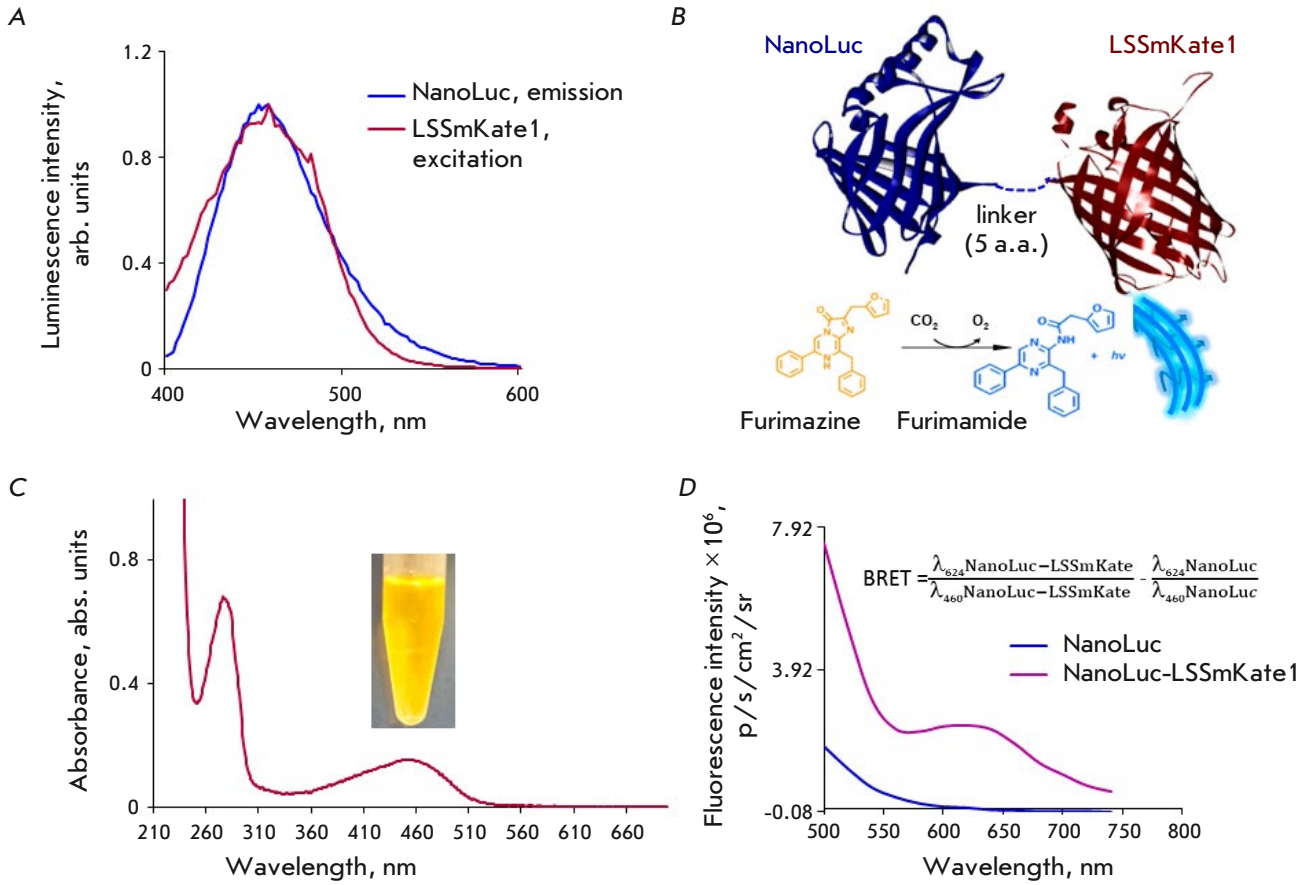

Fig. 2. Characteristics of the NanoLuc-LSSmKate1 BRET sensor. (*A*) – Normalized luminescence spectra of NanoLuc luciferase in the presence of 30 μM furimazine (blue curve) and LSSmKate1 fluorescence (dark red curve). (*B*) – Schematic representation of the NanoLuc-LSSmKate1 BRET sensor and the concept at work: NanoLuc luciferase highly specifically oxidizes its substrate furimazine, whose oxidized form, furimamide, emits light in the blue spectral region. Some of this energy is nonradiatively transferred to LSSmKate1 located in the same polypeptide chain as NanoLuc luciferase. LSSmKate1 begins to fluoresce. (*C*) – Absorption spectrum of the purified NanoLuc-LSSmKate1 protein and a protein sample *in vitro*. (*D*) – Fluorescence spectra of NanoLuc-LSSmKate1 (lilac curve) and NanoLuc (blue curve) recorded in the presence of a luciferase substrate on an IVIS Spectrum CT system without excitation by external light (the excitation block mode). A formula for calculating the efficiency of the resonance energy transfer in the NanoLuc-LSSmKate1 system is provided

by comparing the absorption spectrum of empty liposomes and that of proteoliposomes. As shown in *Fig. 3A*, the spectrum of proteoliposomes (blue curve) coincides with that of the empty liposomes with a concentration of 4.25 mg/mL (green curve) obtained by passing the phospholipid suspension through a filter with a 100 nm pore diameter 15 times. Previously, we found using the hydrophilic membrane-permeable dye, copper phthalocyanine-3,4',4',4',4'-tetrasulfonic acid tetrasodium salt (CPTS), that the concentration of lipid vesicles in 1 mg/mL suspension corresponds to 1.2 nM [28]: hence, the molar concentration of 4.25 mg/mL of the liposome suspension is 5.1 nM. Subtraction of the spectrum of empty liposomes (green curve in *Fig. 3A*) from that of the liposomes loaded with NanoLuc–LSSmKate1 (blue curve in *Fig. 3A*) yields the spectrum of NanoLuc–LSSmKate1 encapsulated into the liposome (lilac curve in *Fig. 3A*).

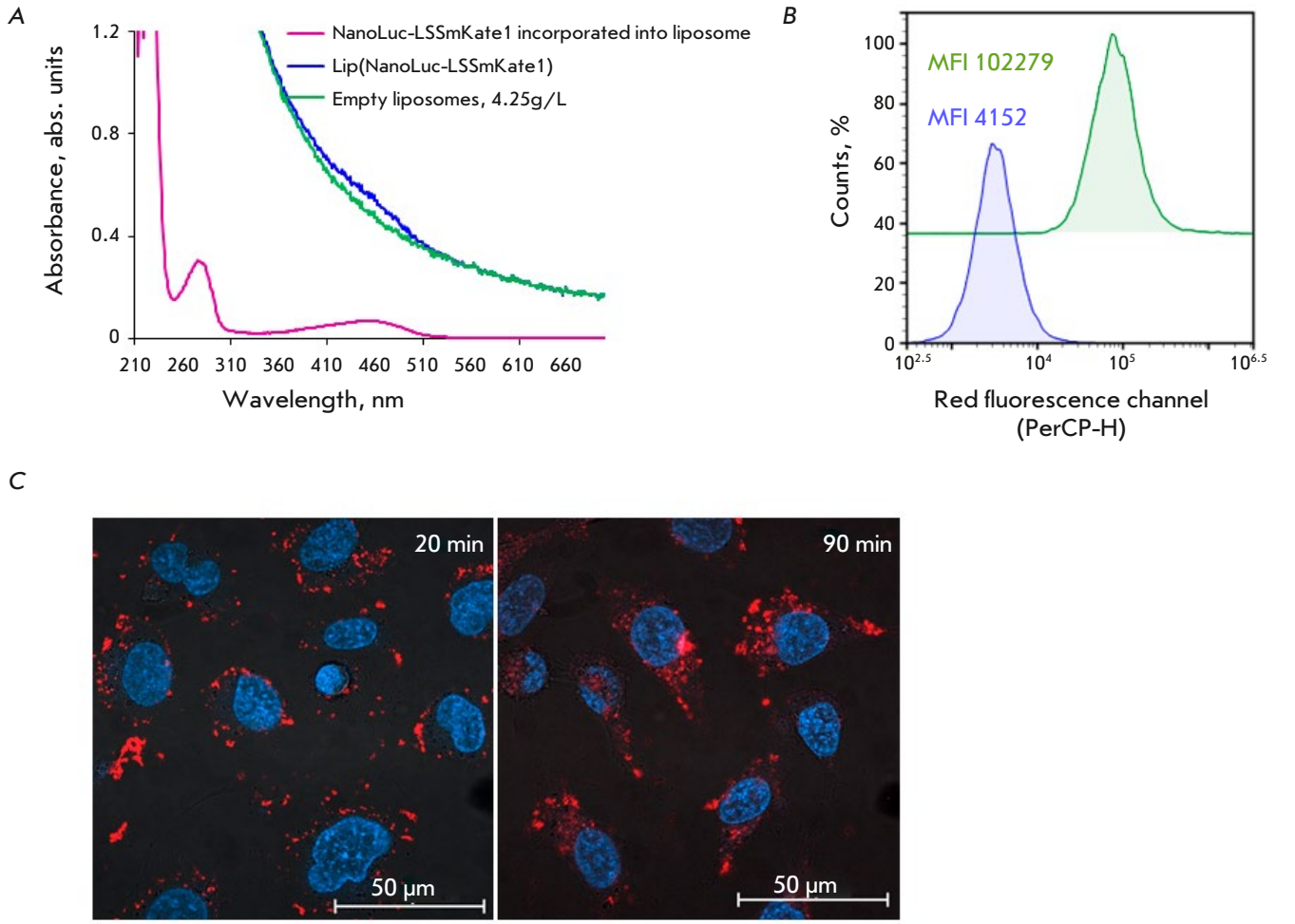

Fig. 3. Characteristics of HER2-specific liposomes loaded with the NanoLuc-LSSmKate1 BRET sensor. (*A*) – Absorption spectra of empty (green curve) liposomes and those containing NanoLuc-LSSmKate1 (blue curve). The purple curve corresponds to the NanoLuc-LSSmKate1 protein loaded into liposomes. (*B*) – Flow cytometry data on the receptor-specific interaction of DARP-Lip(NanoLuc-LSSmKate1) with HER2-positive SKOV3ip cells. The blue curve corresponds to the auto-fluorescence of the cells (control), and the green curve corresponds to cells treated with DARP-Lip(NanoLuc-LSSmKate1). Mean fluorescence intensities (MFI) are shown in the pictogram. The signal was detected in the red fluorescence channel (PerCP-H, $\lambda_{em} = 615 \pm 20$ nm) under laser excitation at 488 nm. (*C*) – Merged confocal images in the blue ($\lambda_{ex} = 405$ nm, detection 410–520 nm) and red ($\lambda_{ex} = 488$ nm, detection 600–755 nm) fluorescence channels of SKOV3ip cells after 20-min (left photo) and 90-min (right image) incubation with DARP-Lip(NanoLuc-LSSmKate1). Nuclei are stained with Hoechst33342

The concentration of the protein encapsulated into liposomes is ~ 5.42 μM ($OD_{280}/\varepsilon_{280}$ = 0.296/54570). Therefore, a single proteoliposome contains ~ 1063 BRET sensor molecules.

Functionalization of proteoliposomes with the DARPin targeted module was conducted using Trout's reagent (2-iminothiolane) and the hydrophilic amino/sulfhydryl crosslinking agent sulfo-EMCS, according to the procedure described in the Experimental section.

The ability of liposomes loaded with the BRET sensor and functionalized with the DARPin targeted module to interact with the HER2 receptor *in vitro* was studied by flow cytometry and confocal microscopy (*Fig. 3B,C*). The flow cytometry data prove the specific interaction between DARPin-modified li-

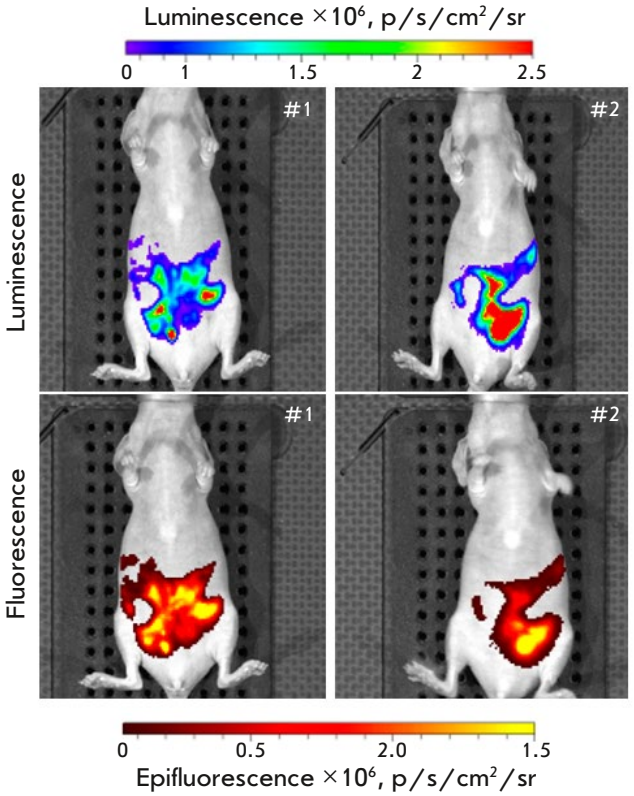

Fig. 4. HER2-specific liposomes loaded with the NanoLuc-LSSmKate1 BRET sensor in the optical bioimaging of disseminated intraperitoneal tumors. The real-time intravital luminescent (top) and fluorescent (bottom) images of animals recorded on an IVIS Spectrum CT system are presented. The images were obtained in two different signal detection modes: top photos, in the bioluminescence mode; bottom photos, in the fluorescence mode without fluorophore excitation

posomes and the HER2 receptor on the SKOV3.ip1 cell surface. As shown in *Fig. 3B*, the mean fluorescence intensity (MFI) of HER2-positive SKOV3.ip1 cells treated with DARP-Lip(NanoLuc-LSSmKate1) is 102,279 (green curve in *Fig. 3B*), which is approximately 25-fold higher than the autofluorescence of these cells (blue curve in *Fig. 3B*).

Confocal microscopy revealed that during a 20-min incubation of SKOV3.ip1 cells in the presence of 300 nM of the DARP-Lip(NanoLuc-LSSmKate1) suspension, targeted proteoliposomes efficiently bind to the cell membrane (the red "crown" along the cell membrane in the left image in *Fig. 3C*). Further incubation for 1.5 h results in internalization of DARP-Lip(NanoLuc-LSSmKate1) as indicated by the red pixels in the cytoplasm (*Fig. 3C*, right image).

Hence, as one can see from the data reported above (*Fig. 3*), the developed system is characterized by a high degree of BRET sensor loading into liposomes and high specificity to the HER2 target.

The applicability of BRET sensor-loaded DARPin-modified liposomes in the real-time non-invasive *in vivo* detection of HER2-positive deep-seated tumors was assessed in the mouse model of disseminated intraperitoneal metastases, based on human ovarian carcinoma SKOV3.ip1 cells stably expressing the *NanoLuc* reporter gene. SKOV3.ip1 cells possess a high metastatic potential, mimicking the late stage of ovarian cancer with extensive spread of tumor cells to the peritoneal wall and surface of organs when injected intraperitoneally [29]. Intraperitoneal tumor growth was monitored by detecting the luminescent signal 10 days after the inoculation of tumor cells expressing *NanoLuc* to the animals (*Fig. 4*, top images). The biodistribution of the DARP-Lip(NanoLuc-LSSmKate1) liposomes systemically administered into the animal body was monitored by detecting the fluorescent signal, which was recorded in the mode when there was no excitation by an external light (*Fig. 4*, bottom images). *Figure 4* demonstrates that the intensity and topography of the fluorescent signal detected after administration of furimazine to mice completely coincide with those of the fluorescent signal detected in the mode without fluorophore excitation (excitation block) after administration of DARP-Lip(NanoLuc-LSSmKate1) and furimazine to mice. Therefore, the developed HER2-specific liposomes carrying a BRET sensor can be used in intravital optical bioimaging to detect deep-seated tumors possessing a specific molecular profile.

CONCLUSIONS

The number of clinically ineffective anticancer drugs is much larger than the number of drugs that have proved to be effective in preclinical studies [2, 36]. This fact indicates that novel models and technologies for the preclinical monitoring of the tumor response to treatment need to be developed [36, 37]. The *in vivo* subcutaneous tumor xenograft models widely used in modern experimental studies enable targeted drug screening and can provide data on drug effectiveness, pharmacokinetics, and pharmacodynamics; however, they cannot be used to assess the metastatic potential of a tumor. Orthotopic models allow one to obtain a relevant disease model, but there arises a problem related to the assessment of how much the tumor burdens the body: what if the

tumor dimensions cannot be measured using a caliper? It is clear that the value of any preclinical model for assessing the efficacy of antitumor compounds is ultimately determined by its ability to predict the clinical response in humans as accurately as possible. The need for intravital imaging of the events occurring in the animal body during preclinical studies of antitumor drugs has driven the rapid development of optical bioimaging, while advances in tumor molecular profiling methods have laid the groundwork for developing the targeted molecular imaging of tumors.

In this study, we have developed a system that allows real-time non-invasive detection of HER2-positive disseminated intraperitoneal tumors using targeted liposomes loaded with a NanoLuc-LSSmKate1 BRET sensor. The system is characterized by a high degree of BRET sensor loading into the liposome (*Fig. 3*) and a proteoliposome specificity to the HER2 receptor both *in vitro* and *in vivo* (*Figs. 3* and *4*); it allows one to perform whole-body non-invasive imaging of tumor processes (*Fig. 4*).

We believe that the developed targeted system for real-time optical bioimaging based on the NanoLuc-LSSmKate1 BRET sensor can become an efficient platform for optimizing preclinical studies of novel targeted drugs. In addition, the elaborated principle of creating a targeted BRET sensor can become a universal platform for non-invasive bioimaging of deep-seated tumors of any molecular profile by simply changing the vector molecule on the liposome surface. ●

This work was supported by the Russian Science Foundation (grant No. 24-14-00088 "Targeted Fluorescent Liposomes as a System for Non-invasive Optical Detection of Primary Tumors and Eradicated Metastases of HER2/EpCAM-Positive Carcinomas".)

REFERENCES

1. Bai J.W., Qiu S.Q., Zhang G.J. // Signal Transduct Target Ther. 2023. V. 8. № 1. P. 89.
2. O'Farrell A.C., Shnyder S.D., Marston G., Coletta P.L., Gill J.H. // Br. J. Pharmacol. 2013. V. 169. № 4. P. 719–735.
3. Hilderbrand S.A., Weissleder R. // Curr. Opin. Chem. Biol. 2010. V. 14. № 1. P. 71–79.
4. Shramova E.I., Kotlyar A.B., Lebedenko E.N., Deyev S.M., Proshkina G.M. // Acta Naturae. 2020. V. 12. № 3. P. 102–113.
5. Badr C.E. // Methods Mol. Biol. 2014. V. 1098. P. 1–18.
6.Serkova N.J., Glunde K., Haney C.R., Farhoud M., De Lille A., Redente E.F., Simberg D., Westerly D.C., Griffin L., Mason R.P. // Cancer Res. 2021. V. 81. № 5. P. 1189–1200.
7. Koessinger A.L., Koessinger D., Stevenson K., Cloix C., Mitchell L., Nixon C., Gomez-Roman N., Chalmers A.J., Norman J.C., Tait S.W.G. // Sci. Rep. 2020. V. 10. № 1. P. 15361.
8. Shramova E.I., Chumakov S.P., Shipunova V.O., Ryabova A.V., Telegin G.B., Kabashin A.V., Deyev S.M., Proshkina G.M. // Light Sci. Appl. 2022. V. 11. № 1. P. 38.
9. Ozawa T., Yoshimura H., Kim S.B. // Anal. Chem. 2013. V. 85. № 2. P. 590–609.
10. Grebenil E.A., Kostyuk A.B., Deyev S.M. // Russ. Chem. Rev. 2016. V. 85. № 12. P. 1277–1296.
11. Endo M., Ozawa T. // Int. J. Mol. Sci. 2020. V. 21. № 18. P. 6538.
12. Főrster T. // Discuss. Faraday Soc. 1959. V. 27. P. 7–17.
13. Yeh H.W., Karmach O., Ji A., Carter D., Martins-Green M.M., Ai H.W. // Nat. Methods. 2017. V. 14. № 10. P. 971–974.
14. Eyre N.S., Aloia A.L., Joyce M.A., Chulanetra M., Tyrrell D.L., Beard M.R. // Virology. 2017. V. 507. P. 20–31.
15. Iglesias P., Costoya J.A. // Biosens. Bioelectron. 2009. V. 24. № 10. P. 3126–3130.
16. Branchini B.R., Rosenberg J.C., Ablamsky D.M., Taylor K.P., Southworth T.L., Linder S.J. // Anal. Biochem. 2011. V. 414. № 2. P. 239–245.
17. Rumyantsev K.A., Turoverov K.K., Verkhusha V.V. // Sci. Rep. 2016. V. 6. P. 36588.
18. Su Y., Walker J.R., Park Y., Smith T.P., Liu L.X., Hall M.P., Labanieh L., Hurst R., Wang D.C., Encell L.P., et al. // Nat. Methods. 2020. V. 17. № 8. P. 852–860.
19. Nishihara R., Paulmurugan R., Nakajima T., Yamamoto E., Natarajan A., Afjei R., Hiruta Y., Iwasawa N., Nishiyama S., Citterio D., et al. // Theranostics. 2019. V. 9. № 9. P. 2646–2661.
20. Ross J.S., Slodkowska E.A., Symmans W.F., Pusztai L., Ravdin P.M., Hortobagyi G.N. // Oncologist. 2009. V. 14. № 4. P. 320–368.
21.Polanovski O.L., Lebedenko E.N., Deyev S.M. // Biochemistry (Moscow). 2012. V. 77. № 3. P. 227–245.
22. Blumenthal G.M., Scher N.S., Cortazar P., Chattopadhyay S., Tang S., Song P., Liu Q., Ringgold K., Pilaro A.M., Tilley A., et al. // Clin. Cancer Res. 2013. V. 19. № 18. P. 4911–4916.
23. Piatkevich K.D., Hulit J., Subach O.M., Wu B., Abdulla A., Segall J.E., Verkhusha V.V. // Proc. Natl. Acad. Sci. USA. 2010. V. 107. № 12. P. 5369–5374.
24. Steiner D., Forrer P., Pluckthun A. // J. Mol. Biol. 2008. V. 382. № 5. P. 121–127.
25. Studier F.W. // Protein Expr. Purif. 2005. V. 41. № 1. P. 207–234.
26. Dragulescu-Andrasi A., Chan C.T., De A., Massoud T.F., Gambhir S.S. // Proc. Natl. Acad. Sci. USA. 2011. V. 108. № 29. P. 12060–12065.
27. Shramova E.I., Filimonova V.P., Frolova A.Y., Pichkur E.B., Fedotov V.R., Konevega A.L., Deyev S.M., Proshkina G.M. // Eur. J. Pharm. Biopharm. 2023. V. 193. P. 208–217.
28. Deyev S., Proshkina G., Baryshnikova O., Ryabova

A., Avishai G., Katrivas L., Giannini C., Levi-Kalisman Y., Kotlyar A. // Eur. J. Pharm. Biopharm. 2018. V. 130. P. 296–305.
29. Yu D., Wolf J.K., Scanlon M., Price J.E., Hung M.C. // Cancer Res. 1993. V. 53. № 4. P. 891–898.
30. Hall M.P., Unch J., Binkowski B.F., Valley M.P., Butler B.L., Wood M.G., Otto P., Zimmerman K., Vidugiris G., Machleidt T., et al. // ACS Chem. Biol. 2012. V. 7. № 11. P. 1848–1857.
31. Mahmood U. // IEEE Eng. Med. Biol. Mag. 2004. V. 23. № 4. P. 58–66.
32. Carpenter S., Fehr M.J., Kraus G.A., Petrich J.W. // Proc. Natl. Acad. Sci. USA. 1994. V. 91. № 25. P. 12273–12277.
33. Proshkina G.M., Shramova E.I., Shilova O.N., Ryabova A.V., Deyev S.M. // J. Photochem. Photobiol. B. 2018. V. 188. P. 107–115.
34. Interlandi G., Wetzel S.K., Settanni G., Pluckthun A., Caflisch A. // J. Mol. Biol. 2008. V. 375. № 3. P. 837–854.
35. Zahnd C., Kawe M., Stumpp M.T., de Pasquale C., Tamaskovic R., Nagy-Davidescu G., Dreier B., Schibli R., Binz H.K., Waibel R., et al. // Cancer Res. 2010. V. 70. № 4. P. 1595–1605.
36. Suggitt M., Bibby M.C. // Clin. Cancer Res. 2005. V. 11. № 3. P. 971–981.
37. Tolmachev V.M., Chernov M.I., Deyev S.M. // Russ. Chem. Rev. 2023. V. 91. № 3. P. RCR5034.

An Attenuated and Highly Immunogenic Variant of the Vaccinia Virus

S. N. Shchelkunov*, S. N. Yakubitskiy, K. A. Titova, S. A. Pyankov, I. S. Shulgina, E. V. Starostina, M. B. Borgoyakova, D. N. Kisakov, L. I. Karpenko, G. A. Shchelkunova, A. A. Sergeev
State Research Center of Virology and Biotechnology "Vector", Rospotrebnadzor, Koltsovo, Novosibirsk region, 630559 Russian Federation
*E-mail: snshchel@rambler.ru
Received: February 10, 2024; in final form, April 05, 2024
DOI: 10.32607/actanaturae.27384

ABSTRACT **The vaccinia virus (VACV) has been used for prophylactic immunization against smallpox for many decades. However, the VACV-based vaccine had been highly reactogenic. Therefore, after the eradication of smallpox, the World Health Organization in 1980 recommended that vaccination against this infection be discontinued. As a result, there has been a rise in the occurrence of orthopoxvirus infections in humans in recent years, with the most severe being the 2022 monkeypox epidemic that reached all continents. Thus, it is crucial to address the pressing matter of developing safe and highly immunogenic vaccines for new generations to combat orthopoxvirus infections. In a previous study, we created a LAD strain by modifying the LIVP (L) VACV strain, which is used as a first-generation smallpox vaccine in Russia. This modification involved introducing mutations in the *A34R* gene to enhance extracellular virion production and deleting the *A35R* gene to counteract the antibody response to the viral infection. In this study, a strain LADA was created with an additional deletion in the DNA of the LAD strain *ati* gene. This *ati* gene directs the production of a major non-virion immunogen. The findings indicate that the LADA VACV variant exhibits lower levels of reactogenicity in BALB/c mice during intranasal infection, as compared to the original L strain. Following intradermal immunization with a 10^5 PFU dose, both the LAD and LADA strains were found to induce a significantly enhanced cellular immune response in mice when compared to the L strain. At the same time, the highest level of virus-specific IFN-γ producing cells for the LAD variant was detected on the 7th day post-immunization (dpi), whereas for LADA, it was observed on 14 dpi. The LAD and LADA strains induced significantly elevated levels of VACV-specific IgG compared to the original L strain, particularly between 28 and 56 dpi. The vaccinated mice were intranasally infected with the cowpox virus at a dose of 460 LD_{50} to assess the protective immunity at 62 dpi. The LADA virus conferred complete protection to mice, with the LAD strain providing 70% protection and the parent strain L offering protection to only 60% of the animals.**

KEYWORDS **vaccinia virus; orthopoxviruses; targeted gene deletion; vaccination; intradermal injection; immunogenicity, protectivity.**

ABBREVIATIONS **CPXV – cowpox virus; VACV – vaccinia virus; PFU – plaque forming units; dpi – day post-immunization; i.d. – intradermal; i.n. – intranasal.**

INTRODUCTION

The dangerous for humans smallpox virus (*Variola virus*, VARV) and its related zoonotic counterparts, the monkeypox (*Monkeypox virus*, MPXV), cowpox (*Cowpox virus*, CPXV), camelpox (*Camelpox virus*, CMLV), and vaccinia (*Vaccinia virus*, VACV) viruses, are all part of the *Orthopoxvirus* genus within the Poxviridae family [1].

Immunizing humans or animals with a low-virulent replicating variant or a weakly pathogenic virus is the most effective method of preventing viral diseases. The earliest recorded form of protection against infectious diseases involved smallpox vaccination [2].

VACV-based vaccines lack significant species specificity towards orthopoxviruses, by which they enable immunization against any type of orthopoxvirus, thus preventing infectious disease outbreaks in both humans and animals [3].

The first-generation smallpox vaccine consisted of VACV, which was propagated by replicating the virus

in the epidermis of calves or other animals. In today's conditions VACV vaccine strains are manufactured using mammalian cell cultures, and they are known as second-generation smallpox vaccines [4, 5].

The World Health Organization strongly recommended discontinuing vaccination after the declaration of the eradication of smallpox around the world in 1980. The decision to discontinue was due to the severe adverse reactions, including fatalities, that were associated with the first-generation live vaccine [1].

The discontinuation of smallpox vaccination has resulted in a notable absence of immunity against zoonotic orthopoxvirus infections among a substantial proportion of individuals, predominantly those under the age of 40–45. Given the rising number of human infections caused by orthopoxviruses, particularly the monkeypox virus, it is crucial to reconsider the potential re-emergence of smallpox or a similar illness through the natural evolution of these viruses [6, 7].

In order to minimize the risk of emergence of highly pathogenic human orthopoxvirus resulting from natural evolution and prevent localized outbreaks from spreading into global epidemics, researchers should concentrate efforts on creating safe new generations of live vaccines based on VACV [3, 8].

The production of third-generation attenuated smallpox vaccines involves the serial passages of a specific VACV strain in a cell culture of a heterologous host. For instance, the well-documented third-generation MVA smallpox vaccine is obtained by subjecting the Ankara VACV strain to a significant number of passages on chicken fibroblast cultures. The genome of the MVA strain underwent multiple mutations and extensive deletions in relation to the DNA of the original VACV strain. MVA is distinguished by its failure to replicate in the majority of mammalian cells, including human cells [9].

A novel strategy for obtaining attenuated replicating fourth-generation smallpox vaccines involves the introduction of targeted mutations or deletions/insertions into the genes that regulate the body's antiviral defense mechanisms via genetic engineering techniques.

Extensive research on gene deletion of immunomodulatory factors in VACV has enabled the identification of specific genes that, upon inactivation, have led to virus attenuation. Various attempts have been made to generate attenuated and highly immunogenic VACV strains through the targeted inactivation of one or several viral genes. However, clinical application of these thus-obtained VACV variants has not followed [3, 4, 10].

We created a recombinant variant of VACΔ5 by modifying the LIVP (L) VACV strain, the first-generation smallpox vaccine used in Russia. This modification involved disrupting five virulence genes, namely hemagglutinin (*A56R*), gamma interferon-binding protein (*B8R*), thymidine kinase (*J2R*), complement-binding protein (*C3L*), and Bcl-2-like inhibitor of apoptosis (*N1L*). It has been demonstrated that deactivating specific virulence genes does not impact the ability of VACV to reproduce in mammalian cell cultures. Characterization of the obtained strain VACΔ5 revealed a notable decrease in reactogenicity and neurovirulence compared to the original L strain [11]. To increase the production of virus-specific antibodies, the *A35R* gene additionally was inactivated in the VACΔ5 genome. The protein product of this gene impedes the presentation of antigens by major histocompatibility complex class II, the activation of T-lymphocytes, and the subsequent generation of chemokines and cytokines. Upon introduction into mice, the created variant VACΔ6 triggered a notably heightened production of virus-neutralizing antibodies and afforded more quality protection than the original L strain [12]. Following preclinical studies [13] and clinical trials, the OrthopoxVac vaccine (VACΔ6) was officially licensed in Russia in November 2022 [2], achieving a significant milestone as the world's first fourth-generation vaccine targeting human orthopoxvirus infections.

Given that VACV encompasses an extensive range of genes responsible for viral progeny formation and immune response regulation to viral infection [10, 14], our research has persisted in developing novel attenuated and highly immunogenic VACV variants through genetic engineering techniques.

The aim of this study was to generate a recombinant LADA variant derived from the L VACV strain. This variant contained specific mutations in the *A34R* gene to enhance the production of extracellular virions. Additionally, the *A35R* gene, which inhibits the antibody response to viral infection, was deleted and the *ati* gene, directing the production of a major non-virion immunogen, was deleted too. Furthermore, we conducted an examination in a mouse model to evaluate the reactogenicity and kinetics of the immune response development specific to VACV vaccination.

EXPERIMENTAL SECTION

Viruses, cell culture

In this study, we utilized Clone 14 of the LIVP strain VACV (L) [11], the LIVP-A34R*-dA35R (LAD) strain derived from it [15], and the GRI-90 CPXV strain [16].

The viruses were cultured and titrated on the CV-1 African green monkey kidney cell line from the SRC VB Vector cell culture collection.

Generation of the recombinant LIVP-A34R*-dA35R-ati strain

For the targeted deletion of the *ati* VACV gene, a monolayer of CV-1 cells was infected with the LAD strain and subsequently transfected with the recombinant plasmid pΔati under the gpt-selection conditions specified for VACV recombinants in the earlier study [17]. PCR analysis and subsequent sequencing of viral DNA allowed us to identify the target virus variant LIVP-A34R*-dA35R-ati (LADA).

The animals

The BALB/c mice used in this research were obtained from the breeding animal facility of the SRC VB Vector. All the experimental animals were housed under veterinary legislation, receiving a standard diet and access to adequate water. We adhered to the ethical principles governing the use of animals in experimental studies. The animal manipulations were conducted with the consent of the Bioethics Committee of the SRC VB Vector (Protocol No. 02-06.2022).

Immunization of mice and subsequent sampling for assays

BALB/c mice, aged 6–7 weeks, were immunized with VACV strains (L, LAD, or LADA) (28 animals per group, virus dose 10^5 plaques forming units (PFU)/20 μL/mouse) via intradermal injection into the dorsal side of the tail, approximately 1 cm from the base [18]. In order to establish a negative control, mice received an injection of saline solution.

The humoral and cellular immune responses in mice were analyzed at 7, 14, and 21 days post-immunization (dpi). Six mice from each group were selected for inclusion in the analysis for every specified time point. Blood was extracted from the retroorbital venous sinus in mice using a 23G × 1.25 needle. The serum was obtained by subjecting individual animal blood samples to centrifugation at a relative centrifugal force of 1000 g for 10 minutes, thereby precipitating the blood cells. The resulting sera were subjected to incubation at a temperature of 56°C for 30 minutes and subsequently stored at a temperature of –20°C.

Following blood collection at 7, 14, and 21 dpi, mice were euthanized by cervical dislocation. Individual spleens were aseptically extracted from each of the six mice in the respective study groups at the corresponding time point.

Blood samples were collected from the retroorbital venous sinus of the same mice (ten mice from each group) at 28, 42, and 56 dpi.

Splenocyte isolation

Splenocytes were isolated by wiping an individual spleen through 70 and 40 μm cell filters (BD Falcon™, USA) using a syringe piston. Once the erythrocytes were removed using an erythrocyte lysis buffer (Sigma, USA), the splenocytes were washed and then resuspended in an RPMI-1640 nutrient medium. The medium was enriched with 2 mM *L*-glutamine and gentamicin at a concentration of 50 μg/mL. The determination of cell viability and concentration was conducted using a trypan blue dye (Bio-Rad, USA) on an automatic cell counter TC20 (Bio-Rad).

Quantification of IFN-γ-producing cells

The T-cell immune response intensity in the immunized mice was assessed by quantifying the number of IFN-γ-producing splenocytes through the IFN-γ ELISpot technique. The experiment was conducted utilizing the Murine IFNγ ELISPOT Kit (with precoated plates) obtained from Abcam, USA, following the guidelines provided by the manufacturer. The splenocytes were cultured in the Lymphogen medium ("PanEco", Russia) with a cell density of 10^5 cells per well. The cells were stimulated using a combination of VACV-specific immunodominant peptides, namely SPYAAGYDL, SPGAAGYDL, VGPSNSPTF, KYGRLFNEI, GFIRSLQTI, KYMWCYSQV, and SFIRSLQNI, each at a concentration of 20 μg/mL [19, 20]. The mitogenic activity was induced using Concanavalin A, with the Lymphogen medium as the negative control. The IFN-γ-producing cells were quantified using an ELISpot reader (Carl Zeiss, Germany).

Enzyme immunoassay of mouse blood sera

The performance of the enzyme-linked immunosorbent assay (ELISA) on individual mouse sera followed the guidelines provided in [18]. The antigen employed in this study was derived from the purification of the virions of strain L VACV using centrifugation with a sucrose cushion. The mouse serum samples underwent titration through a series of twofold serial dilutions, ranging from 1 : 100 to 1 : 12800. The ELISA titration was repeated on the following day. The determination of IgG titers was accomplished using mouse anti-IgG peroxidase conjugates obtained from Sigma, USA. The IgG titers of each serum sample were determined for each repetition individually, and then a mean value was calculated. The geometric

mean values of the logarithms of the VACV-specific IgG reverse titer were computed for each experimental group. Additionally, confidence intervals were determined at the 95% probability level to assess the likelihood of each sample matching the general population.

Assessment of the degree of protective immunity in immunized mice

On dpi 62, the groups that had received immunization with the L, LAD, or LADA strains, as well as the control animals, were infected intranasally (i.n.) with CPXV GRI-90. The infection was administered at a dose of 460 LD_{50} (2.0×10^6 PFU/50 μL/mouse), with 10 animals in each group. A 14-day monitoring period was observed to record the clinical manifestations of infection and mortality in the animals.

To evaluate the presence of disease symptoms, we utilized a scoring scale that encompassed the following values: 0 – no signs of disease; 1 – slight hair ruffling; 2 – severe hair ruffling; 3 – severe hair ruffling, as well as slouching posture or conjunctivitis; 4 – difficulty in breathing or lack of movement; and 5 – death.

We conducted individual weighing sessions of the mice every two days. The arithmetic mean body weights for each group of mice at each time point were determined and then expressed as a percentage of the initial weight.

The data were collected from groups of animals that received immunization with the VACV variants under investigation, as well as from the groups of mice that were not immunized and remained uninfected (Negative Control, N.C.), or were infected with CPXV GRI-90 (Positive Control, P.C.).

Assessment of the pathogenicity of VACV strains

In order to study the pathogenicity of the L and LADA VACV strains through i.n. infection, we utilized 3-week-old BALB/c mice weighing 10–12 g. Each group contained 10 animals. Following inhalation anesthesia with diethyl ether, the mice received an injection of virus-containing liquid (50 μL, dose 10^7 PFU/mouse) or a saline solution (control group) into their nasal cavity. The animals were under observation for 14 days, during which their deaths were documented.

Statistical data analysis

The statistical processing and comparison of the results were conducted using the standard methods provided by the Statistica 13.0 computer program package (StatSoft Inc. 1984–2001). A *P* value below 0.05 was deemed to be statistically significant.

RESULTS

Cellular immune response to vaccination of mice with VACV variants

The vaccination was performed on adult BALB/c mice, aged 6–7 weeks, through intradermal injection. The mice were given the L, LAD, or LADA VACV strains at a dose of 10^5 PFU per animal. Following the time points 7, 14, and 21 dpi, the mice (six animals per group after vestibular blood collection) were euthanized. Spleens were then extracted, and splenocytes were isolated. The quantification of IFN-γ-producing cells in each animal, following stimulation with a pool of VACV-specific peptides, was conducted using ELISpot. As outlined in *Fig. 1*, the results indicate significant discrepancies in the cellular immune response development dynamics and levels among the three VACV variants investigated in the laboratory mice after intradermal immunization.

Humoral immune response to vaccination of mice with VACV variants

Blood samples were collected from BALB/c mice aged 6–7 weeks, which had been intradermally immunized with the L, LAD, or LADA VACV strains at a dose of 10^5 PFU. The samples were taken from the retroorbital venous sinus at 7, 14, 21, 28, 42, and 56 dpi, and sera were obtained at the same time points. The blood samples were collected from six animals in each group at three designated time points, specifically 7, 14, and 21 dpi. The blood samples were collected from the same animals (10 mice per group) at 28, 42, and 56 dpi. The ELISA method was used to determine the VACV-specific IgG titers in each serum sample.

The results depicted in *Fig. 2* provide evidence that the recombinant strains LAD and LADA effectively stimulate the production of VACV-specific IgG, surpassing the levels achieved by the parental strain L, starting from 14 dpi. Notably, the LADA strain was found to produce the highest level of antibodies between 28–56 dpi.

Protective efficacy in immunized mice against a lethal orthopoxvirus infection

This study aimed to assess the impact of the L, LAD, and LADA strains on the development of protective immunity against a lethal infection of mice with heterologous orthopoxvirus. For this purpose, the cohorts of immunized and control (non-immunized) animals were exposed to CPXV GRI-90 at a dosage of 460 LD_{50} on 62 dpi. All experimental groups exhibited signs of viral infection (*Fig. 3*), along with the corresponding change to the body weight of the animals (*Fig. 4*). Vaccination with the LADA strain produced

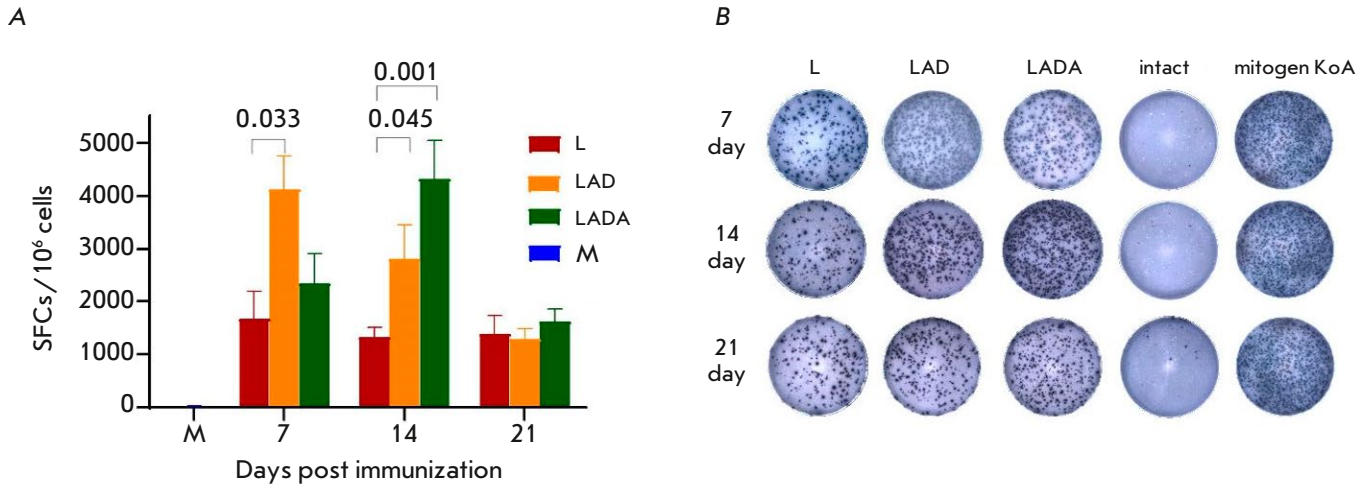

Fig. 1. The results of the ELISpot analysis of the VACV-specific cellular response in BALB/c mice immunized with the L, LAD, or LADA viruses. M – the control mice (not immunized). (*A*) – the number of splenocytes expressing IFN-γ in response to stimulation with a pool of VACV-specific peptides, per million splenocytes. The data are presented as medians along with their respective ranges. Graphical and statistical analysis was performed using the GraphPad Prism 9.0 software. The *P* values are indicated above the brackets. (*B*) – the representative images of ELISpot wells

the least pathogenic effect of CPXV on the mice (*Fig. 3* and *4*). The survival rate of all the animals in this particular group was 100%, whereas in the groups of mice vaccinated with the LAD or L strains, the survival rates were 70% and 60%, respectively (*Fig. 5*).

Pathogenic properties of the L and LADA strains in an intranasal infection of mice

The pathogenicity of the L and LADA strains was investigated in this study using 3-week-old BALB/c mice, with 10 animals in each group. The mice were intranasally infected with viruses at a dosage of 10^7 PFU per animal. The animals were closely monitored over a two-week period, and any instances of mortality were documented. The mortality rate was significantly higher in the group of mice infected with VACV strain L, with 50% of the animals dying, compared to the group infected with strain LADA, where only 10% of the animals died (*Fig. 6*).

DISCUSSION

In the process of coevolution with vulnerable animals, orthopoxviruses have developed diverse molecular mechanisms to suppress specific stages of innate and adaptive immune responses to infection [10]. The genes that govern the immune response are generally nonessential and have no bearing on the ability of viruses to multiply in cell cultures. Consequently, the targeted inactivation or modification of these genes may prove to be a fruitful approach to acquiring attenuated and highly immunogenic variations of VACV [10, 14, 21–25].

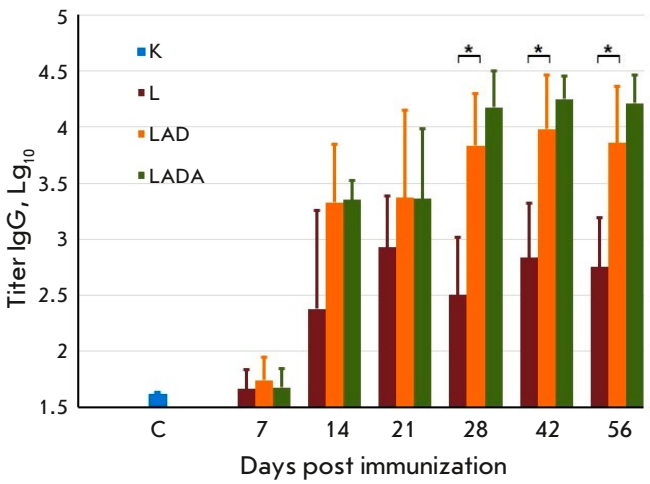

Fig. 2. The titers of the VACV-specific IgG in the sera of mice immunized with the L, LAD, or LADA viruses. C – the blood serum of mice injected with saline. The data are presented as medians along with their respective ranges. Graphical and statistical analysis was performed using the GraphPad Prism 9.0 software.
*Statistically significant differences with $P < 0.05$

In our prior studies, we examined the progression of humoral and T-cell immune reactions in mice that were vaccinated with VACV variants containing a

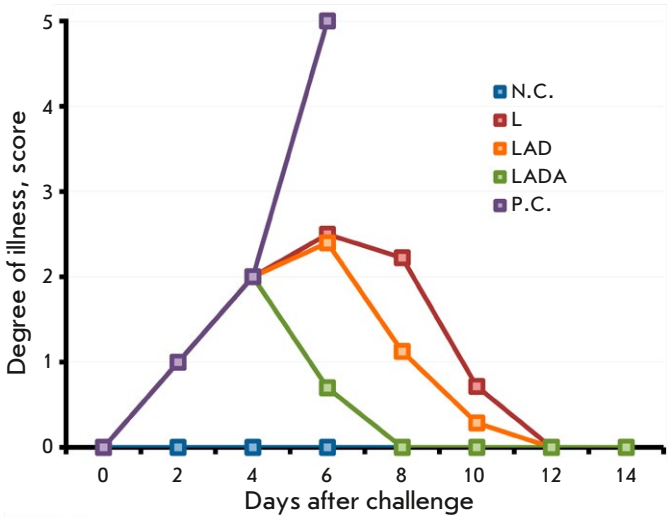

Fig. 3. The dynamics of the clinical manifestations of the infection in mice vaccinated with the L, LAD, or LADA viruses at a dose of 10^5 PFU after intranasal infection with CPXV GRI-90 at a dose of 460 LD_{50} on day 62 after immunization. The data are presented for groups comprising 10 animals that were immunized with the respective viruses, as well as groups that were neither immunized nor infected (N.C.) or infected with CPXV (P.C.)

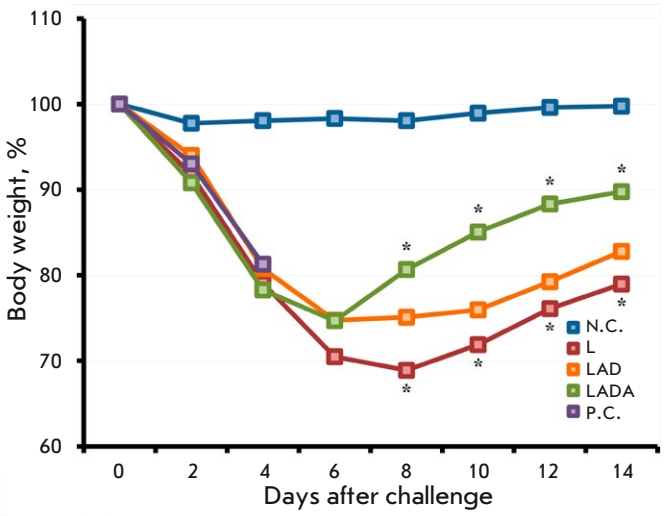

Fig. 4. The dynamics of the changes in body weight in mice vaccinated with the L, LAD, or LADA viruses at a dose of 10^5 PFU after their intranasal infection with CPXV GRI-90 at a dose of 460 LD_{50} on day 62 after immunization. The data are presented for groups comprising 10 animals that were immunized with the respective viruses, as well as groups that were neither immunized nor infected (N.C.) or infected with CPXV (P.C.). *Statistically significant differences with $P < 0.05$ in the mean values between the LADA and L groups

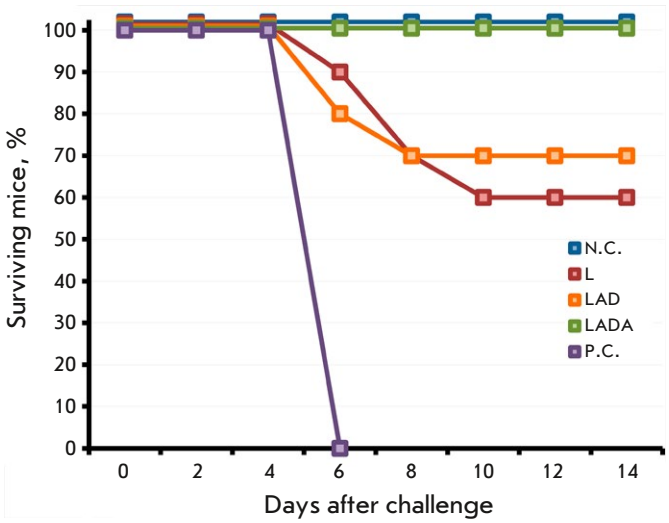

Fig. 5. The dynamics of the death of mice vaccinated with the L, LAD, or LADA viruses at a dose of 10^5 PFU after their intranasal infection with CPXV GRI-90 at a dose of 460 LD_{50} on day 62 after immunization. The data are presented for groups comprising 10 animals that were immunized with the respective viruses, as well as groups that were neither immunized nor infected (N.C.) or infected with CPXV (P.C.)

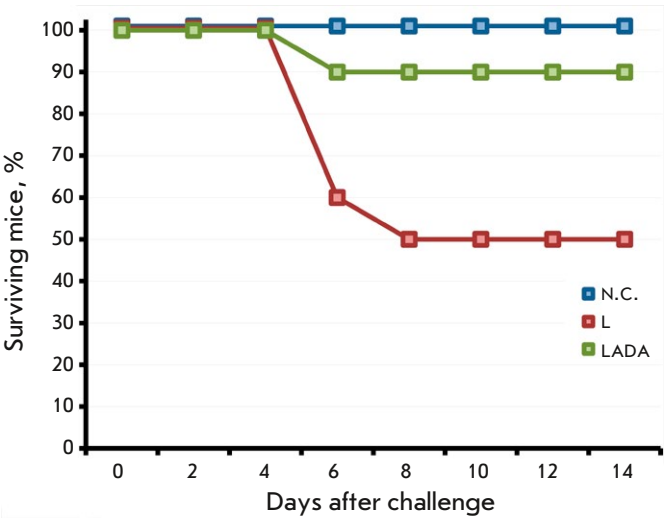

Fig. 6. The dynamics of the death of mice after intranasal infection with the L or LADA viruses at a dose of 10^7 PFU. N.C. – the mice that were intranasally injected with saline. The data are presented for groups comprising 10 animals

mutant *A34R* gene, resulting in heightened extracellular virion production or a deleted *A35R* gene, leading to the inhibition of antigen presentation by major histocompatibility complex class II, inducing immune priming of T-lymphocytes and subsequent synthesis of chemokines and cytokines. The simultaneous modification of the *A34R* gene and deletion of the *A35R* gene produced a synergistic impact on the immunogenic properties of the LAD strain of VACV surpassing those of the parental strain L [15].

Additionally, we investigated the influence of the *ati* gene-encoded non-virion major immunogenic protein production on the manifestation of VACV pathogenicity and immunogenicity [17]. The targeted removal of the *ati* gene resulted in heightened production of VACV-specific IgG in the obtained virus variant LIVPΔati, following the immunization of mice. This increase in IgG production was significantly greater than what was observed with vaccination using the parental L strain. Moreover, immunization with LIVPΔati provided enhanced protection against a subsequent orthopoxvirus infection.

Within this investigation, a modified variant LADA was generated by introducing mutations into the *A34R* gene to enhance extracellular virion production, eliminating the *A35R* gene to suppress its inhibition of the antibody response to viral infection, and deleting the *ati* gene responsible for the synthesis of major non-virion immunogen that does not possess viral neutralizing properties. The investigation into the properties of the LADA strain using an intranasally infected mouse model demonstrated that the resulting VACV variant displays attenuation when compared to the original L strain (*Fig. 6*).

The LAD and LADA strains elicited a more pronounced cellular immune response in mice when they were immunized intradermally with a dose of 10^5 PFU, as compared to the L strain (*Fig. 1*). The highest number of cells producing virus-specific IFN-γ was observed at 7 dpi for the LAD variant, while for LADA it was detected at 14 dpi. The change in the number of IFN-γ-producing cells observed in LADA seems to be caused by the absence of synthesis of a major non-virion immunogen.

Starting at 14 dpi, production of VACV-specific IgG was observed for all strains (*Fig. 2*). Significantly increased levels of specific antibodies were observed in response to the recombinant LAD and LADA variants as compared to the parental L strain, particularly within the 28–56 dpi period. It should be noted that the LADA strain demonstrated the highest levels of VACV-specific antibodies from 28–56 dpi.

The protective immunity conferred by vaccination with the VACV variants was evaluated by infecting the mice with a highly lethal dose of heterologous CPXV at 62 dpi (460 LD_{50}). The LADA virus provided comprehensive protection (*Fig. 5*), resulting in minimal clinical manifestations of infection on the 2nd to 6th day (*Fig. 3*) and a significantly lesser temporary decrease in body weight compared to the other experimental groups of mice (*Fig. 4*). In the same conditions, the parental strain L offered 60% protection whereas the LAD strain showed a higher protection rate of 70%.

Thus, the created LADA variant is attenuated and more immunogenic compared to the L strain, on the basis of which a first-generation smallpox vaccine had been obtained and approved for clinical use in Russia.

Based on these findings, the *A35R* and *ati* genes can be regarded as potential candidates for the integration of target genes into the DNA of the LIVP-A34R* strain, thereby generating safe and efficacious live polyvalent VACV-derived vaccines. ●

This work was conducted with a financial support of the Russian Science Foundation (Grant No. 19-14-00006-П).

REFERENCES

1. Fenner F., Henderson D.A., Arita I., Jezek Z., Ladnyi I.D. Smallpox and Its Eradication. Geneva: World Health Organization, 1988. 1460 p.
2. Shchelkunova G.A., Shchelkunov S.N. // Viruses. 2023. V. 15. P. 103.
3. Moss B. // Immunol. Rev. 2011. V. 239. P. 8–26.
4. Sanchez-Sampedro L., Perdiguero B., Mejias-Perez E., Garcia-Arriaza J., Di Pilato M., Esteban M. // Viruses. 2015. V. 7. P. 1726–1803.
5. Esparza J., Schrick L., Damaso C.R., Nitsche A. // Vaccine. 2017. V. 35. P. 7222–7230.
6. Shchelkunov S.N. // PLoS Pathog. 2013. V. 9. P. e1003756.
7. Harapan H., Ophinni Y., Megawati D., Frediansyah A., Mamada S.S., Salampe M., Bin Emran T., Winardi W., Fathima R., Sirinam S., et al. // Viruses. 2022. V. 14. P. 2155.
8. Shchelkunov S.N. // Vaccine. 2011. V. 29. P. D49–D53.
9. Volz A., Sutter G. // Adv. Virus Res. 2017. V. 97. P. 187–243.
10. Shchelkunov S.N., Shchelkunova G.A. // Acta Naturae. 2020. V. 12. P. 33–41.
11. Yakubitskiy S.N., Kolosova I.V., Maksyutov R.A., Shchelkunov S.N. // Acta Naturae. 2015. V. 7. P. 113–121.
12. Yakubitskiy S.N., Kolosova I.V., Maksyutov R.A., Shchelkunov S.N. // Dokl. Biochem. Biophys. 2016. V. 466. P. 35–38.

13. Shchelkunov S.N., Yakubitskiy S.N., Nesterov A.E., Kolosova I.V., Sergeev A.A., Zaykovskaya A.V., Kabanov A.S., Nechaeva E.A., Bogryantseva M.P., Usova S.V., et al. // Epidemiology and Vaccinal Prevention. 2022. V. 21. № 6. P. 34–47.
14. Albarnaz J.D., Torres A.A., Smith G.L. // Viruses. 2018. V. 10. P. 101.
15. Shchelkunov S.N., Yakubitskiy S.N., Sergeev A.A., Starostina E.V., Titova K.A., Pyankov S.A., Shchelkunova G.A., Borgoyakova M.B., Zadorozhny A.M., Orlova L.A., et al. // Viruses. 2022. V. 14. P. 1453.
16. Shchelkunov S.N., Safronov P.F., Totmenin A.V., Petrov N.A., Ryazankina O.I., Gutorov V.V., Kotwal G.J. // Virology. 1998. V. 243. P. 432–460.
17. Yakubitskiy S.N., Sergeev A.A., Titova K.A., Shulgina I.S., Starostina E.V., Borgoyakova M.B., Karpenko L.I., Shchelkunov S.N. // Acta Naturae. 2023. V. 15. P. 52–57.
18. Shchelkunov S.N., Yakubitskiy S.N., Sergeev A.A., Kabanov A.S., Bauer T.V., Bulichev L.E., Pyankov S.A. // Viruses. 2020. V. 12. P. 795.
19. Oseroff C., Peters B., Pasquetto V., Moutaftsi M., Sidney J., Panchanathan V., Tscharke D.C., Maillere B., Grey H., Sette A. // J. Immunol. 2008. V. 180. P. 7193–7202.
20. Russell T.A., Tscharke D.C. // Immunol. Cell Biol. 2014. V. 92. P. 466–469.
21. Rehm K.E., Connor R.F., Jones G.J.B., Yimbu K., Roper R.L. // Virology. 2010. V. 397. P. 176–186.
22. Garber D., O'Mara L., Gangadhara S., McQuoid M., Zhang X., Zheng R., Gill K., Verma M., Yu T., Johnson B., et al. // J. Virol. 2012. V. 86. P. 12605–12615.
23. Benfield C.T.O., Ren H., Lucas S.J., Bahsoun B., Smith G.L. // J. Gen. Virol. 2013. V. 94. P. 1647–1657.
24. Summer R.P., Ren H., Smith G.L. // J. Gen. Virol. 2013. V. 94. P. 1121–1126.
25. Strnadova P., Ren H., Valentine R., Mazzon M., Sweeney T.R., Brierley I., Smith G.L. // PLoS Pathog. 2015. V. 11. P. e1005151.

GENERAL RULES

Acta Naturae publishes experimental articles and reviews, as well as articles on topical issues, short reviews, and reports on the subjects of basic and applied life sciences and biotechnology.

The journal *Acta Naturae* is on the list of the leading periodicals of the Higher Attestation Commission of the Russian Ministry of Education and Science. The journal Acta Naturae is indexed in PubMed, Web of Science, Scopus and RCSI databases.

The editors of *Acta Naturae* ask of the authors that they follow certain guidelines listed below. Articles which fail to conform to these guidelines will be rejected without review. The editors will not consider articles whose results have already been published or are being considered by other publications.

The maximum length of a review, together with tables and references, cannot exceed 50,000 characters with spaces (approximately 30 pages, A4 format, 1.5 spacing, Times New Roman font, size 12) and cannot contain more than 16 figures.

Experimental articles should not exceed 30,000 symbols (approximately 15 pages in A4 format, including tables and references). They should contain no more than ten figures.

A short report must include the study's rationale, experimental material, and conclusions. A short report should not exceed 12,000 symbols (5–6 pages in A4 format including no more than 12 references). It should contain no more than three figures.

The manuscript and all necessary files should be uploaded to www.actanaturae.ru:

1) text in Word 2003 for Windows format;
2) the figures in TIFF format;
3) the text of the article and figures in one pdf file;
4) the article's title, the names and initials of the authors, the full name of the organizations, the abstract, keywords, abbreviations, figure captions, and Russian references should be translated to English;
5) the cover letter stating that the submitted manuscript has not been published elsewhere and is not under consideration for publication;
6) the license agreement (the agreement form can be downloaded from the website www.actanaturae.ru).

MANUSCRIPT FORMATTING

The manuscript should be formatted in the following manner:

- Article title. Bold font. The title should not be too long or too short and must be informative. The title should not exceed 100 characters. It should reflect the major result, the essence, and uniqueness of the work, names and initials of the authors.
- The corresponding author, who will also be working with the proofs, should be marked with a footnote *.
- Full name of the scientific organization and its departmental affiliation. If there are two or more scientific organizations involved, they should be linked by digital superscripts with the authors' names. Abstract. The structure of the abstract should be very clear and must reflect the following: it should introduce the reader to the main issue and describe the experimental approach, the possibility of practical use, and the possibility of further research in the field. The average length of an abstract is 20 lines (1,500 characters).
- Keywords (3 – 6). These should include the field of research, methods, experimental subject, and the specifics of the work. List of abbreviations.
- INTRODUCTION
- EXPERIMENTAL PROCEDURES
- RESULTS AND DISCUSSION
- CONCLUSION

  The organizations that funded the work should be listed at the end of this section with grant numbers in parenthesis.
- REFERENCES

  The in-text references should be in brackets, such as [1].

RECOMMENDATIONS ON THE TYPING AND FORMATTING OF THE TEXT

- We recommend the use of Microsoft Word 2003 for Windows text editing software.
- The Times New Roman font should be used. Standard font size is 12.
- The space between the lines is 1.5.
- Using more than one whole space between words is not recommended.
- We do not accept articles with automatic referencing; automatic word hyphenation; or automatic prohibition of hyphenation, listing, automatic indentation, etc.
- We recommend that tables be created using Word software options (Table → Insert Table) or MS Excel. Tables that were created manually (using lots of spaces without boxes) cannot be accepted.
- Initials and last names should always be separated by a whole space; for example, A. A. Ivanov.
- Throughout the text, all dates should appear in the "day.month.year" format, for example 02.05.1991, 26.12.1874, etc.
- There should be no periods after the title of the article, the authors' names, headings and subheadings, figure captions, units (s – second, g – gram, min – minute, h – hour, d – day, deg – degree).
- Periods should be used after footnotes (including those in tables), table comments, abstracts, and abbreviations (mon. – months, y. – years, m. temp. – melting temperature); however, they should not be used in subscripted indexes (T_m – melting temperature; $T_{p.t}$ – temperature of phase transition). One exception is mln – million, which should be used without a period.
- Decimal numbers should always contain a period and not a comma (0.25 and not 0,25).
- The hyphen ("-") is surrounded by two whole spaces, while the "minus," "interval," or "chemical bond" symbols do not require a space.
- The only symbol used for multiplication is "×"; the "×" symbol can only be used if it has a number to its

right. The "·" symbol is used for denoting complex compounds in chemical formulas and also noncovalent complexes (such as DNA·RNA, etc.).
- Formulas must use the letter of the Latin and Greek alphabets.
- Latin genera and species' names should be in italics, while the taxa of higher orders should be in regular font.
- Gene names (except for yeast genes) should be italicized, while names of proteins should be in regular font.
- Names of nucleotides (A, T, G, C, U), amino acids (Arg, Ile, Val, etc.), and phosphonucleotides (ATP, AMP, etc.) should be written with Latin letters in regular font.
- Numeration of bases in nucleic acids and amino acid residues should not be hyphenated (T34, Ala89).
- When choosing units of measurement, SI units are to be used.
- Molecular mass should be in Daltons (Da, KDa, MDa).
- The number of nucleotide pairs should be abbreviated (bp, kbp).
- The number of amino acids should be abbreviated to aa.
- Biochemical terms, such as the names of enzymes, should conform to IUPAC standards.
- The number of term and name abbreviations in the text should be kept to a minimum.
- Repeating the same data in the text, tables, and graphs is not allowed.

GUIDENESS FOR ILLUSTRATIONS

- Figures should be supplied in separate files. Only TIFF is accepted.
- Figures should have a resolution of no less than 300 dpi for color and half-tone images and no less than 600 dpi.
- Files should not have any additional layers.

REVIEW AND PREPARATION OF THE MANUSCRIPT FOR PRINT AND PUBLICATION

Articles are published on a first-come, first-served basis. The members of the editorial board have the right to recommend the expedited publishing of articles which are deemed to be a priority and have received good reviews.

Articles which have been received by the editorial board are assessed by the board members and then sent for external review, if needed. The choice of reviewers is up to the editorial board. The manuscript is sent on to reviewers who are experts in this field of research, and the editorial board makes its decisions based on the reviews of these experts. The article may be accepted as is, sent back for improvements, or rejected.

The editorial board can decide to reject an article if it does not conform to the guidelines set above.

The return of an article to the authors for improvement does not mean that the article has been accepted for publication. After the revised text has been received, a decision is made by the editorial board. The author must return the improved text, together with the responses to all comments. The date of acceptance is the day on which the final version of the article was received by the publisher.

A revised manuscript must be sent back to the publisher a week after the authors have received the comments; if not, the article is considered a resubmission.

E-mail is used at all the stages of communication between the author, editors, publishers, and reviewers, so it is of vital importance that the authors monitor the address that they list in the article and inform the publisher of any changes in due time.

After the layout for the relevant issue of the journal is ready, the publisher sends out PDF files to the authors for a final review.

Changes other than simple corrections in the text, figures, or tables are not allowed at the final review stage. If this is necessary, the issue is resolved by the editorial board.

FORMAT OF REFERENCES

The journal uses a numeric reference system, which means that references are denoted as numbers in the text (in brackets) which refer to the number in the reference list.

For books: the last name and initials of the author, full title of the book, location of publisher, publisher, year in which the work was published, and the volume or issue and the number of pages in the book.

For periodicals: the last name and initials of the author, title of the journal, year in which the work was published, volume, issue, first and last page of the article, doi. Must specify the name of the first 10 authors. Ross M.T., Grafham D.V., Coffey A.J., Scherer S., McLay K., Muzny D., Platzer M., Howell G.R., Burrows C., Bird C.P., et al. // Nature. 2005. V. 434. № 7031. P. 325–337. doi: 10.1038/nature03440.

References to books which have Russian translations should be accompanied with references to the original material listing the required data.

References to doctoral thesis abstracts must include the last name and initials of the author, the title of the thesis, the location in which the work was performed, and the year of completion.

References to patents must include the last names and initials of the authors, the type of the patent document (the author's rights or patent), the patent number, the name of the country that issued the document, the international invention classification index, and the year of patent issue.

The list of references should be on a separate page. The tables should be on a separate page, and figure captions should also be on a separate page.

The following e-mail addresses can be used to contact the editorial staff: actanaturae@gmail.com, tel.: (495) 727-38-60.